CHAPTER IV

RESULTS AND DISCUSSION

The main purpose of this research was to prepare silicon containing flame retardant additives for ABS/montmorillonite nanocomposites by using silica extracted from rice husk and corn cob. Rice husk silica (RHS) and corn cob silica (CCS) were prepared by chemical treatment. From calculation, the percentage of yield for RHS and CCS extracted from rice husk and corn cob was approximately 20-21% and 1-2%, respectively. Then, RHS and CCS were modified with two types of silane coupling agents namely vinyltrimethoxysilane (VTMO) and 3-aminopropyltrimethoxysilane (AMMO) in order to improve interfacial adhesion between surface of silica and ABS. In addition, both RHS and CCS were used as starting materials to synthesize silatrane and organomontmorillonite clay (OMT) was also blended with ABS, modified silica, and synthesized silatrane. The effects of OMT loading, type and amount of modified and unmodified silica, and type and amount of silane coupling agent and silatrane on thermal, flame retardant, and mechanical properties of ABS/organomontmorillonite nanocomposites were investigated.

4.1 Characterization of Rice Husk Silica and Corn Cob Silica

4.1.1 CHN Analysis

Rice husk silica (RHS) and corn cob silica (CCS) were extracted from rice husk and corn cob by using acid hydrolysis. The acid treatment used in this research was hydrochloric acid (HCl) to extract ash at high yield with low amount of impurities [Chuayjujit]. After that, they were washed with water for several times until pH was neutral, then they were burnt in furnace at 700^{o}C. Therefore, before hydrolysis and after incineration, CHN analysis was performed to confirm whether acid treatment could get rid of an impurity of organic matters containing in RHS and CCS by measuring the quantity of carbon, hydrogen, and nitrogen atoms. As shown in Table 4.1, the percentage of carbon, hydrogen, and nitrogen atoms of RHS and CCS after hydrolysis and incineration was drastically decreased because HCl could extract organic and inorganic matters from rice husk and corn cob leaving silica more than 99% and 64%,

respectively, obtained by XRF as discussed in the next topic. Therefore, the acid treatment with HCl was a suitable method for extracting silica from rice husk and corn cob.

Table 4.1 CHN analysis of rice husk and corn cob before hydrolysis and after incineration

Samples	Condition	%C	%H	%N
Rice husk	Before hydrolysis	38.78	5.80	0.19
	After incineration	0.25	0.40	0.02
Corn cob	Before hydrolysis	43.77	6.50	0.12
	After incineration	0.82	0.12	0.06

4.1.2 Elemental Analysis

The elemental analysis of RHS and CCS was identified by using X-ray fluorescence (XRF). Figure 4.1, Table 4.2, and Table 4.3 displayed XRF spectra and elemental composition of silica containing in RHS and CCS. From XRF patterns, 99.2% and 64% of silicon were found mainly in RHS and CCS, respectively. Obviously, the silica extracted from rice husk and corn cob had high purity of silicon content, therefore they were expected to be used as starting materials for synthesis of silatrane compound.

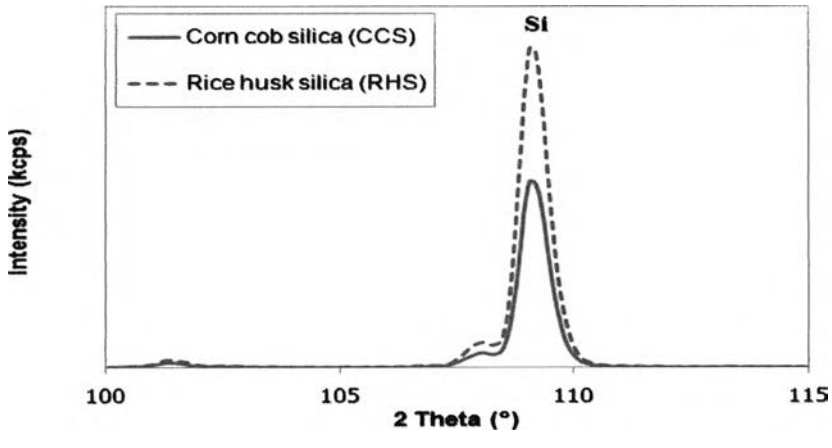

Figure 4.1 XRF spectra of rice husk silica and corn cob silica

Table 4.2 XRF results from rice husk analysis

Analyte	Compound	Concentration (%)
Mg	MgO	0.034
Al	Al_2O_3	0.051
Si	SiO_2	99.2
P	P_2O_5	0.039
S	SO_3	0.08
K	K_2O	0.04
Ca	CaO	0.407
Fe	Fe_2O_3	0.122
Zn	ZnO	0.028

Table 4.3 XRF results from corn cob analysis

Analyte	Compound	Concentration (%)
Na	Na_2O	0.587
Mg	MgO	1.637
Al	Al_2O_3	6.008
Si	SiO_2	64.002
P	P_2O_5	2.646
S	SO_3	7.027
Cl	Cl	0.092
K	K_2O	3.287
Ca	CaO	13.235
Mn	MnO_2	0.114
Fe	Fe_2O_3	0.484
Cu	CuO	0.043
Zn	ZnO	0.83
Sr	SrO	0.009

4.1.3 Chemical Structure by FTIR Technique

The silica extracted from rice husk and corn cob was characterized by FTIR for investigating its functional group. Figure 4.2 revealed that the siloxane of Si-O-Si stretching vibrations appeared at 1107-1098 cm^{-1} and silanol groups of Si-O bending vibrations appeared at 471-467 cm^{-1}. It was also found that the broad absorbing peak of the stretching vibration of O-H bond occurred at 3600-3000 cm^{-1} because the silanol groups could be hydrogen bonded with water or moisture in an atmosphere; in fact, there could be adsorbed water presenting on the silica surface. Furthermore, O-H deformation (in plane) and O-H deformation (out of plane) also appeared at 1680-1600 cm^{-1} and 950-900 cm^{-1}, respectively. This resulted from acid hydrolysis which caused the formation of hydroxyl as other hydrophilic group that might adsorb water. The surface of silica network was also found that Si-H associated peaks appeared at 800-780 cm^{-1}. The FTIR spectra of RHS and CCS shown in Figure 4.2 were similar to that of commercial silica, therefore they could be used as starting material for synthesis of silatrane compound undoubtedly.

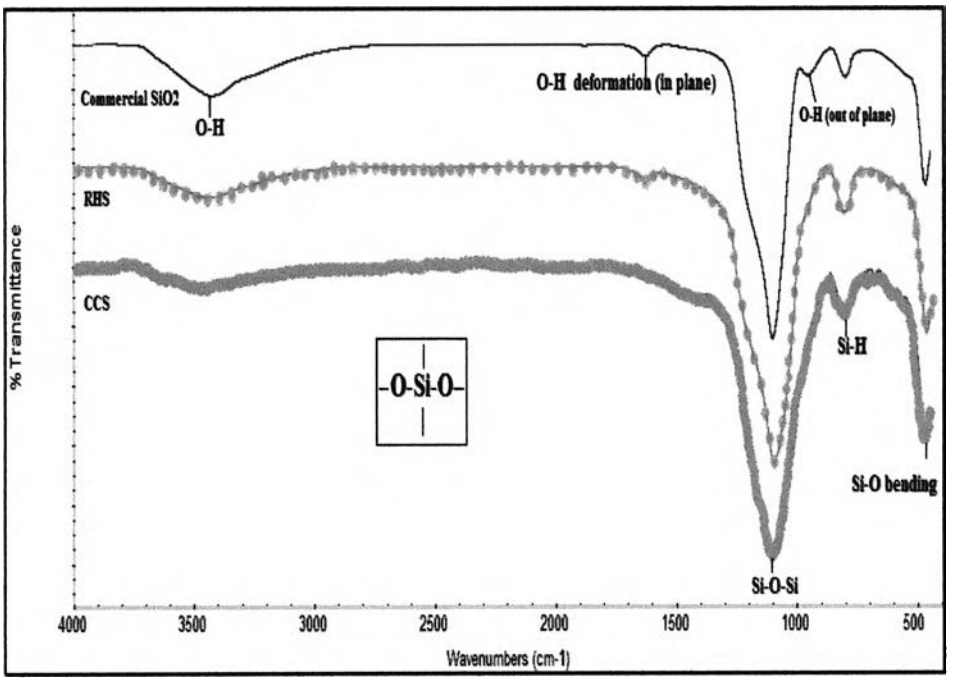

Figure 4.2 FTIR spectra of commercial silica, RHS, and CCS

4.1.4 Crystallinity of RHS and CCS

The crystal structure of RHS and CCS was examined by using X-ray diffractometer (XRD). Normally, silica can be distinguished the different polymorph of silica in three forms, i.e., quartz, cristobalite, and tridymite, respectively, which are depended on temperature used in manufacturing process. As displayed in Figure 4.3 (a), the XRD pattern of CCS obviously showed the small 2θ peak at 25.3°and 26.6° of disordered cristobalite and at 31.4° of tridymite, whereas RHS displayed only a small peak at 9.4° of quartz. These results were because of temperature used in manufacturing process as reported by Della et al [30].

Regarding to the XRD pattern of commercial silica as displayed in Figure 4.3 (a), it was shown that no sharp peak appeared, thus it was completely amorphous in nature. The difference in structure between commercial silica and silica extracted from agricultural wastes resulted from manufacturing process. The commercial silica was produced by the stirred reaction between sodium silicate and acid; whereas both RHS and CCS were incinerated at high temperature (700°C). This high temperature could have an influence on the crystallization of cristobalite and tridymite. In addition, the heating time for producing CCS was longer than that of RHS; therefore, cristobalite and tridymite forms could be found because of transformation of silica form. As a result of this crystal structure, it can be concluded that both RHS and CCS that were crystallite material. This would have an effect on mechanical properties as will be discussed later.

For XRD patterns of unmodified montmorillonite (MMT) and organomontmorillonite (OMT) as exhibited in Figure 4.3 (b), it clearly showed the high intensity of diffraction peak because their structure consisted of several silicate layers, thus the crystalline peaks were very sharp and high. Comparing between the XRD patterns of OMT and MMT, it was found that the 2θ peak at 6.96° of MMT with an interlayer spacing of 12.69 A° was shifted to lower angle at 4.68° with basal spacing of 18.87 A°, hence the increase of basal spacing between OMT and MMT was 6.18 A°. This phenomenon occurred from the modification of MMT with dioctadecyl dimethyl ammonium chloride in order to solve the incompatible problem between SAN matrix and silicate layer of MMT. Similar to other work reported by Ma et al [31], the insertion of

dioctadecyl dimethyl ammonium chloride chain caused separation of silicate layer of OMT, thus the basal spacing was increased drastically.

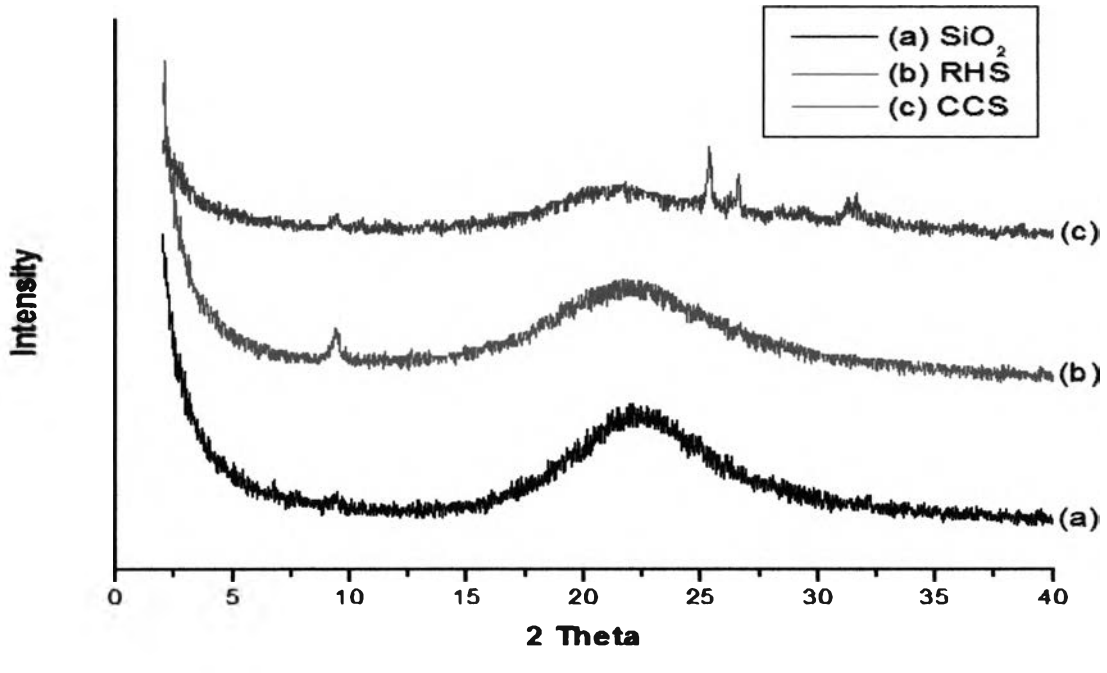

(a)

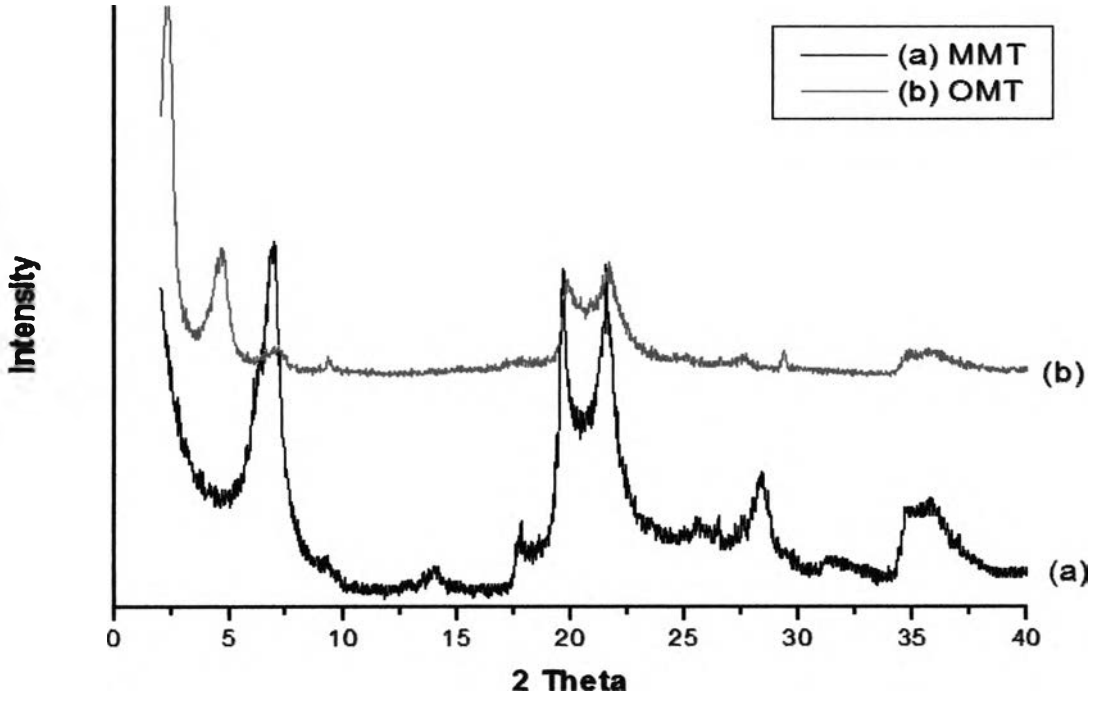

(b)

Figure 4.3 XRD patterns of (a) unmodified commercial SiO_2, RHS, and CCS and (b) unmodified MMT and OMT

4.1.5 Particle size and Surface Area Analysis

The particle size and specific surface area of RHS and CCS were determined by using laser particle size analyzer and surface area analyzer in accordance to Brunauer-Emmett-Teller (BET) method, respectively. Comparing among three types of silica shown in Table 4.4, it was found that silica extracted from rice husk ash had the smallest particle size and highest BET specific surface area of RHS which were 35.30 μm and 201m^2/g, respectively. Generally, the small particle with large surface area of fillers would have an influence on dispersibility in polymer matrix. The fineness of the particles exhibited a very high surface area. Thus, based on these results, it was expected that RHS will be well dispersed in ABS matrix when mixing with twin-screw extruder. Furthermore, it was also found that the particle size of commercial silica was too big when compared to RHS. Hence, its size was confirmed by SEM images as displayed in Figure 4.4. Regarding the surface area of OMT, the result obtained from BET surface area analyzer was incorrect because of the limitation use of this instrument that could determine surface area only in a range of mesoporous and microporous materials.

Table 4.4 Particle size and surface area of silica and OMT

Sample	Particle size (micron)	BET surface area, N_2 (m^2/g)
Commercial silica (SiO_2)	129.20	148.68
Rice husk silica (RHS)	35.30	201.00
Corn cob silica (CCS)	114.80	44.49
Organomontmorillonite (OMT)	21.66	19.67

4.1.6 Morphological Studies

The surface morphology of RHS and CCS was investigated under a scanning electron microscopy (SEM). Usually, the appearance of rice husk and corn cob before hydrolysis was seen by naked eyes as yellow in color and hard in characteristic. When they were hydrolyzed with HCl acid, their appearance was changed to dark brown in color and brittle in characteristic. From SEM images of rice husk and corn cob silica

before hydrolysis, the cell wall structure consisted of cellulose, hemi-cellulose, and lignin as reported by Bharadwaj et al [32]. When rice husk and corn cob were hydrolyzed by HCl acid, organic matters such as lignin, hemi-cellulose and cellulose, would be extracted from their inner cell wall. After incineration at 700^{o}C, the white needle-like powder of RHS and fine white powder of CCS were obtained, and then they were ground with grinder machine. Finally, the RHS and CCS with diamond-cut shape were obtained as displayed in Figure 4.4 (b) and (d), respectively. This morphology was different from that of commercial silica. Figure 4.4 (e) and (f) shown that the shape of commercial silica was clearly rounded-shape or spherical shape.

Unlike the particle size determined by laser particle size analysis shown in Table 4.4 that RHS had a smaller particle size than CCS and commercial silica, from Figure 4.4, SEM images of RHS and CCS particle showed their size of approximately 5 μm; whereas, the particle size of commercial silica was about 20-50 μm. The difference in particle size of silica determined by these two techniques was probably because of some agglomeration of silica particle in n-hexane medium during ultrasonic vibration of laser particle size analysis measurement, leading to higher particle size.

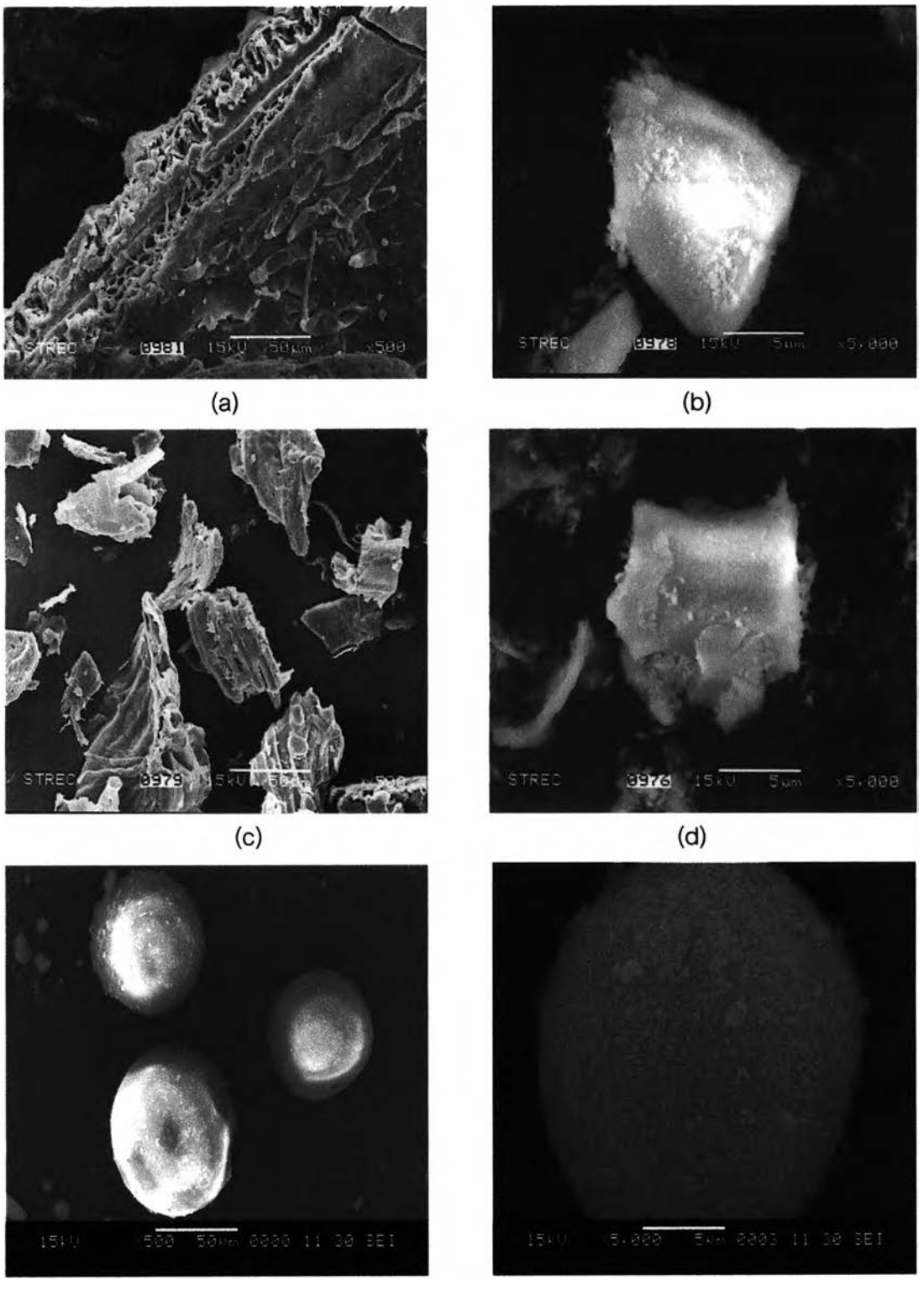

(a) (b)

(c) (d)

(e) (f)

Figure 4.4 SEM micrographs of (a,b) rice husk before hydrolysis and after incineration, (c,d) corn cob before hydrolysis and after incineration, and (e,f) commercial silica, respectively

4.2 Characterization of Surface Modified Silica

Silane coupling agents (e.g., vinyltrimethoxysilane (VTMO) and 3-aminopropyl trimethoxysilane (AMMO)) were used for modifying surface of silica (i.e., commercial silica, RHS, and CCS) to promote adhesion between ABS and silica particles. Before grafting, commercial silica, RHS, and CCS were hydroxylated with HCl acid following procedure of Browne et al [33]. After that, the hydroxylated silica was silylated with silane coupling agent as reaction shown in Figure 4.5. In addition, the hydroxylated silica can also react with each other resulting in -Si-O-Si- or siloxane bond as confirmed by FTIR spectrum and ^{29}Si NMR.

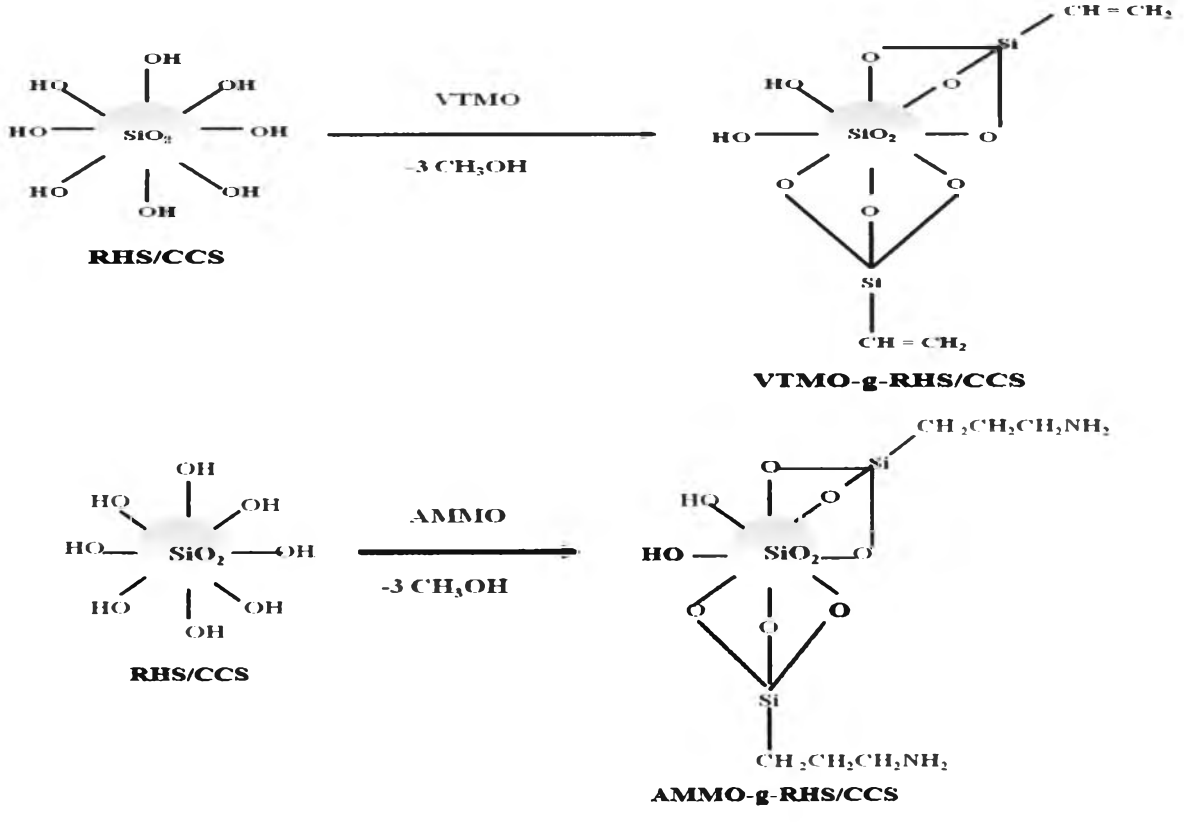

(a)

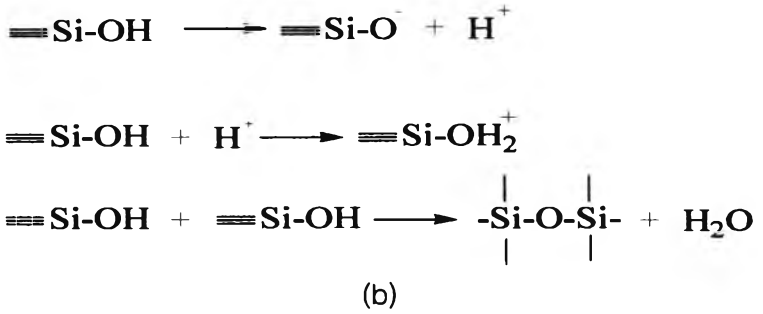

(b)

Figure 4.5 Schematic of (a) reaction of AMMO/VTMO grafted on silica and (b) hydrolysis on silanol group

4.2.1 Chemical Structure by FTIR technique

The change of functional groups contained in commercial silica and RHS before and after grafting with 3-aminopropyltrimethoxysilane (AMMO) and vinyltrimethoxysilane (VTMO) was analyzed by FTIR as shown in Figure 4.6. In case of grafting with AMMO, all hydroxylated silica (commercial silica, RHS, and CCS) were reacted with AMMO by silylation as reaction shown in Figure 4.5. The obtained products were named as AMMO-g-SiO_2, AMMO-g-RHS, AMMO-g-CCS, respectively. The comparison of FTIR spectra between hydroxylated silica and AMMO grafted silica (AMMO-g-SiO_2, AMMO-g-RHS and AMMO-g-CCS) shown in Figure 4.6 (a)-(c) confirmed the existence of Si-O bonding at 468 cm^{-1}, Si-C bonding at 800 cm^{-1}, and Si-O-Si vibration at 1099 cm^{-1}. Furthermore, the presence of aminosilane grafting was confirmed by an appearance of secondary amine N-H stretching at 3600-3000 cm^{-1}, N-H bending at 1635 cm^{-1}, C-NH_2 stretching at 1120-1000 cm^{-1} and the increase in the intensity of methyl band C-H stretching was appeared at 2930 cm^{-1}, -CH_2 or -CH_3 at 1400 cm^{-1}, and -(CH_2)- at 694 cm^{-1}. From these spectra, the functional groups of AMMO-g-SiO_2, AMMO-g-RHS, and AMMO-g-CCS were similar, confirming the success of grafting AMMO on surface of commercial SiO_2, RHS, and CCS, respectively.

The silica (commercial silica and RHS) grafted with VTMO was called VTMO-g-SiO_2 and VTMO-g-RHS, respectively. The comparison of FTIR spectra of silica, hydroxylated silica, and grafted silica presented the existence of Si-O bonding at 466 cm^{-1}, Si-C bonding at 783 cm^{-1}, and Si-O-Si vibration at 1097 cm^{-1}. This result indicated the siloxane structure in commercial silica, RHS, and CCS. Furthermore, the presence of vinyltrimethoxysilane grafting was confirmed by the appearance of methyl band C-H stretching at 2962 cm^{-1}, -CH_2 or -CH_3 bonding at 1410 cm^{-1}, -(CH_2)- at 695 cm^{-1}, C=C bonding at 1605 cm^{-1}, and also stretching of Si-OH at 3025 cm^{-1}. As a result, it can conclude that all hydroxylated silica (commercial silica and RHS) can be successfully grafted with VTMO.

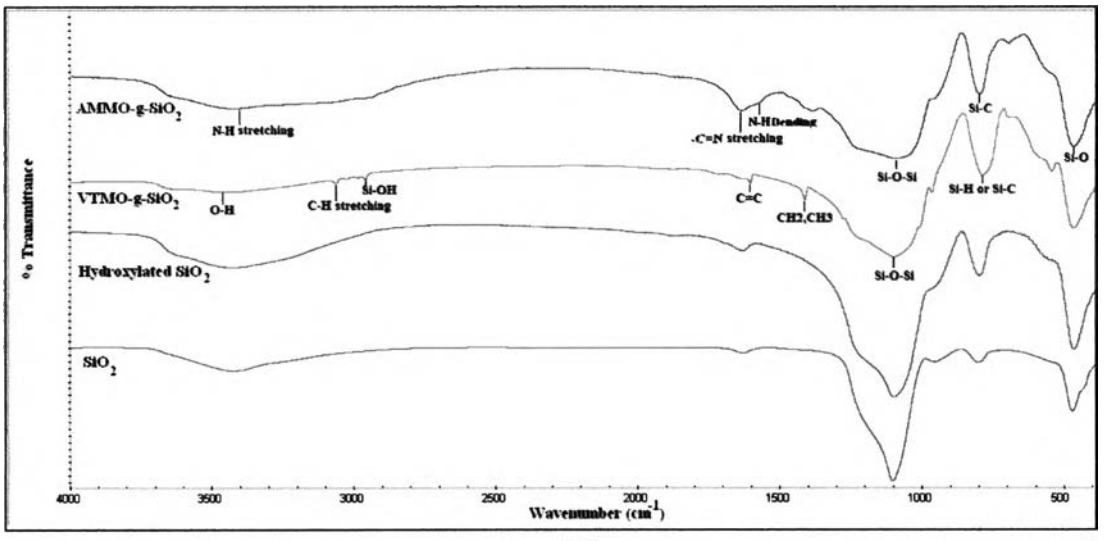

(a)

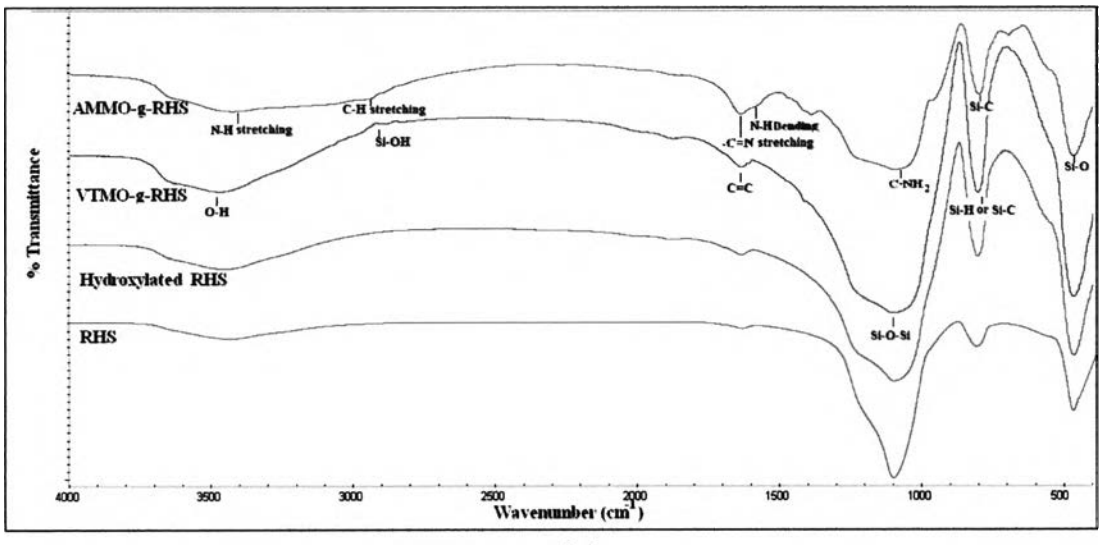

(b)

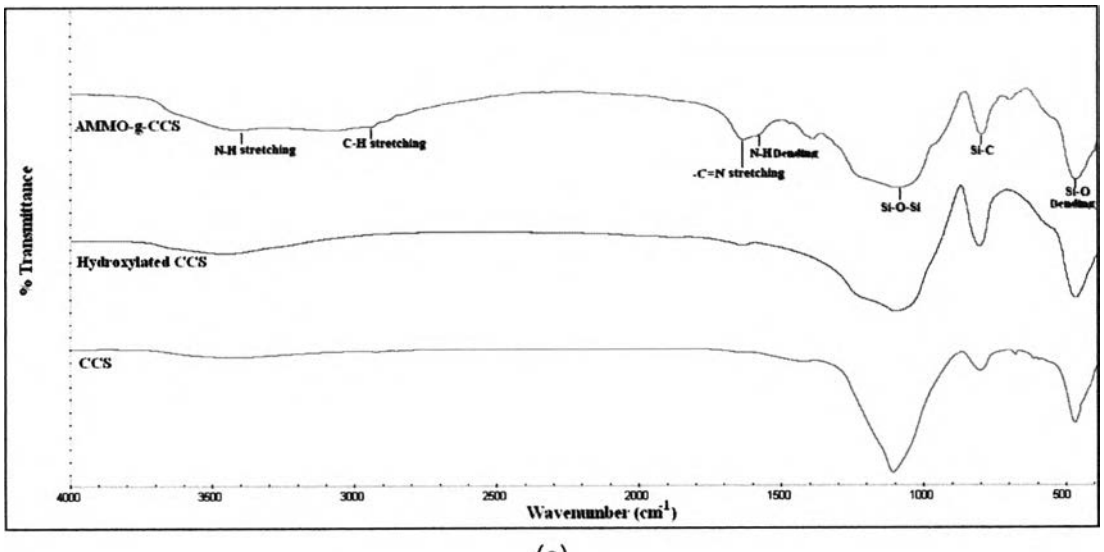

(c)

Figure 4.6 FTIR spectra of AMMO and VTMO grafted on (a) commercial silica, (b) RHS, and (c) CCS

4.2.2 Chemical Structure by ^{29}Si NMR Technique

The chemical structure of hydroxylated RHS, CCS, and commercial silica was investigated by using ^{29}Si NMR spectroscopy. From Figure 4.7, it was shown that hydroxylated RHS, CCS, and commercial silica contained siloxane and silanol groups on their surface as previously shown in Figure 4.6. The signals approximately at –110 ppm, -100 ppm, and –90 ppm obtained from unmodified RHS and CCS were assigned to siloxane, free silanols, and geminal silanols group, respectively, as also reported by Bauer et al [34].

Obviously, the signal at -100 ppm of hydroxylated SiO_2 and RHS was very strong indicated the free silanols in their structure; whereas the hydroxylated CCS exhibited very high intensity of the signal at -110 ppm, corresponding to siloxane.

Surface of silica, modified with two types of silane coupling agents, i.e., VTMO and AMMO, to improve the dispersibility of silica in polymer matrix, was investigated by using ^{29}Si NMR. Silane grafted on surface of RHS, CCS, and commercial silica determined by ^{29}Si NMR spectroscopy was shown in Figure 4.9- 4.12. The signals appeared at –112 ppm, –100 ppm, and –92 ppm obtained from unmodified or hydroxylated commercial SiO_2 were assigned to siloxane groups, free silanols, and geminal silanols, respectively. After grafting with VTMO, additional peaks in the region at –71 ppm and –79 ppm were observed and when commercial SiO_2 was modified with AMMO, the additional peaks were also found at -59 ppm and -67 ppm. In addition , no peak in the range from 0 to -50 ppm was appeared, it could be confirmed that these peaks were indicated condensation of water in silylation reaction as displayed in Figure 4.5 and 4.6. Moreover, the structure of product modified with the functional groups of trimethoxysilanes was type of bidentate and tridentate structure as structure shown in Figure 4.8 [34-35].

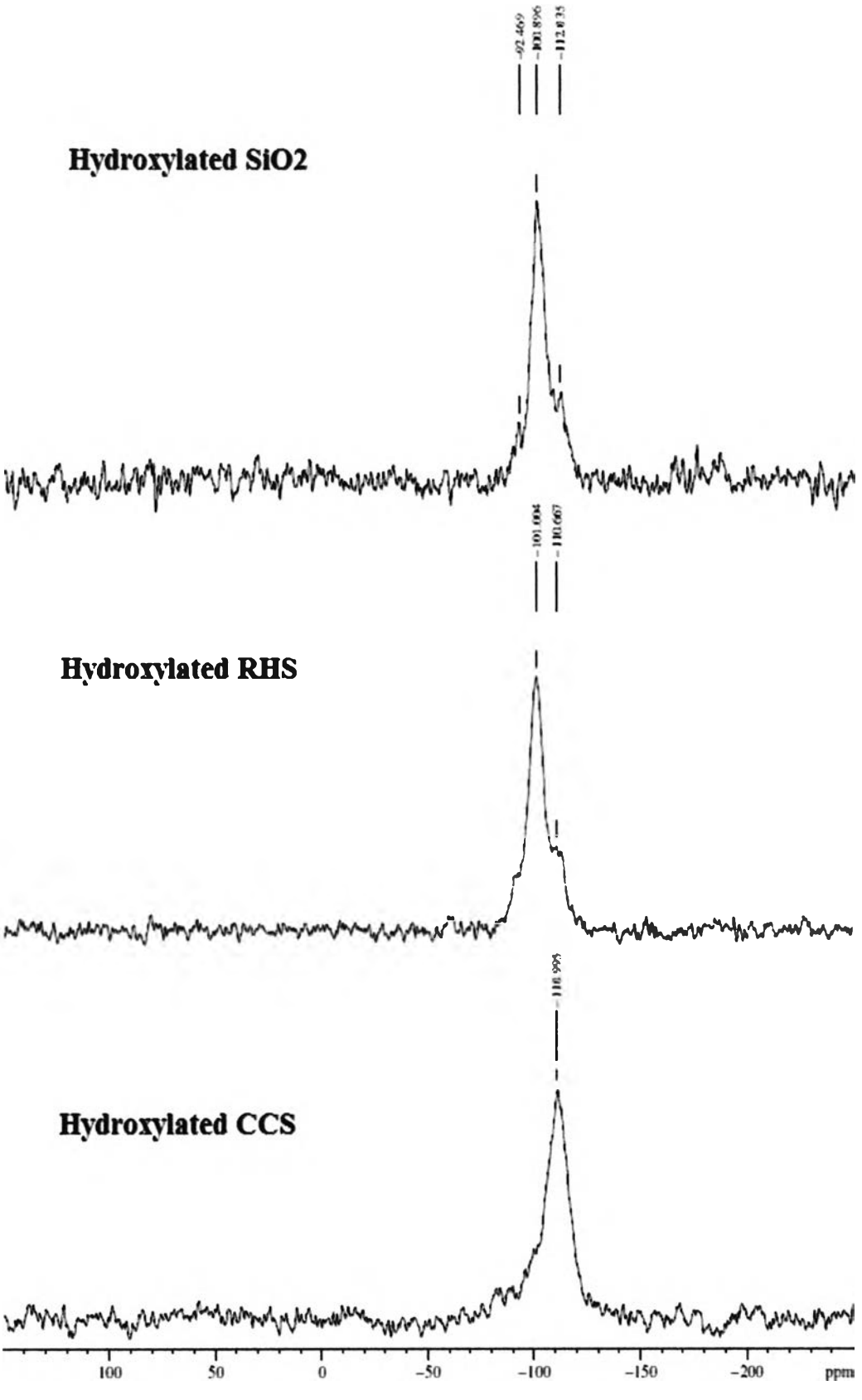

Figure 4.7 ^{29}Si NMR of hydroxylated SiO_2, hydroxylated RHS, and hydroxylated CCS

The position of additional peaks from AMMO and VTMO appeared in Figure 4.10 and 4.11 were similar to peaks in Figure 4.9. Therefore, these results showed the successful grafting of AMMO/VTMO onto surface of silica. In addition, it was found that silica modified with aminosilane gave higher signal intensities and greater shifted of the signals to the higher field more than those of vinylsilane. This resulted from amino group in AMMO structure.

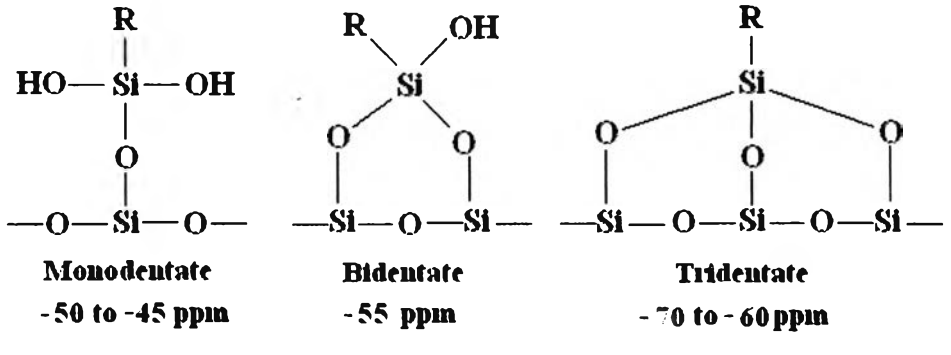

Figure 4.8 Schematic of monodentate, bidentate, and tridentate structure

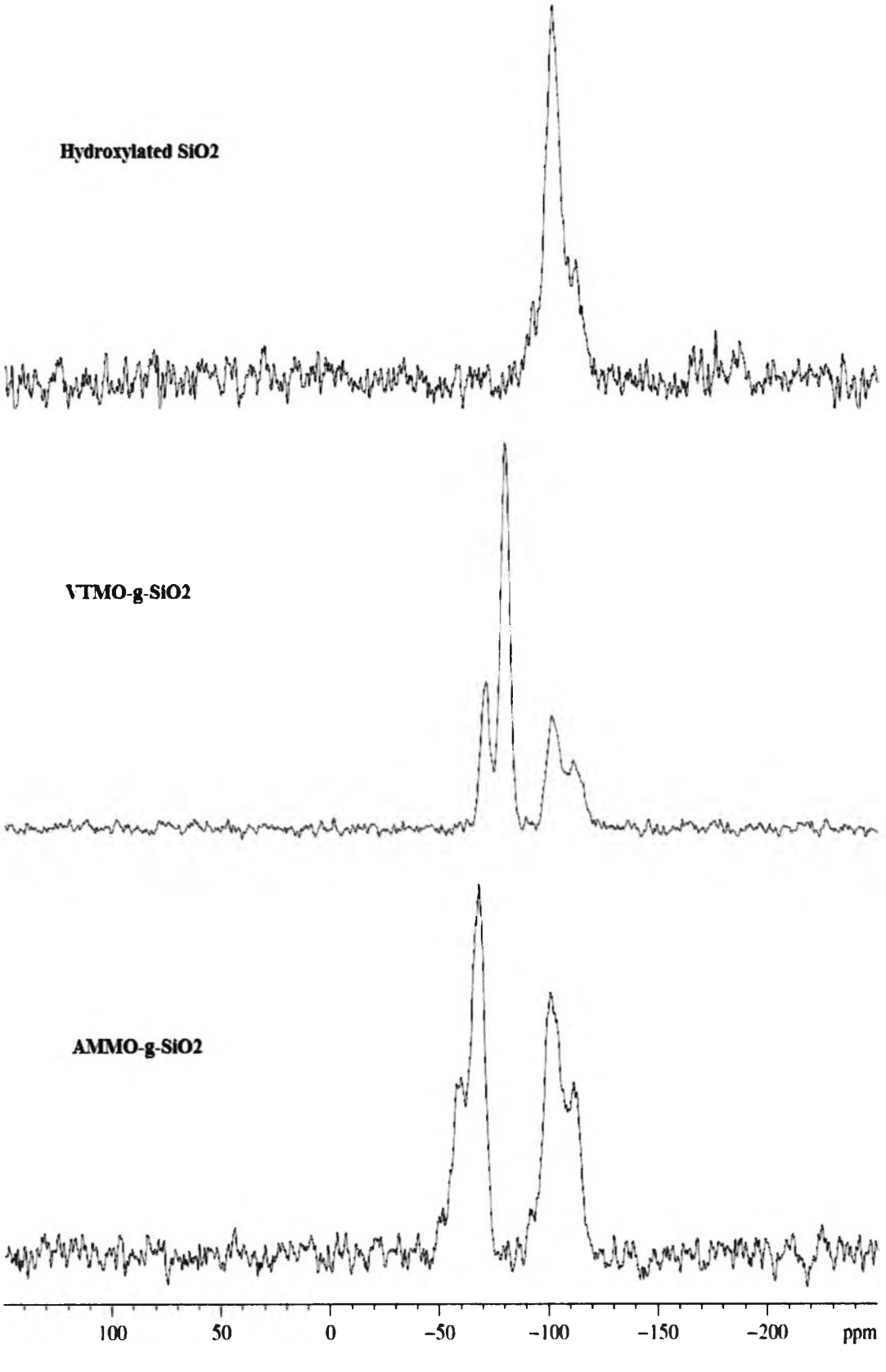

Figure 4.9 ^{29}Si NMR of hydroxylated SiO_2, VTMO-g-SiO_2, and AMMO-g-SiO_2

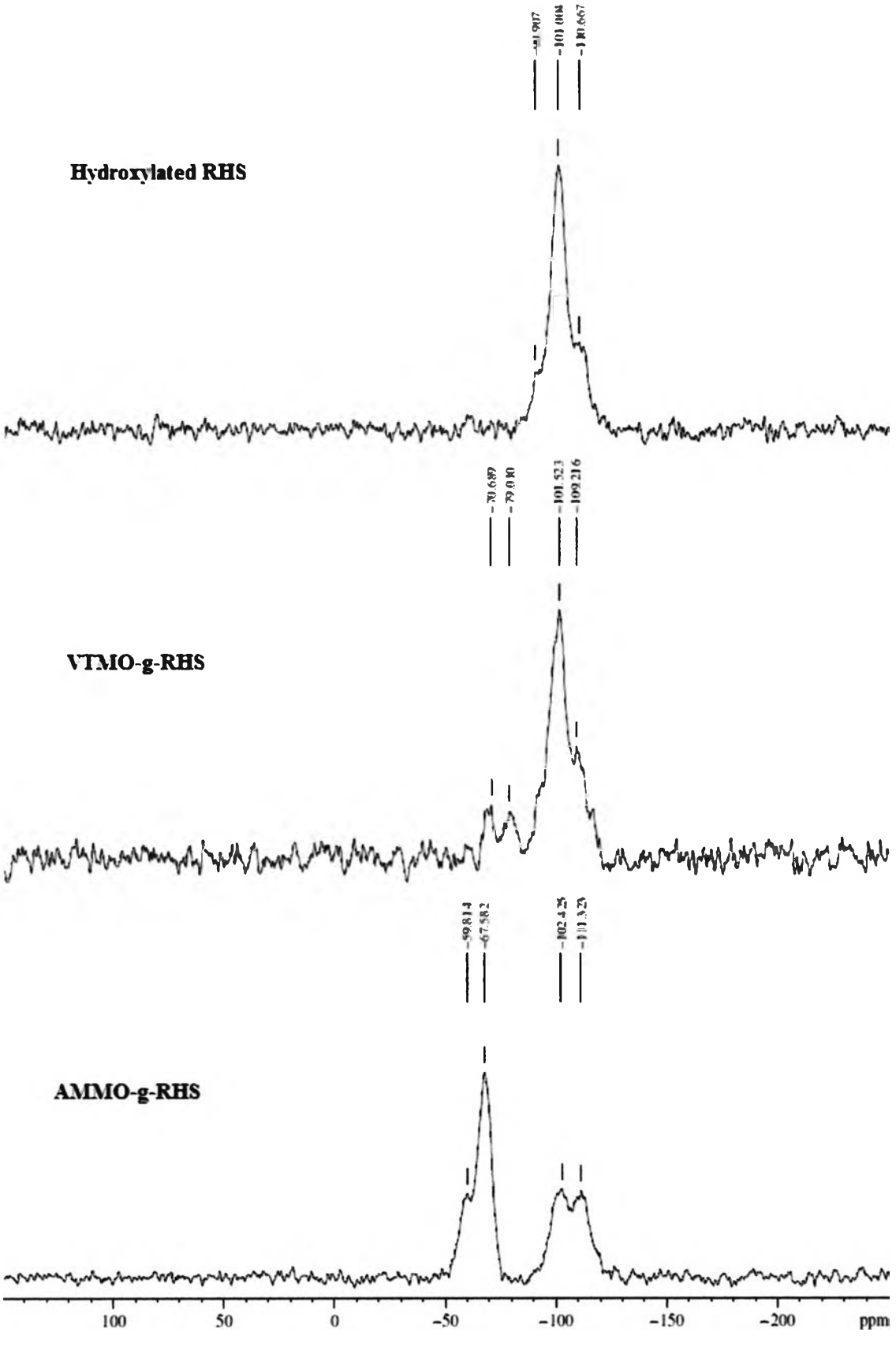

Figure 4.10 ^{29}Si NMR of hydroxylated RHS, VTMO-g-RHS and AMMO-g-RHS

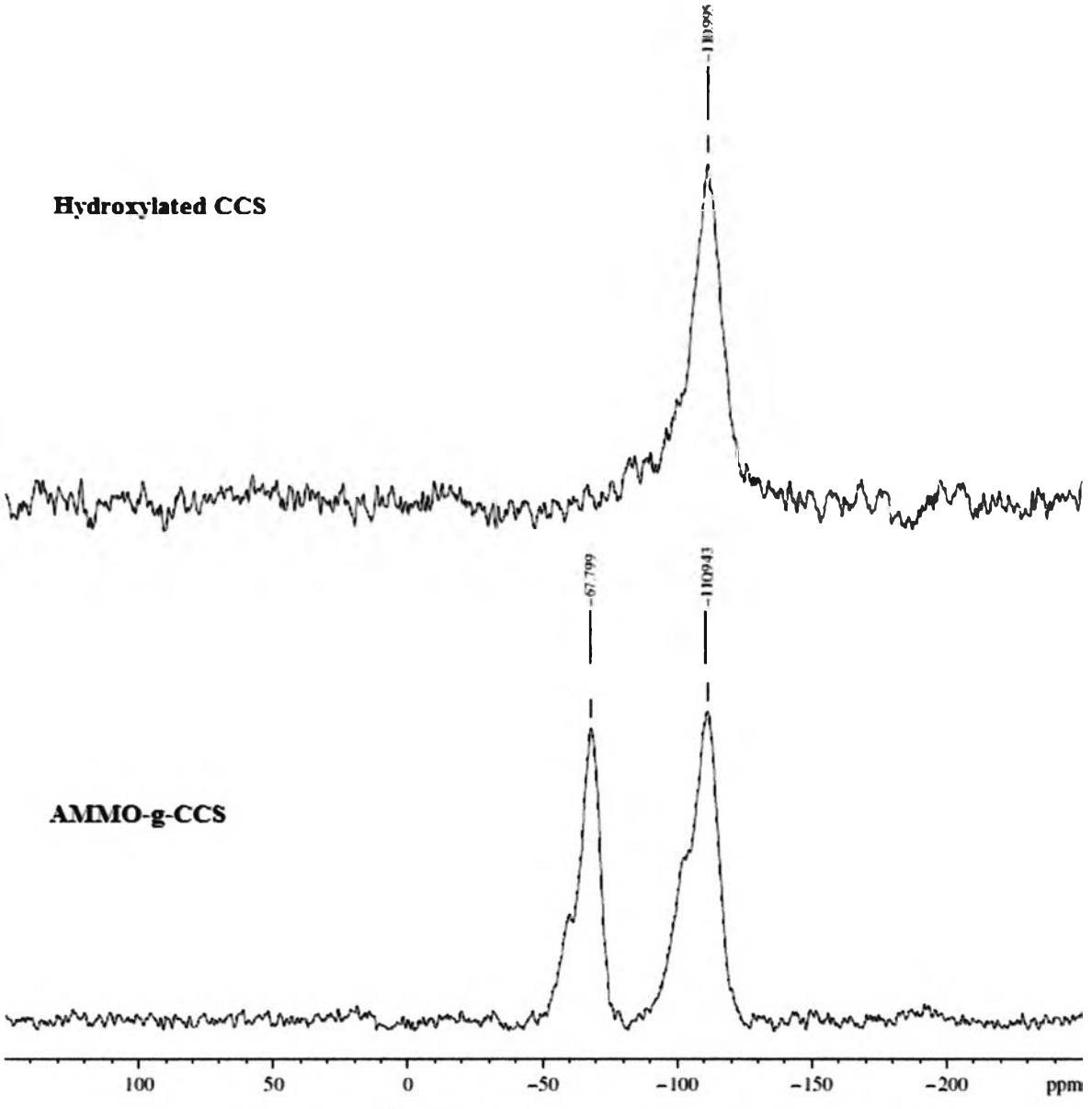

Figure 4.11 ^{29}Si NMR of hydroxylated CCS and AMMO-g-CCS

According to the work of He, et al., All of additional peaks appeared in Figure 4.12 revealed that the position at -67 ppm was tridentate structure, which can be hydrolyzed and condensed in the solution of water/methanol mixture or silylation reaction [33-35].

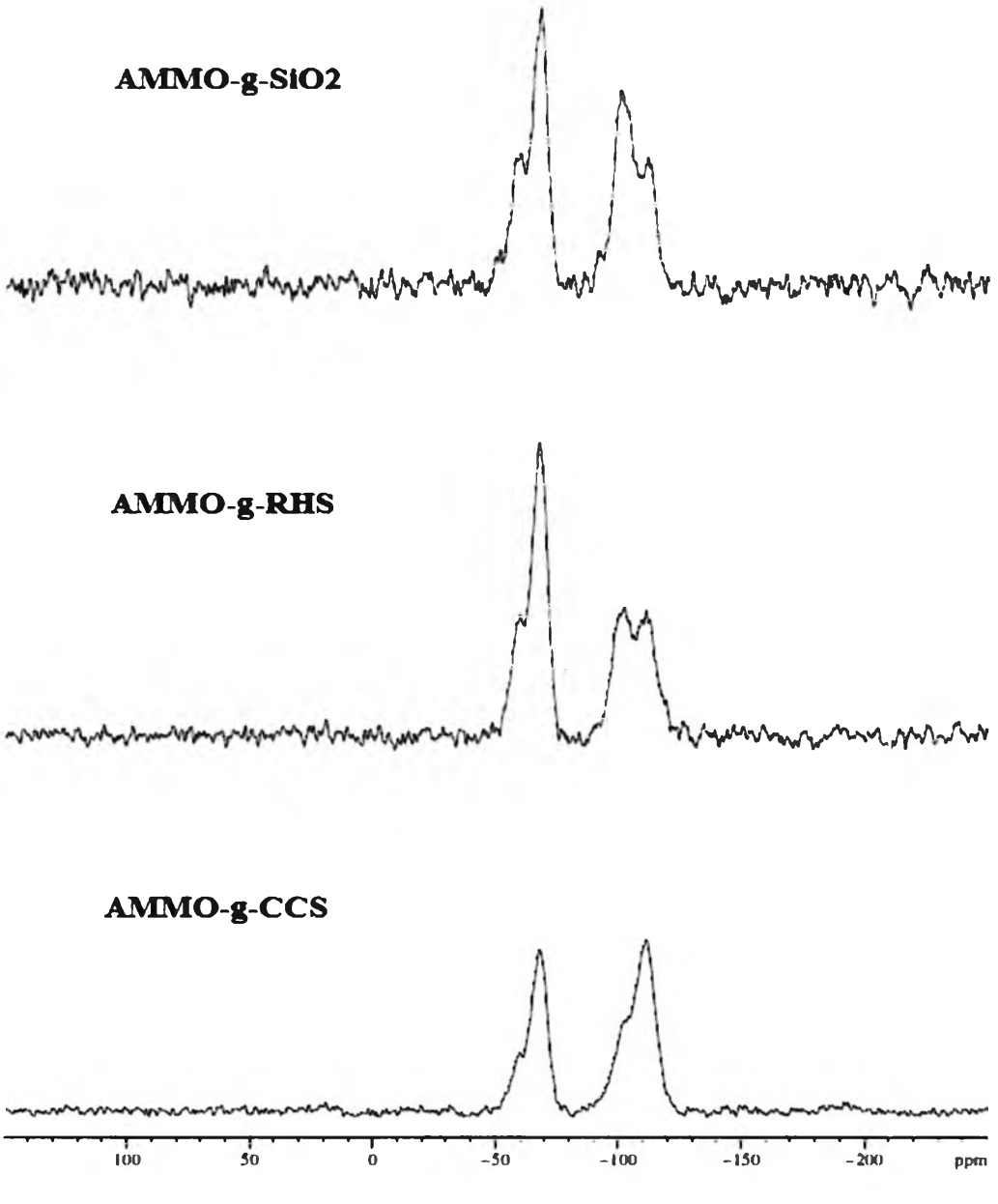

Figure 4.12 ^{29}Si NMR of AMMO-g-SiO_2, AMMO-g-RHS, and AMMO-g-CCS

4.2.3 Crystallinity by XRD Technique

The crystal structure of AMMO-g-SiO_2, AMMO-g-RHS, and AMMO-g-CCS were determined by using X-ray diffractometer (XRD). XRD patterns of all AMMO grafted on commercial silica, RHS, and CCS were shown in Figure 4.13. In comparison to XRD patterns shown in Figure 4.3 it was found that the peak intensity decreased obviously after grafting with

AMMO and the 2θ diffraction peak of AMMO-g-RHS and AMMO-g-SiO_2 was found at 9.3°of siloxane [38]. This additional peak, compared with the ungrafted silica (Figure 4.3), resulted from siloxane bond containing in AMMO. However, AMMO-g-CCS had no such peak at 9.3°of siloxane but the cristobalite peak was still noticed at 26° and 28°. This result indicated that all of AMMO grafted on silica was crystalline structure [36-38].

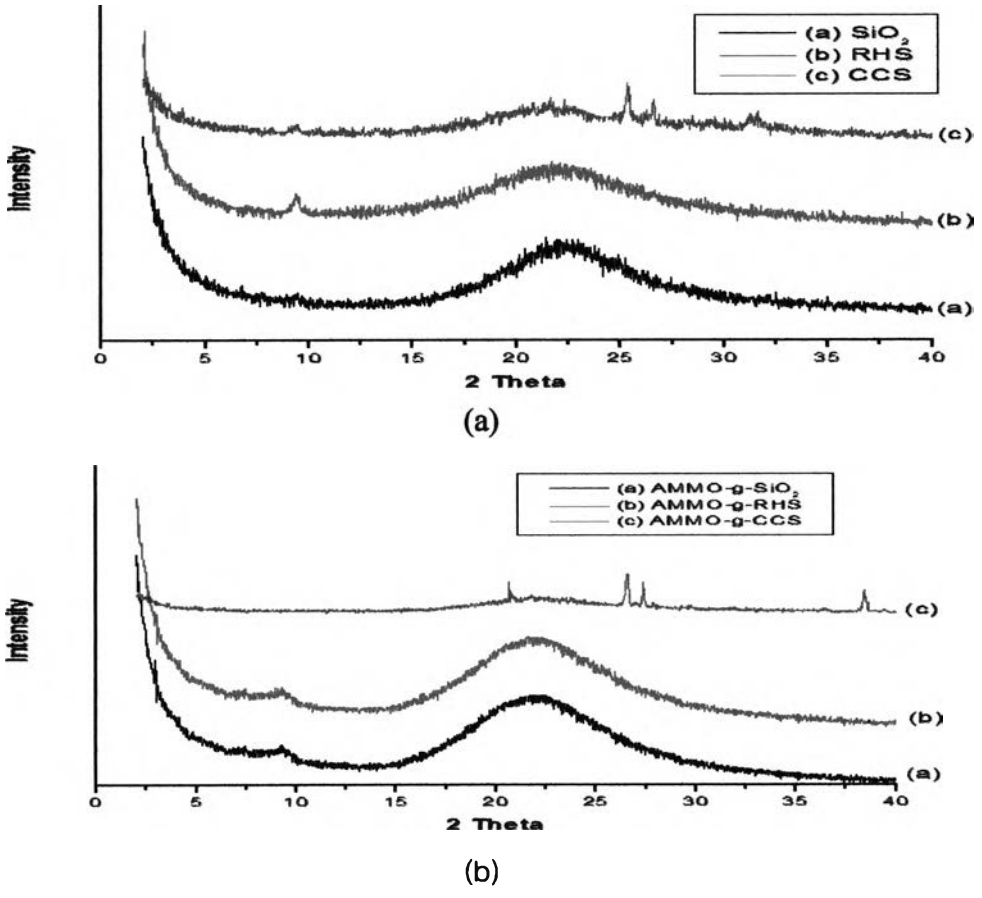

Figure 4.13 XRD patterns of (a) before grafting and (b) after grafting of AMMO-g-SiO_2, AMMO-g-RHS, and AMMO-g-CCS

4.2.4 Morphological Studies

The morphological characteristics of AMMO-g-SiO_2, AMMO-g-RHS, and AMMO-g-CCS were determined by using a scanning electron microscope. The SEM micrographs of silica modified with AMMO were illustrated in Figure 4.14. All of AMMO grafted on silica was white fine powder as seen by naked eye. Under microscope, the particle size of each powder was less than 0.5 μm and in a range of nanometer. Nevertheless, aggregated particles were seen clearly. Comparing to ungrafted silica (Figure 4.4), all of the AMMO grafted silica powder had significantly smaller particle size.

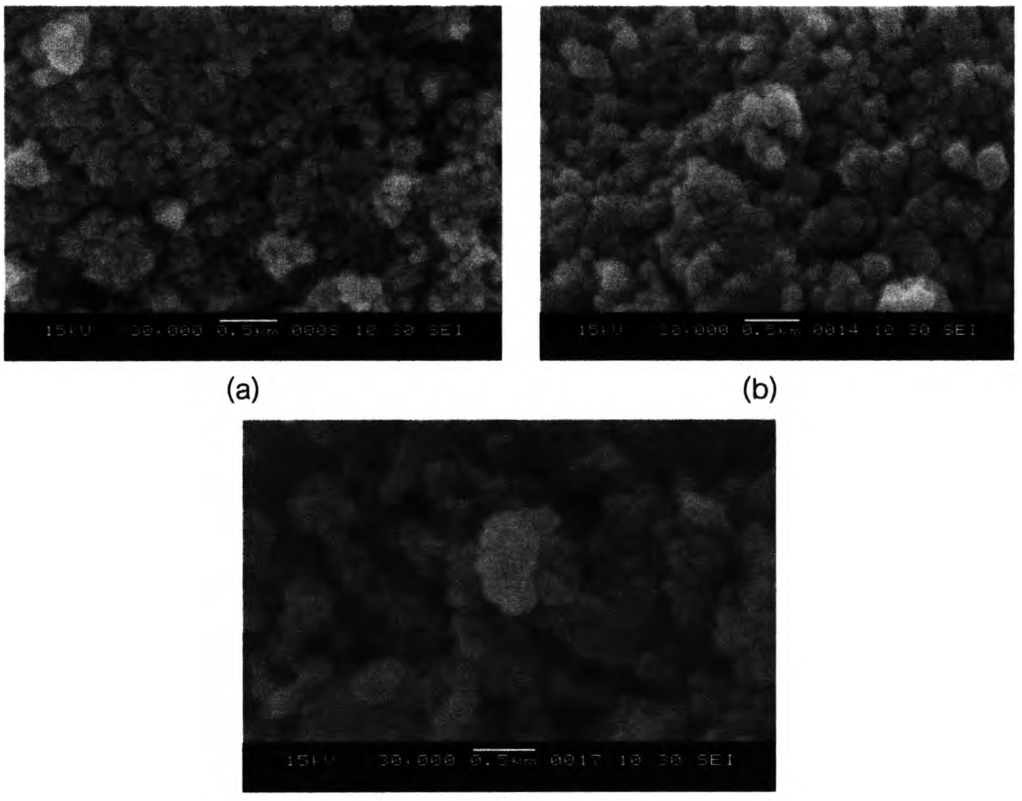

(a) (b)

(c)

Figure 4.14 SEM micrographs of (a) AMMO-g-SiO_2, (b) AMMO-g-RHS, and (c) AMMO-g-CCS

4.2.5 Thermal Properties

4.2.5.1 Thermogravimetric Analysis (TGA)

Thermogravimetric analysis (TGA) was used to characterize and measure silane coupling agents (i.e., vinyltrimethoxysilane (VTMO) and 3-aminopropyltrimethoxysilane (AMMO)) content grafted on surface of silica. The values of decomposition temperature (Td) indicated the processing and manufacturing temperature without initiating a process of decomposition.

TGA thermograms of AMMO grafted on surface of commercial silica, RHS, and CCS as displayed in Figure 4.15 and Table 4.5 comprised of three stages. The first stage in a temperature range of 90-110^{o}C was due to moisture decomposition. The second one at 190-240^{o}C was a decomposition of AMMO and the last one attributed to complete volatile of AMMO was around 475-500^{o}C. As shown in these thermograms, the char residues at 750^{o}C of AMMO-g-SiO_2, AMMO-g-RHS, and AMMO-g-CCS was 81.72%, 87.86%, and 85.78%, respectively; hence the percentage of AMMO grafting on SiO_2, RHS, and CCS was 14.51%, 9.97%, and 12.43%, respectively.

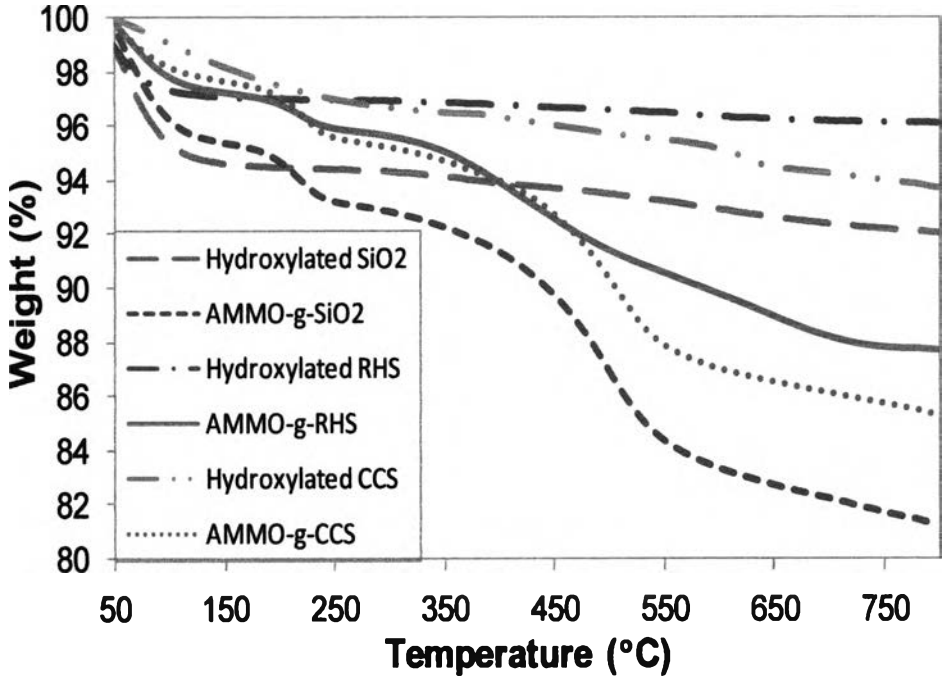

Figure 4.15 TGA thermograms of AMMO-g-SiO_2, AMMO-g-RHS, and AMMO-g-CCS

From TGA thermograms of hydroxylated SiO_2, hydroxylated RHS, and hydroxylated CCS, it was found that hydroxylated RHS had the most thermal stability when compared to hydroxylated SiO_2 and hydroxylated CCS. This result might be from purity of silica as mentioned in the topic of 4.1.2, therefore the purity control of silica is the most important factor that had an effect on grafting.

Table 4.5 TGA data of AMMO grafted on commercial silica, RHS, and CCS

Sample	Td (°C) (Onset)			Percent weight loss (%)			Residue (%)
	First	Second	Third	At 100 °C	At 250 °C	At 600°C	At 750 °C
AMMO-g-SiO_2	87.05	191.93	436.61	3.77	6.74	16.67	81.72
AMMO-g-RHS	90.84	197.98	356.06	2.17	4.05	10.18	87.86
AMMO-g-CCS	100.10	198.53	443.21	1.81	4.38	12.95	85.78

TGA curves of VTMO-g-SiO_2 and VTMO-g-RHS as displayed in Figure 4.16 and Table 4.6 consisted of two decomposition stages. The first stage around 80-100°C was due to the absorbed moisture in commercial silica/RHS and to the water as by-product from hydrolysis and condensation in silylation reaction of VTMO [40].

The second one around 540°C for VTMO-g-SiO_2 and 560°C for VTMO-g-RHS was due to the decomposition of vinyltrimethoxysilane. Regarding these two thermograms, VTMO-g-SiO_2 and VTMO-g-RHS could produce 92.41% and 90.59% of char residues at 750°C, respectively. Therefore, percentage of VTMO grafting on SiO_2 and RHS was 4.83% and 6.38%, respectively. Comparing the percentage of grafting between VTMO and AMMO, it could be concluded that AMMO had higher grafting efficiency grafting onto the silica surface than VTMO. From TGA curve, hydroxylated RHS showed better thermal stability than that of hydroxylated SiO_2.

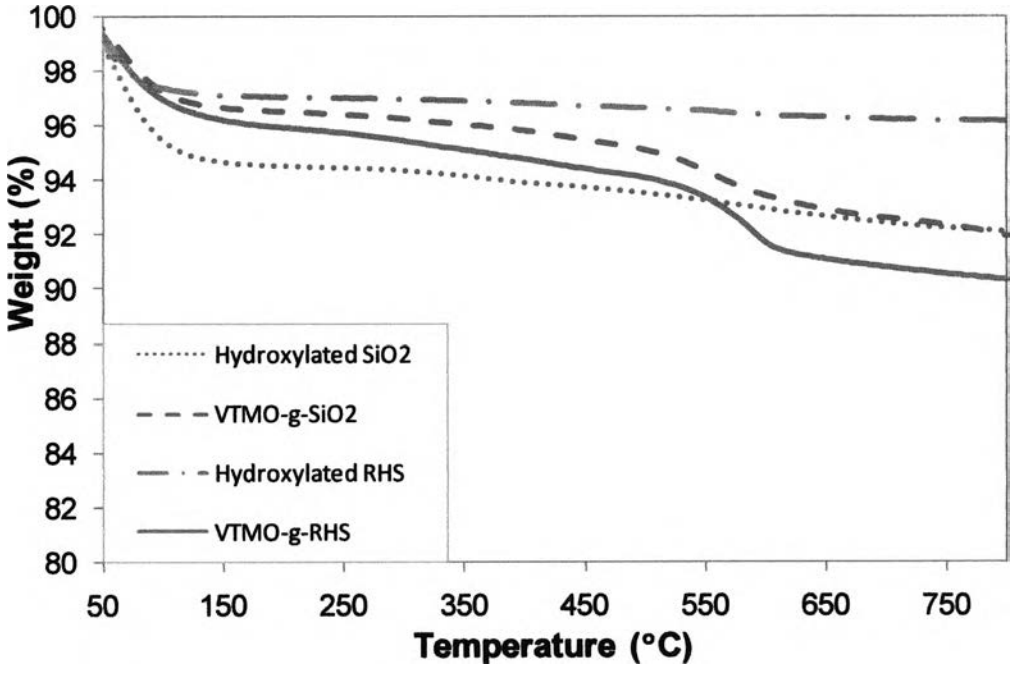

Figure 4.16 TGA thermograms of VTMO-g-SiO_2 and VTMO-g-RHS

From TGA curve, it was also found that the weight loss of hydroxylated RHS had more stable than that of hydroxylated SiO_2, therefore it could be concluded that the purity of silica had an influenced on silane grafting as described above.

Table 4.6 TGA data of VTMO grafted on commercial silica and RHS

Sample	Td (°C) (Onset)		Percent weight loss (%)		Residue (%)
	First	Second	At 100 °C	At 600 °C	At 750°C
VTMO-g-SiO_2	85.23	538.91	2.76	6.53	92.41
VTMO-g-RHS	90.18	563.09	3.03	8.22	90.59

4.3 Characterization of SSilatrane, RHSilatrane, and CCSilatrane

Silica was reacted with triethanolamine in ethylene glycol by hydrolysis in one step to form silatrane glycol as equation displayed in Figure 4.17. The reaction time could be completed within 4 hrs in which the product was changed from clear liquid to viscous yellow liquid. After that, it was precipitated with acetonitrile and then dried in an oven at 85°C overnight. The white powder of silatrane glycol was obtained. In this work, silatrane glycol synthesized from commercial silica, rice husk silica, and corn cob silica was abbreviated as SSilatrane, RHSilatrane, and CCSilatrane, respectively.

In order to confirm the functional group and chemical structure of synthesized SSilatrane, RHSilatrane, and CCSilatrane, they were characterized by FTIR, ^{29}Si NMR, ^{13}C NMR and ^{1}H NMR as discussed in the next topic.

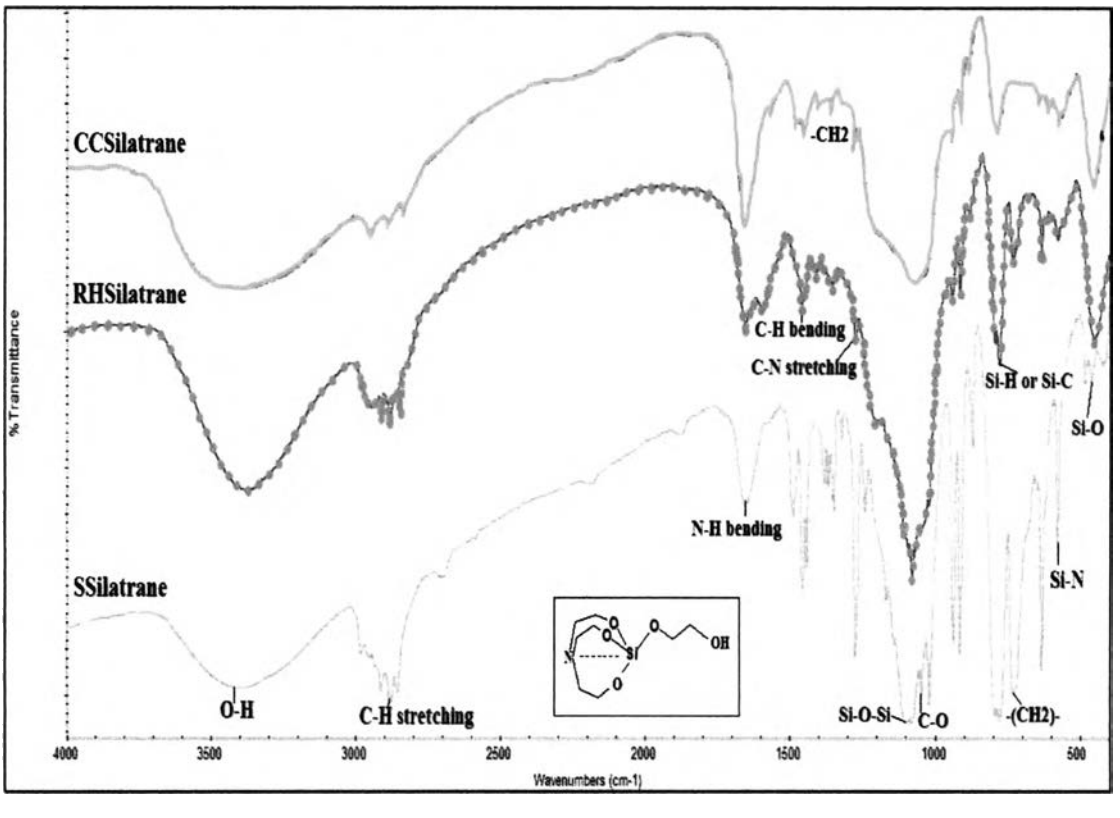

Figure 4.18 FTIR of SSilatrane, RHSilatrane, and CCSilatrane

4.3.2 Chemical Structure by ^{29}Si NMR Technique

Silatrane glycol consisted of a transannular Si-N bond that created a pentacoordinate silicon coupled with a tricyclic ring as chemical structure shown in Figure 4.17. Although FTIR technique could indicate the functional group of silatrane compound but it could not confirm a pentacoordinate Si-N dative bond in its structure; therefore, ^{29}Si NMR technique was used to investigate this Si-N bond.

From spectra shown in Figure 4.19, the peak in a range of -99 to -100 ppm indicated a pentacoordinate Si with a transannular dative bond in which Si atom was interacted with N atom of triethanolamine [7-9]. As for the signal peak at –108 to -110 ppm, it was assigned to siloxane structure as mentioned in 4.2.2 [20-23]. All synthesized silatrane similarly showed these two peaks confirming the structure of synthesized silatrane.

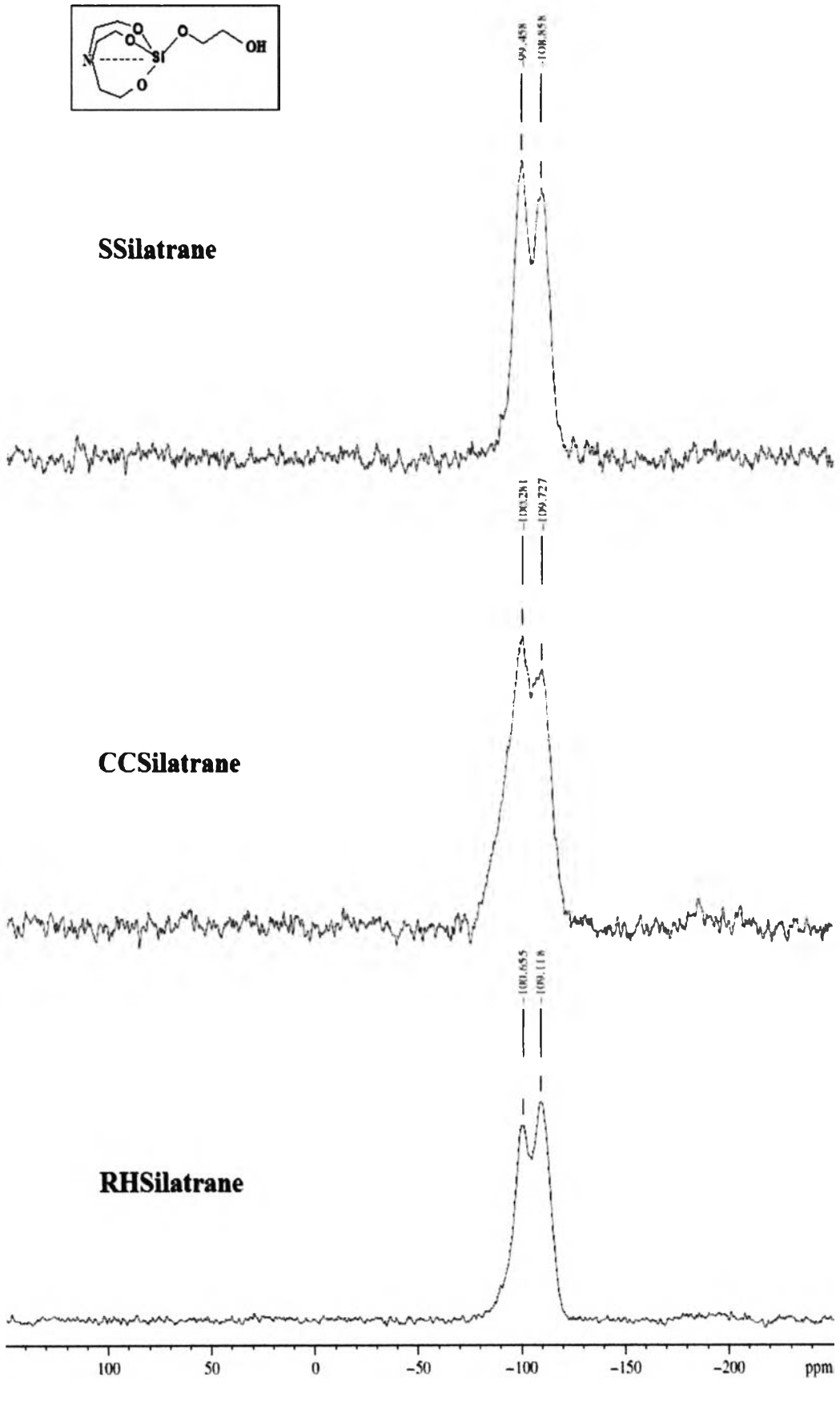

Figure 4.19 ^{29}Si NMR of SSilatrane, RHSilatrane, and CCSilatrane

4.3.3 Chemical Structure by ^{1}H NMR Technique

^{1}H NMR was used to investigate the structure of silatrane complex. SSilatrane, RHSilatrane, and CCSilatrane were dissolved in dimethyl sulfoxide (DMSO). The ^{1}H NMR spectra of all synthesized silatrane shown in Figure 4.20 were similar. The strong peak at 2.53-2.49 ppm indicated the proton atom in CH_2-N; whereas the other two peaks at 3.29-3.27 ppm and 3.38-3.37 ppm designated to the H-atoms in -O-CH_2-C-, and CH_2-O bonds of triethanolamine. The other intense peak at 3.75-3.71 ppm indicated proton atoms in CH_2-OH of ethylene glycol. Finally, the tiny peak at 8.73-8.37 ppm was assigned to the dative bond between Si and N atom [20-23].

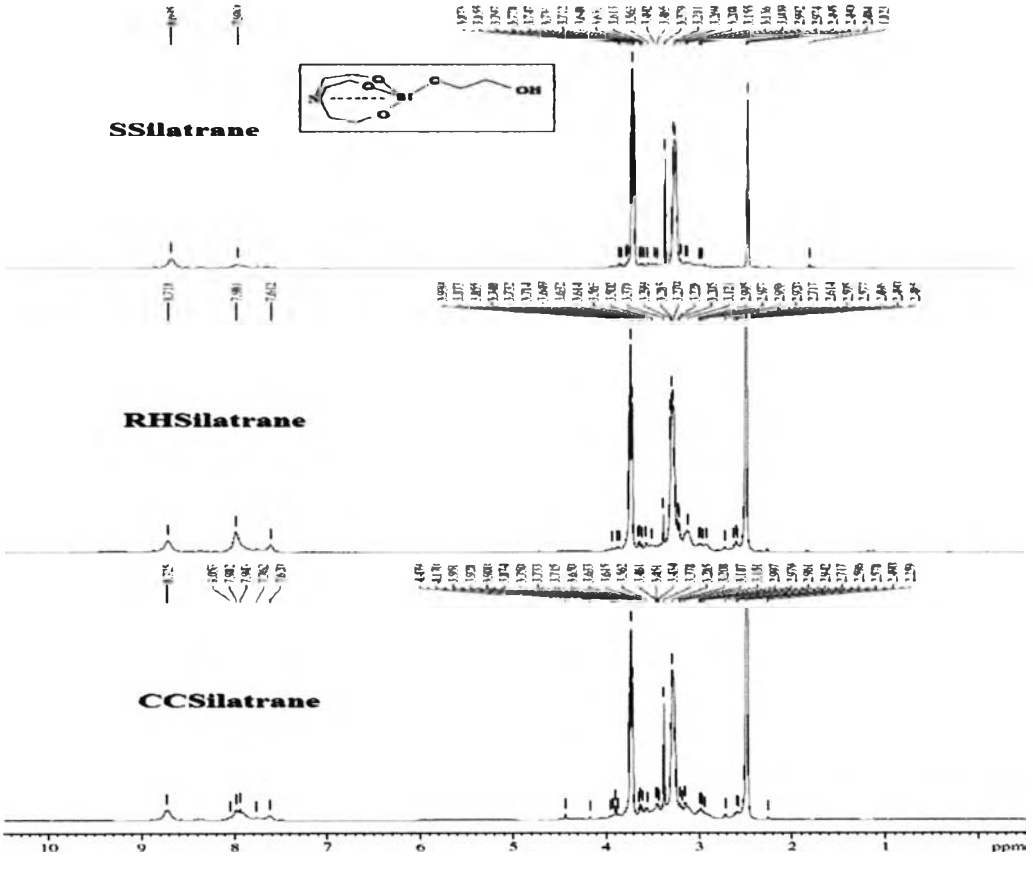

Figure 4.20 ^{1}H NMR of SSitatrane, RHSilatrane, and CCSilatrane

4.3.4 Chemical Structure by ^{13}C Technique

^{13}C-NMR spectra of SSilatrane, RHSilatrane, and CCSilatrane shown in Figure 4.21 displayed very strong intensity of the peaks at 60.08 - 60.12 ppm and 57.43- 57.64 ppm which were designated as the c- atoms in CH_2-O and CH_2-N bonds, respectively. In addition, small peak at 68.68-63.82 ppm can be noticed in SSilatrane and

CCSilatrane, which was attributed to the C-atoms in CH_2-OH of glycol part in silatrane [20-23].

According to all the NMR results, when comparing to SSilatrane or silatrane prepared from commercial silica, it can be concluded that silatrane glycol was successfully synthesized by hydrolysis reaction using silica extracted from agricultural wastes (i.e., rice husk and corn cob) as a starting material.

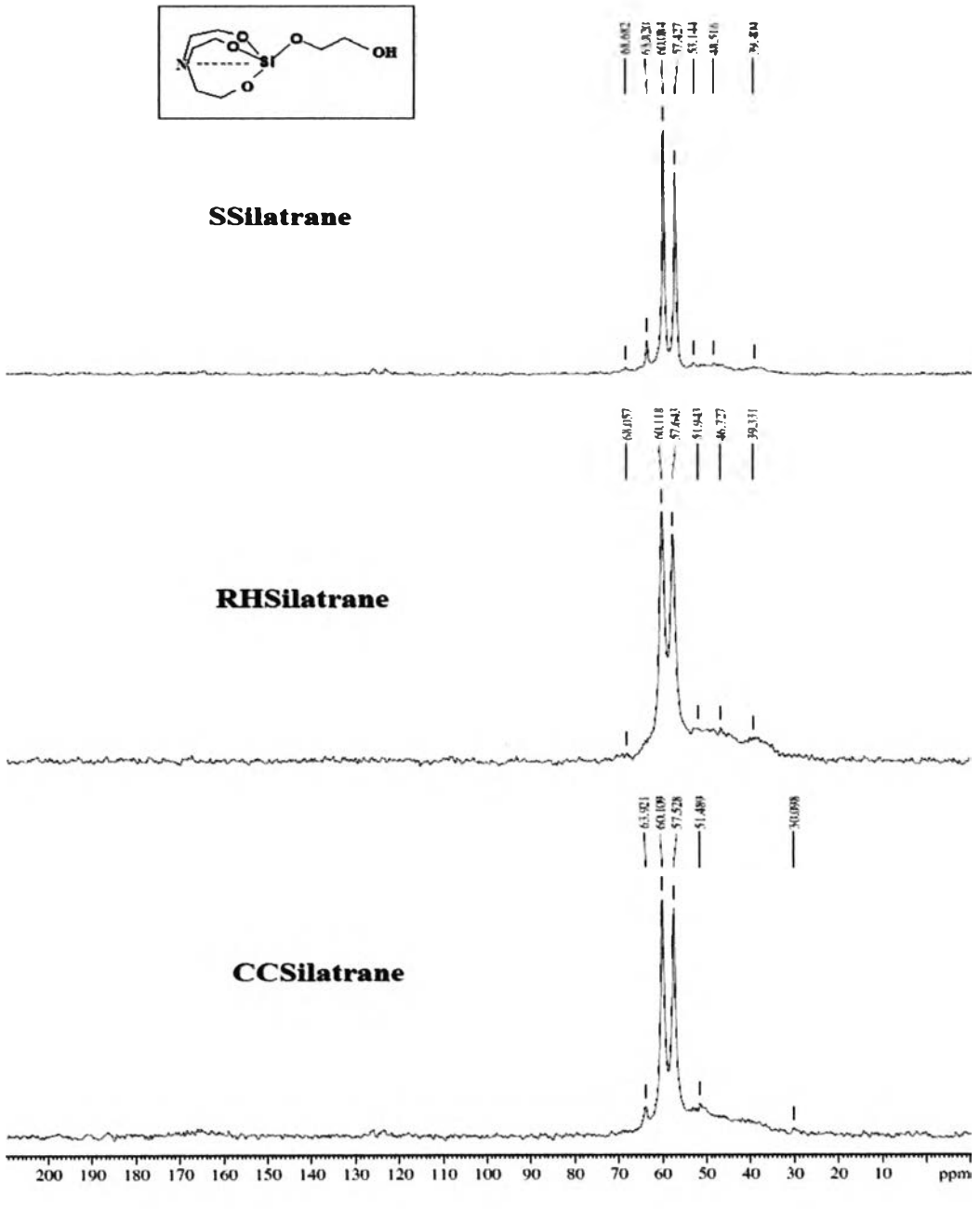

Figure 4.21 ^{13}C NMR of SSilatrane, RHSilatrane, and CCSilatrane

4.3.5 Particle Size and Surface Area Analysis

The particle size and specific surface area of SSilatrane, RHSilatrane and CCSilatrane were determined by using laser particle size analyzer and surface area analyzer in accordance to Brunauer-Emmett-Teller (BET) method, respectively. Table 4.7 showed the particle size and surface area of SSilatrane, RHSilatrane, and CCSilatrane. It revealed that CCSilatrane had the smallest particle size and highest BET specific surface area with 5.98 μm and 100.26m^2/g, respectively. As a result, the particle size of SSilatrane, RHSilatrane, and CCSilatrane were in line with SEM images as illustrated in Figure 4.22.

Interestingly, when comparing to the data presented in Table 4.4, we can see that all the synthesized silatrane had smaller particle size and lower surface area than their silica counterparts, except for CCSilatrane that had smaller particle size and higher area than corn cob silica. Thus, based on these results, it was expected that ABS nanocomposite containing CCSilatrane will have good mechanical performance.

Table 4.7 Particle size and surface area of various silatrane

Samples	Particle size (micron)	BET surface area, N_2 (m^2/g)
SSilatrane	17.55	30.17
RHSilatrane	12.83	37.42
CCSilatrane	5.98	100.26

4.3.6 Morphological Studies

The morphological characteristics of SSilatrane, RHSilatrane, and CCSilatrane were determined by using a scanning electron microscope. The SEM micrographs of all silatrane were illustrated in Figure 4.22. All synthesized silatrane was white fine powder as seen by naked eye. Under microscope, the particle size of each silatrane was smaller than 0.5 μm or in a range of nanometer level. Similar trend from the particle size analysis presented in Table 4.7, SSSilatrane had the biggest particle size whereas the CCSilatrane exhibited the smallest particle size. Nevertheless, each silatrane obviously showed an agglomeration of the particles, resulted in higher particle size of the silatrane when measerred by the laser particle size analyzer

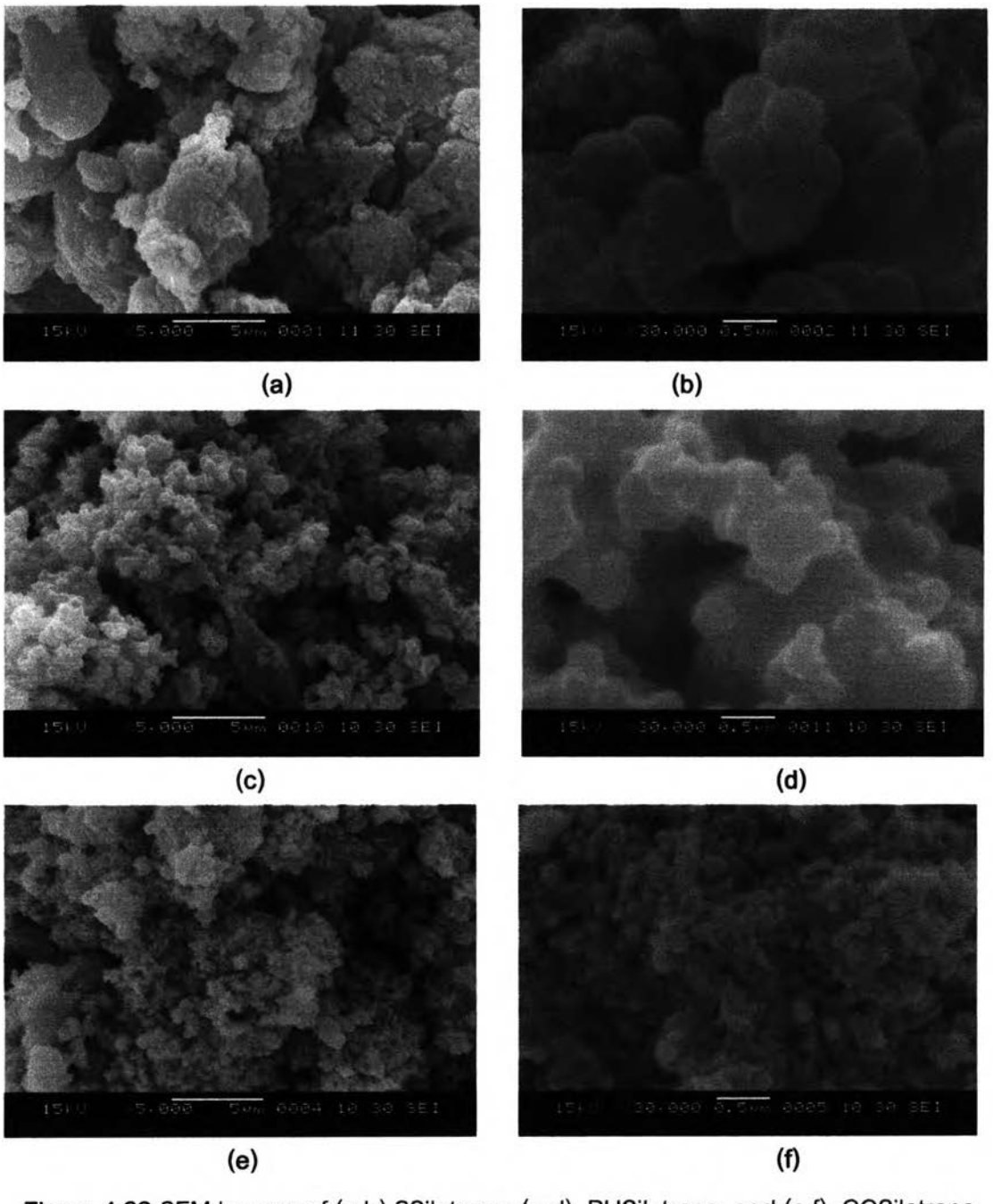

Figure 4.22 SEM images of (a,b) SSilatrane, (c,d) RHSilatrane, and (e,f) CCSilatrane

4.3.7 Crystallinity by XRD Technique

The crystal structure of SSilatrane, RHSilatrane, and CCSilatrane were determined by using X-ray diffractometer (XRD). All the silatrane shown in Figure 4.23 was crystalline structure because the diffraction 2θ peak appeared clearly. The small 2θ peaks of SSilatrane at 5°, 8.5°, 9.4°, 11.8°, and 15°, were assigned to basal spacing of 17.18 A°, 10.43 A°, 9.4 A°, 7.5 A°, and 5.6 A°, respectively. For the 2θ peaks of RHSilatrane, the peaks at 3.7°, 7°, 10.4°, 13.7°, 17°, and 20° were indicated

as the basal spacing of 23.6 A^{o}, 12.5 A^{o}, 8.5 A^{o}, 6.4 A^{o}, 5.2 A^{o}, and 4.3^{o}, respectively. The 2θ peaks of CCSilatrane at 2.8^{o}, 6.2^{o}, 9.5^{o}, 12.9^{o}, 16.2^{o}, and 19.6^{o} were designated the basal spacing of 31.6 A^{o}, 14.3 A^{o}, 9.3 A^{o}, 6.9 A^{o}, 5.5 A^{o}, and 4.5^{o}, respectively. As a result, it was found that all synthesized silatrane was more crystallite more than its starting material that might have affect on good mechanical properties of ABS. Moreover, SSilatrane showed crystallinity obviously in comparison to XRD pattern of commercial silica as shown previously.

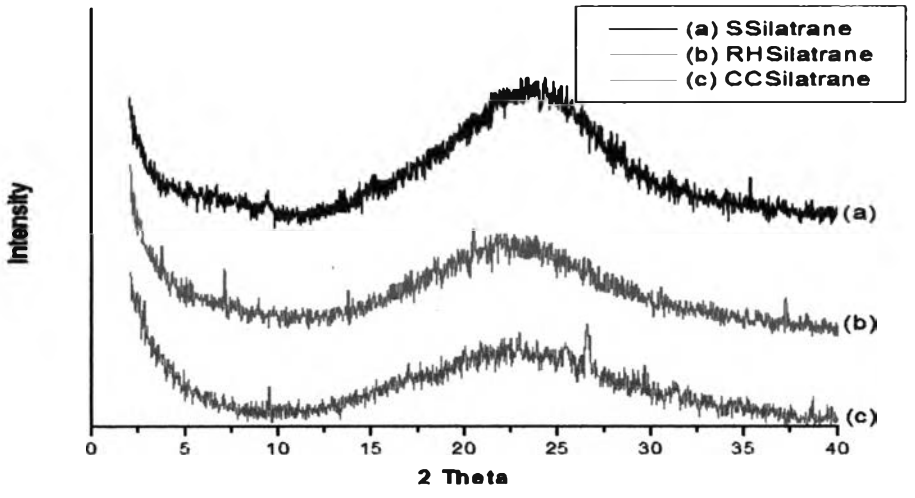

Figure 4.23 XRD patterns of (a) SSilatrane, (b) RHSilatrane, and (c) CCSilatrane

4.3.8 Thermal Properties

The thermal stability of white powder of SSilatrane, RHSilatrane, and CCSilatrane was determined by measuring their weight loss during heating under nitrogen atmosphere using thermogravimetric analysis (TGA). TGA curves presented in Figure 4.25 revealed that all synthesized silatrane degraded in three decomposition stages. The first stage between 70^{o}C and 110^{o}C was because of the moisture decomposition. The second one occurred between 160^{o}C and 220^{o}C was due to the decomposition of ethylene glycol and triethanolamine, used as solvent and reactant, respectively in dimerization reaction [20-23] as shown in Figure 4.24.

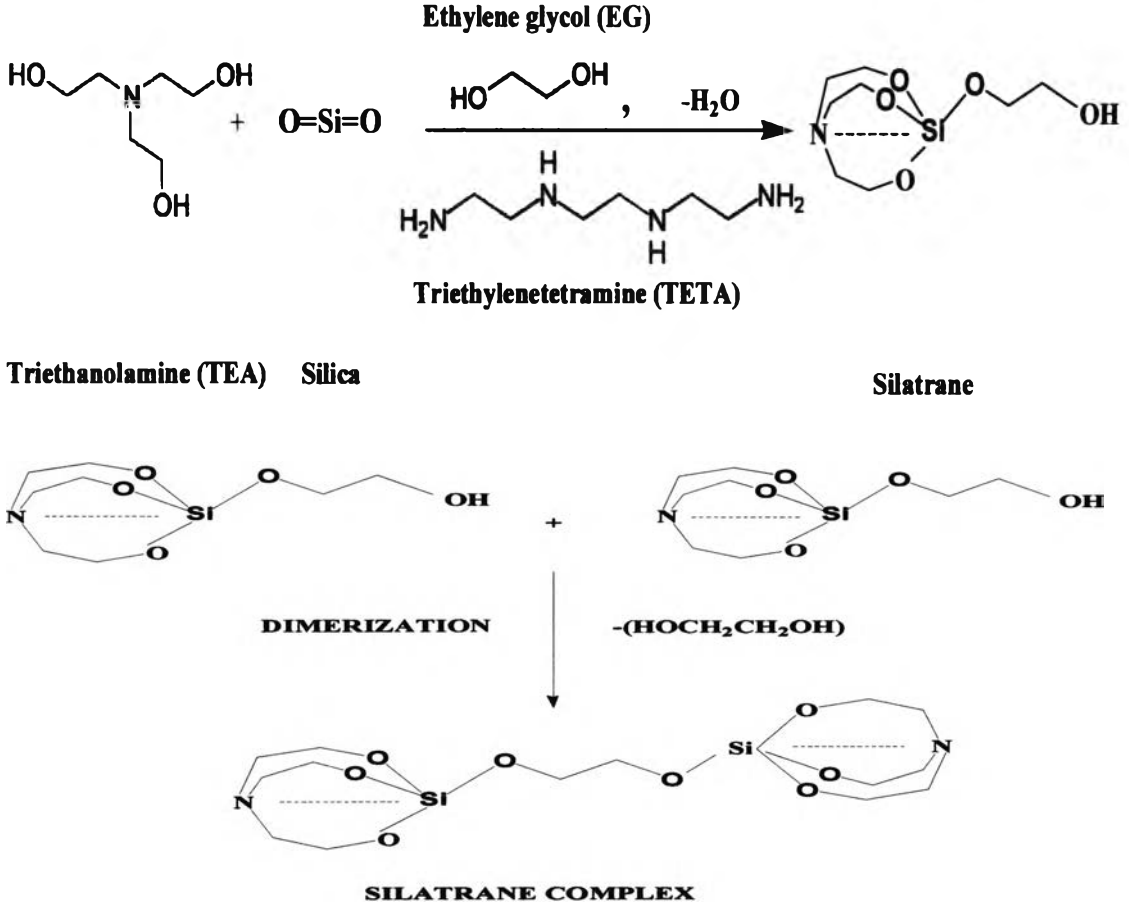

Figure 4.24 Schematic of dimerization in silatrane complex synthesis

The third decomposition step occurred in the range of 320-350°C, corresponding to the thermal decomposition temperature (Td) of organic ligands [39]. In addition, it was also found that the percentage of weight residue of SSilatrane, RHSilatrane, and CCSilatrane at 600°C was 50.63%, 42.84%, and 54.85%, respectively. As a result of this high residue yield, thus the synthesized silatrane was expected to be used as an efficiently silicon containing flame retardant additive for improving fire retardant properties of ABS, as will be discussed shortly.

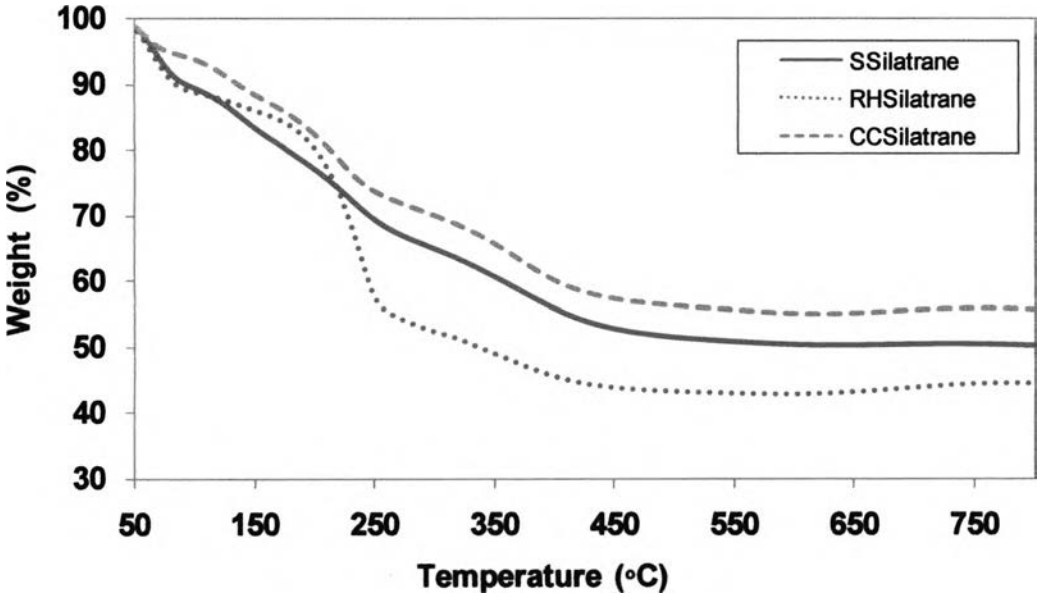

Figure 4.25 TGA curves of SSilatrane, RHSilatrane, and CCSilatrane

Table 4.8 TGA data of SSilatrane, RHSilatrane, and CCSilatrane

Sample	Td (°C) (Onset)			Percent weight loss (%)	Residue (%)
	First	Second	Third	At 100 °C	At 600 °C
SSilatrane	80.73	167.23	336.24	10.61	50.63
RHSilatrane	69.54	160.23	330.06	11.20	42.84
CCSilatrane	92.47	164.64	339.46	6.62	54.85

4.4 Characterization of ABS Nanocomposites

4.4.1 Chemical Structure by FTIR Technique

The change of functional group contained in ABS nanocomposites was investigated by FTIR as shown in Figure 4.26 FTIR spectrum of Neat ABS showed C-H stretching at 2900-2800 cm^{-1}, C≡N groups at 2235 cm^{-1}, -C=N groups at 1635 cm^{-1}, Phenyl groups at 1485 cm^{-1}, CH_2 or $-CH_3$ at 1480-1400 cm^{-1}, $CH=CH_2$ at 1000-970 cm^{-1}, C=C-H at 695 cm^{-1}, and $-(CH_2)-$ at 698 cm^{-1} indicating double bond, cyano groups, and phenyl in ABS structure.

When OMT was blended in ABS, the existence of Si-O bonding at 500-450 cm^{-1} and Si-O-Si vibration at 1100-1000 cm^{-1}, and Si-O at 455 cm^{-1} was found apparently. These two peaks were attributed to the silicate layer in organoclay.

As for FTIR spectra of ABS/OMT/VTMO-g-SiO_2 or ABS/OMT/VTMO-g-RHS, the broad peak of siloxane at 1100-1000 cm^{-1} was noticed obviously. In addition, it was also found that the increase of intensity peak of C-H stretching at 2900-2800 cm^{-1} , C=C at 1600-1560 cm^{-1}, and $-CH_2$ or $-CH_3$ at 1480-1400 cm^{-1} was appeared drastically. This was due to VTMO grafted on silica surface.

When AMMO was blended with ABS/OMT, FTIR spectra of ABS/OMT/AMMO-g-SiO_2, ABS/OMT/AMMO-g-RHS, and ABS/OMT/AMMO-g-CCS showed peak of C-NH_2 stretching at 1200 cm^{-1} and Si-C bonding at 800-700 cm^{-1}, and Si-O-Si vibration at 1100-1000 cm^{-1}. This was because of amino group in AMMO structure.

Regarding FTIR spectra of ABS/OMT/AMMO-g-SiO_2/SSilatrane, ABS/OMT/AMMO-g-RHS/RHSilatrane, and ABS/OMT/AMMO-g-CCS/CCSilatrane, it was found that the high intensity of -C-N stretching at 1230-1100 cm^{-1}, Si-O-Si vibration at 1100-1050 cm^{-1}, C-NH_2 bonding at 1150-1030 cm^{-1}, and Si-C bonding at 800-700 cm^{-1} was appeared drastically when compared to other spectra. Because Si-N bonding at 595-560 cm^{-1} in silatrane structure was disappeared; therefore covalent bond of Si-C in silatrane structure appeared clearly. This result might had an impact on the increase of intensity peak at Si-C bonding.

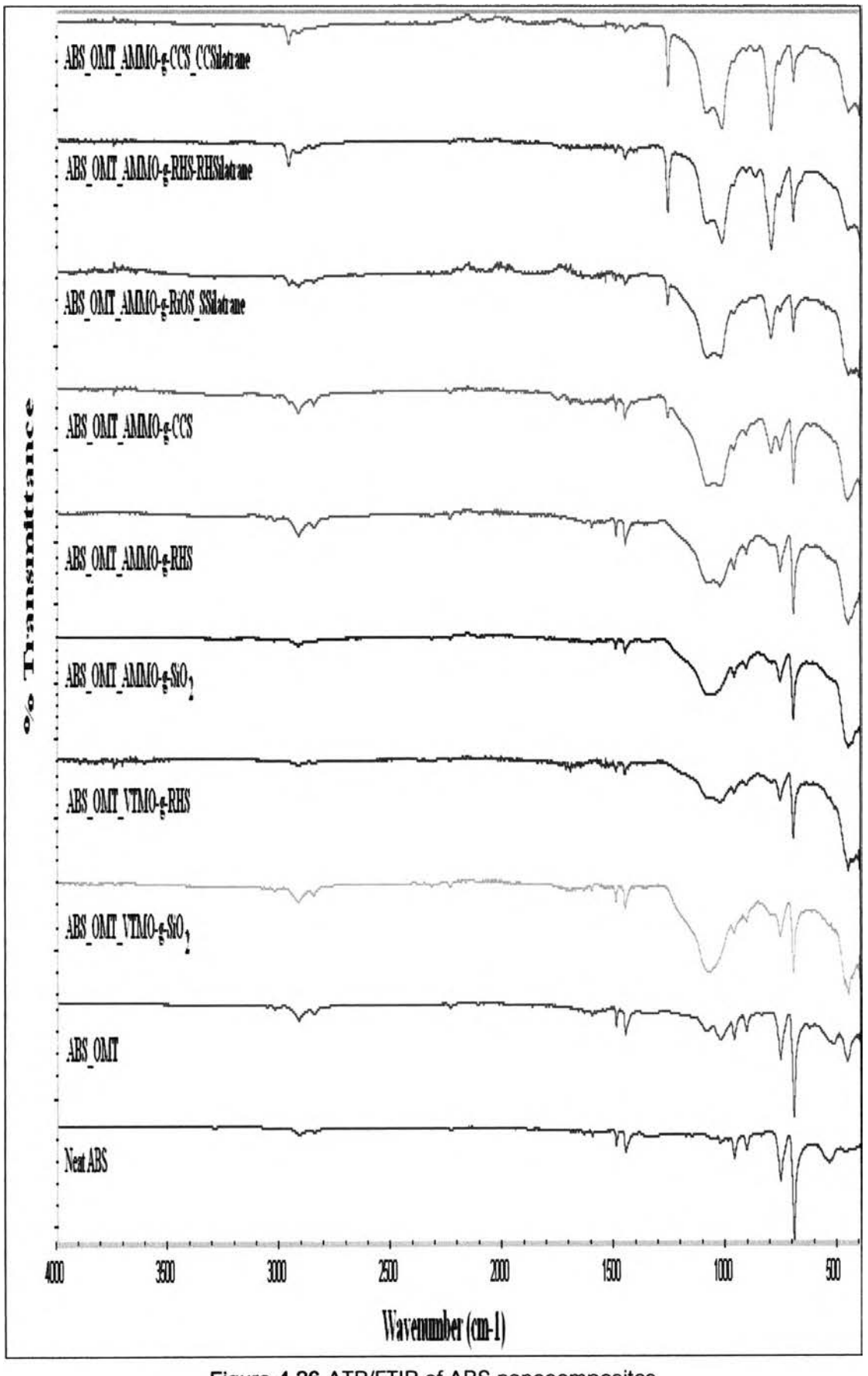

Figure 4.26 ATR/FTIR of ABS nanocomposites

4.4.2 Crystallinity by XRD Technique

The basal spacing of ABS nanocomposites was examined by using X-ray diffractometer (XRD). As shown in Figure 4.27. Two structures of nanocomposites can be found. Intercalated structure occurred where the polymer chain can be inserted between the silicate layers of clay and increased the basal spacing of the clay layers When the silicate layers are uniformly dispersed and separated in a polymer matrix, an exfoliated structure is obtained [11].

Regarding to the XRD patterns of Neat ABS and ABS with 5 wt% of OMT as shown in Figure 4.27 (b) and (c), it was found that neat ABS showed amorphous structure because no diffraction 2θ peak appeared. On the contrary, when 5 wt% of OMT was added into ABS, the 2θ peak at 2.4°, 4.9°, and 7.2° was found, corresponding to basal spacing of 36.55 A°, 18.01 A°, and 12.13 A°, respectively. This result was in agreement with the presence of silicate layers existing in an intercalated structure as TEM micrographs shown in Figure 4.32 (e) and (f).

When VTMO-g-SiO_2 / VTMO-g-RHS was blended with ABS and OMT as displayed in Figure 4.27 (d) and (e), it was found that the 2θ peak at 7.2° of OMT with an interlayer spacing of 12.13 nm was shifted to lower angle at $6.61\text{-}6.69^{\circ}$ with basal spacing of 13.2-13.36 nm; hence the increase of basal spacing was 1.07-1.23 nm. This phenomenon occurred from the intercalation of ABS chain into silicate layer of OMT, leading to a shift of the 2θ peak towards lower angle value corresponding to Bragg's equation; thus ABS/OMT/VTMO-g-SiO_2 and ABS/OMT/VTMO-g-RHS nanocomposites were intercalated structure, as evidenced by their TEM images presented in Figure 4.32 (a) -(d).

XRD patterns of AMMO grafted on three types of silica (RHS, commercial silica, and CCS) blended with ABS and OMT were shown in Figure 4.27 SiO_2 (e), RHS (f), and CCS (g), respectively. It was found that the intensity of 2θ peak at 22° was decreased and the 2θ peak at 2.4° was shifted drastically towards lower angle, therefore their structure might be partially exfoliated structure. However, it can not conclude solely from XRD pattern how their structure were, they must be confirmed by using TEM micrographs as illustrated in Figure 4.33 (a)-(d).

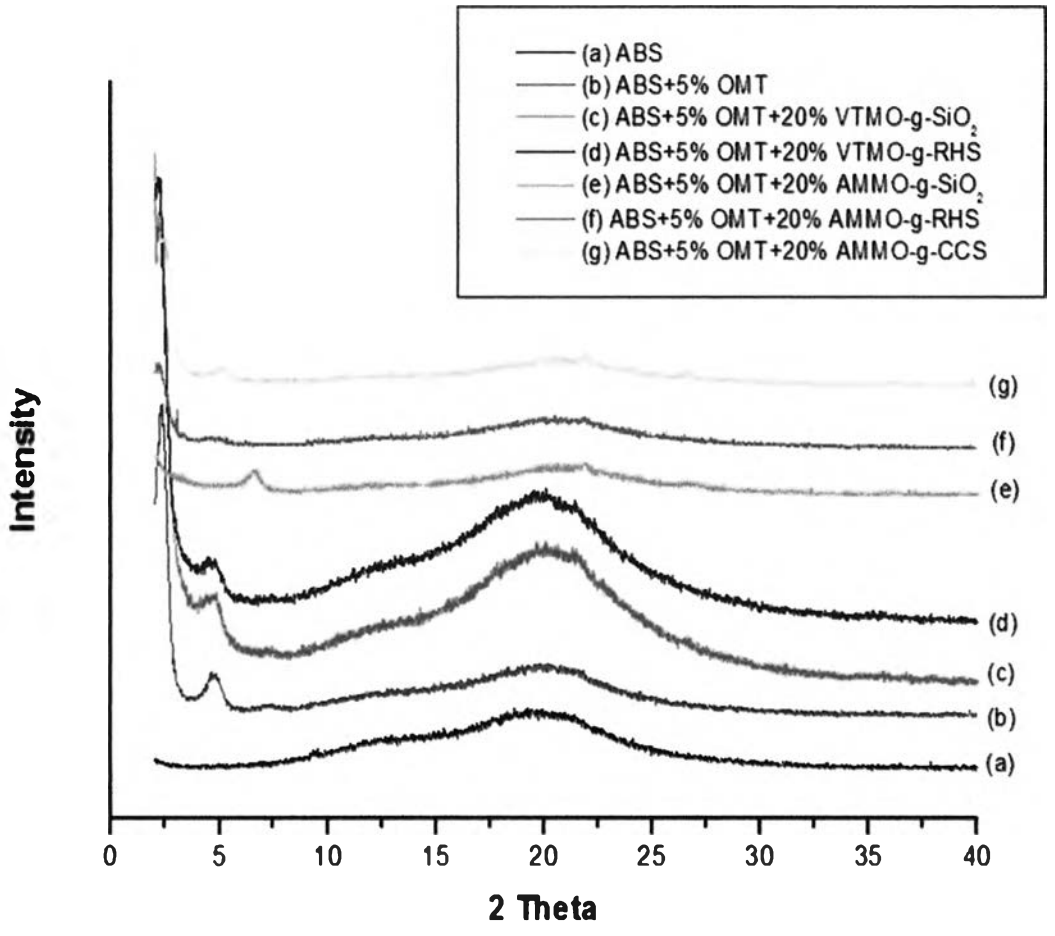

Figure 4.27 XRD patterns of ABS/OMT/VTMO-g- silica and ABS/OMT/AMMO-g-silica nanocomposites

The effect of type of silica on crystallinity of ABS nanocomposites was studied by using XRD patterns as displayed in Figure 4.28 It revealed that ABS with 5wt% of OMT and 20wt% of ungrafted SiO_2 showed cristobalite peak as same as ABS/OMT/Ungrafted RHS and ABS/OMT/Ungrafted CCS. This resulted from inorganic content or ungrafted silica.

On the other hand, ABS/OMT/AMMO-g-SiO_2, ABS/OMT/AMMO-g-RHS, and ABS/OMT/AMMO-g-CCS had no peak of cristobalite appeared and the diffraction peak of silicate layer of OMT at 4.8^{o} was shifted slightly to the lower angle in comparison to ABS/OMT/Ungrafted silica. This was due to the fact that silane coupling agent could promote the good dispersion of silica in SAN matrix. In addition, it was found that ABS/OMT/AMMO-g-SiO_2 showed intercalated structure as well as ABS/OMT/AMMO-g-RHS and ABS/OMT/AMMO-g-CCS.

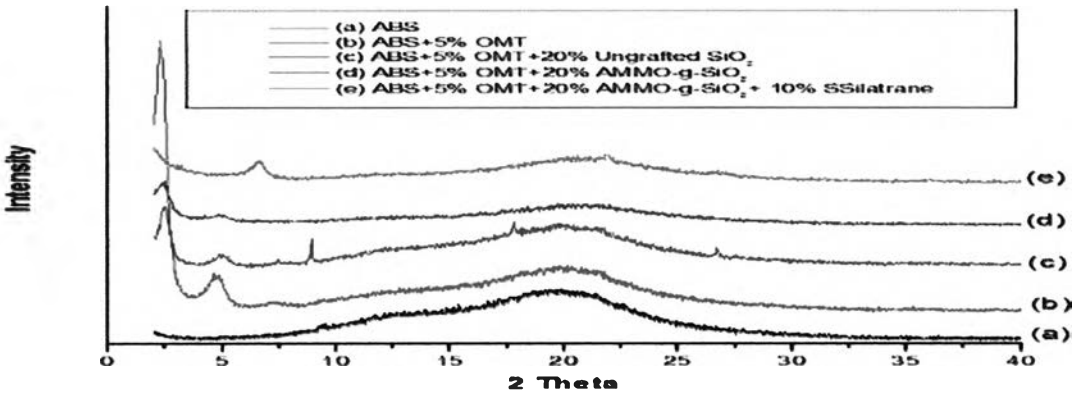

(a)

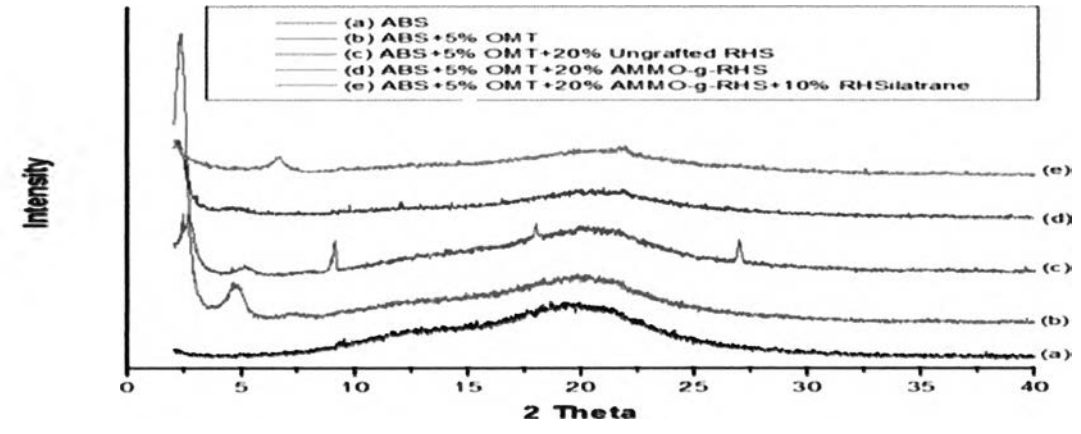

(b)

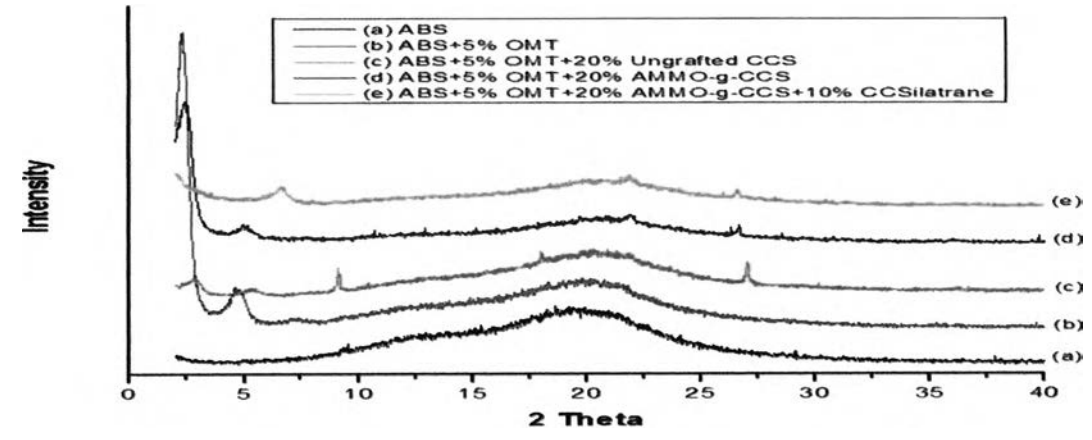

(c)

Figure 4.28 XRD patterns of (a) ABS/OMT/AMMO-g-SiO_2/SSilatrane, (b) ABS/OMT/AMMO-g-RHS/RHSilatrane, and (c) ABS/OMT/AMMO-g-CCS/CCSilatrane nanocomposites

When synthesized silatrane (SSilatrane, RHSilatrane, and CCSilatrane) was blended with ABS with 5wt% of OMT and 20 wt% of AMMO grafted silica (AMMO-g-SiO_2, AMMO-g-RHS, and AMMO-g-CCS), it was found that the diffraction peak of siloxane at 6.5° was noticed. Normally, it was appeared at 9.3° as discussed previously in topic 4.2.3. This might be because the dispersion of silatrane particles had an influence on separation between silicate layer of OMT. Furthermore, the diffraction peak of silicate layer of OMT was disappeared. This result indicated that ABS/OMT/AMMO-g-SiO_2/SSilatrane, ABS/OMT/AMMO-g-RHS/RHSilatrane, and ABS/OMT/AMMO-g-CCS/CCSilatrane might be partially exfoliated structure. However, their structure will be confirmed with TEM images as illustrated shortly.

4.4.3 Morphological Studies

4.4.3.1 Scanning electron microscopy (SEM)

SEM image of neat Pure was exhibited in Figure 4.29 (a) for comparison, while Figure 4.29 (b), (c), (d), (e), (f), and (g) corresponded to the SEM images of ABS/OMT, ABS/OMT/VTMO-g-SiO_2, ABS/OMT/VTMO-g-RHS, ABS/OMT/AMMO-g-SiO_2, ABS/OMT/AMMO-g-RHS, and ABS/OMT/AMMO-g-CCS nanocomposites, respectively.

Figure 4.29 (b) revealed that it was not clear to observe OMT particles in the ABS/OMT nanocomposites because of their small particle size in the nanometer range. The distribution of OMT particles was, however, clearly observed by the TEM analysis, which will be discussed shortly. For nanocomposites containing silane grafted SiO_2 , silane grafted RHS, and silane grafted CCS, the images in Figure 4.29 (c), (d), (e), and (f) showed that small silica particles were well dispersed and randomly distributed in the SAN phase as white spots but it was not clear enough to observe, therefore transmission electron microscope was used to investigate the morphology of ABS nanocomposites as evidenced by TEM images in Figure 4.32 and 4.33.

The SEM micrographs of fractured surface of (a) ABS/OMT/AMMO-g-SiO_2/SSilatrane , (b) ABS/OMT/AMMO-g-RHS/RHSilatrane, and (c) ABS/OMT/AMMO-g-CCS/CCSilatrane were illustrated in Figure 4.30. It was noticed obviously that there were some aggregated particles of fillers (AMMO-g-silica and silatrane) dispersed in SAN matrix and many voids at surface were obviously observed. This phenomenon led to the

defect of samples during impact and tensile testing, caused the decrease in mechanical properties when the filler loading increased as will be discussed later in the topic 4.4.6. In addition, it was also found that the fracture of samples occurred from phase separation between SAN matrix and filler as illustrated in Figure 4.30.

In this work, SEM-EDX was also used to confirm silicon containing on ABS/OMT/AMMO-g-RHS/RHSilatrane and ABS/OMT/AMMO-g-CCS/CCSilatrane nanocomposites as displayed in Figure 4.31. It was found that there were some agglomeration of silatrane particles dispersed in SAN matrix as illustrated in Figure 4.31 (a) and (c). Moreover, the silicon atoms containing on silatrane complex were shown apparently in Figure 4.31 (b) and (d) at approximately 1.5-2 keV. Therefore, preparation of ABS/OMT/AMMO-g-RHS/RHSilatrane and ABS/OMT/AMMO-g-CCS/CCSilatrane nanocomposites was achieved to study flammability and mechanical properties as explained later.

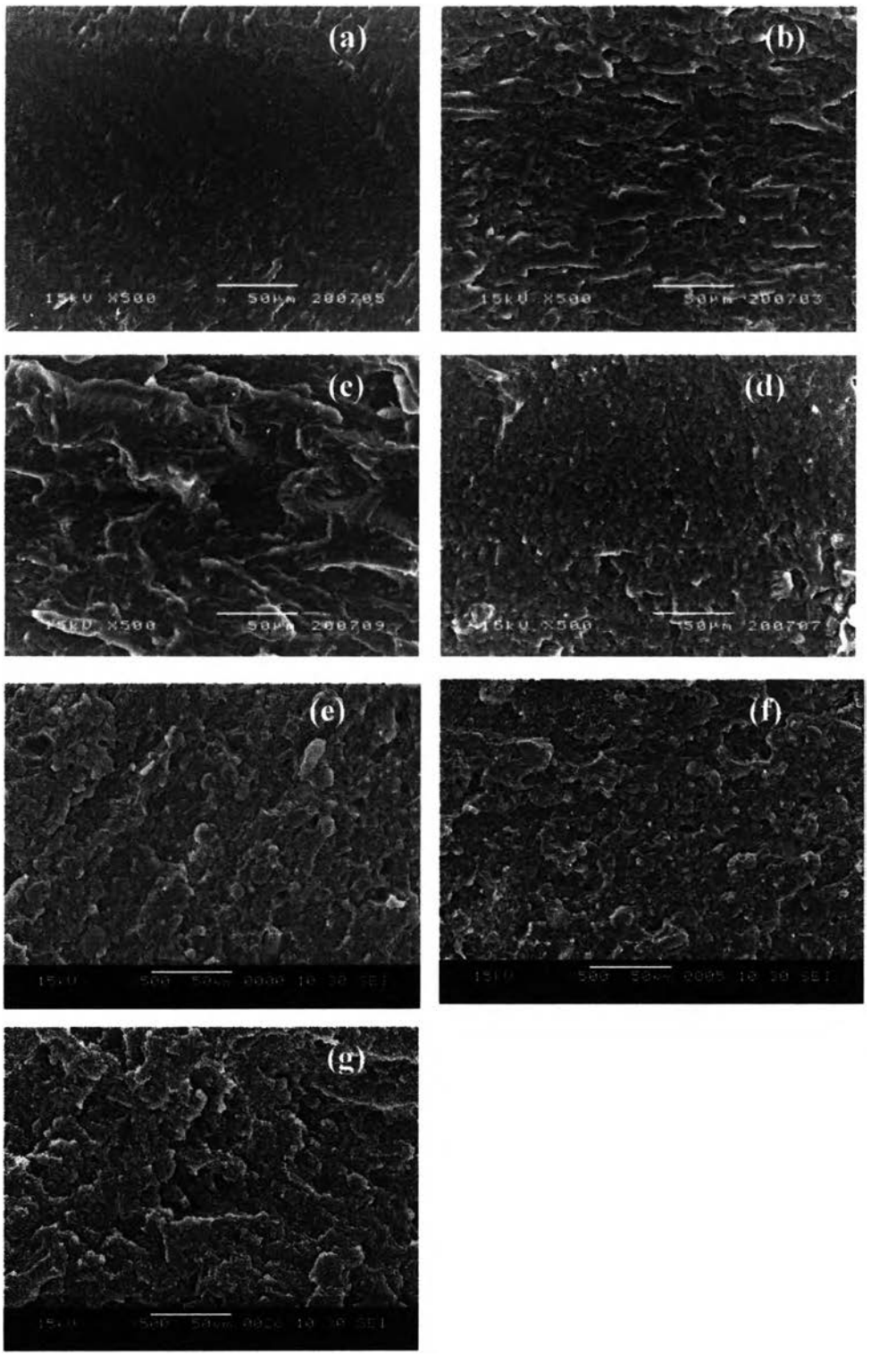

Figure 4.29 SEM images of (a) neat ABS, (b) ABS/OMT, (c) ABS/OMT/VTMO-g-SiO_2, (d) ABS/OMT/VTMO- g-RHS, (e) ABS/OMT/AMMO-g-SiO_2, (f) ABS/OMT/AMMO-g-RHS, and (g) ABS/OMT/AMMO-g-CCS, respectively

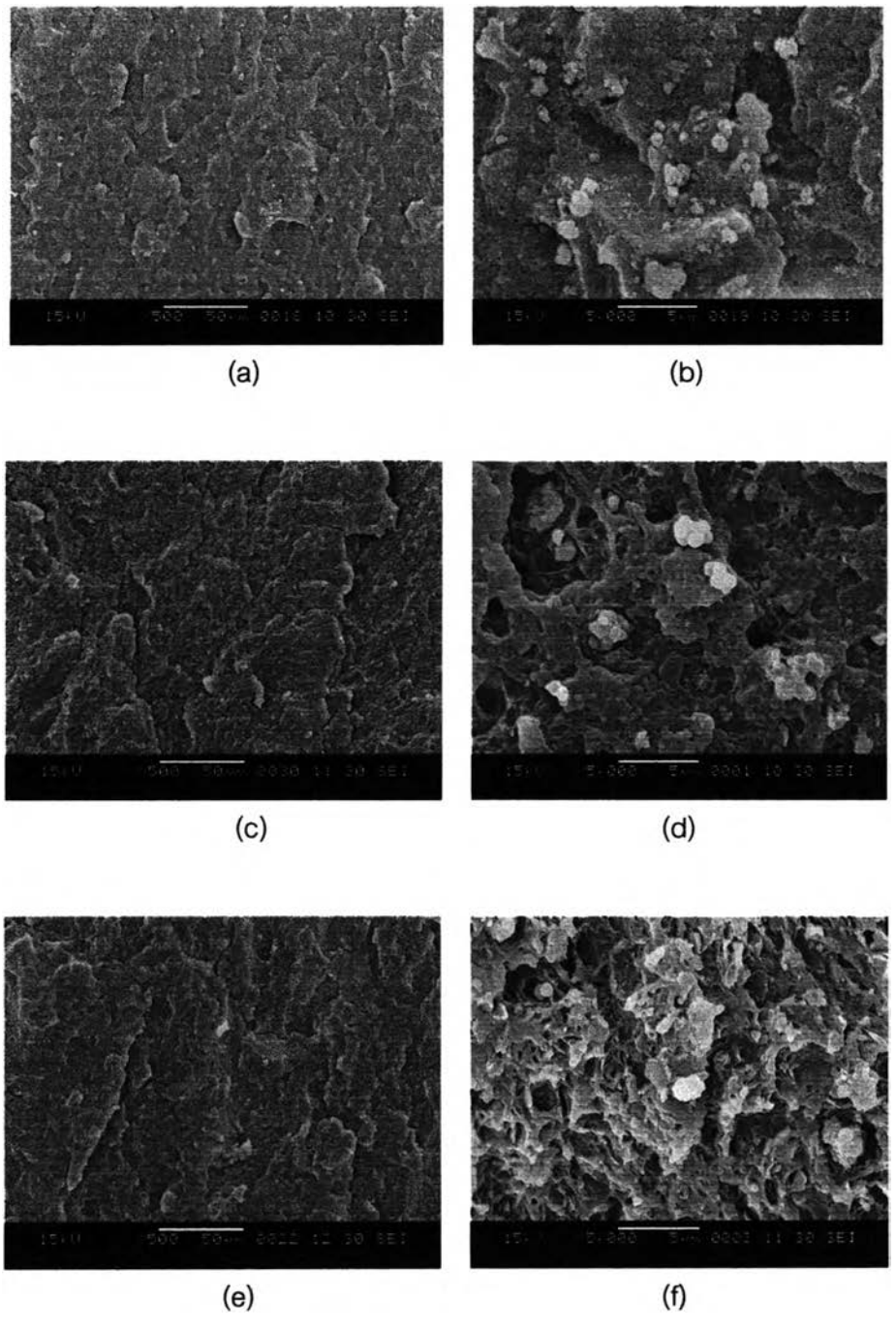

Figure 4.30 SEM images of (a,b) ABS/OMT/AMMO-g-SiO_2/SSilatrane, (c,d) ABS/OMT/AMMO-g-RHS/RHSilatrane, and (e,f) ABS/OMT/AMMO-g-CCS/CCSilatrane at lower magnification (x500) and higher magnification (x5,000), respectively

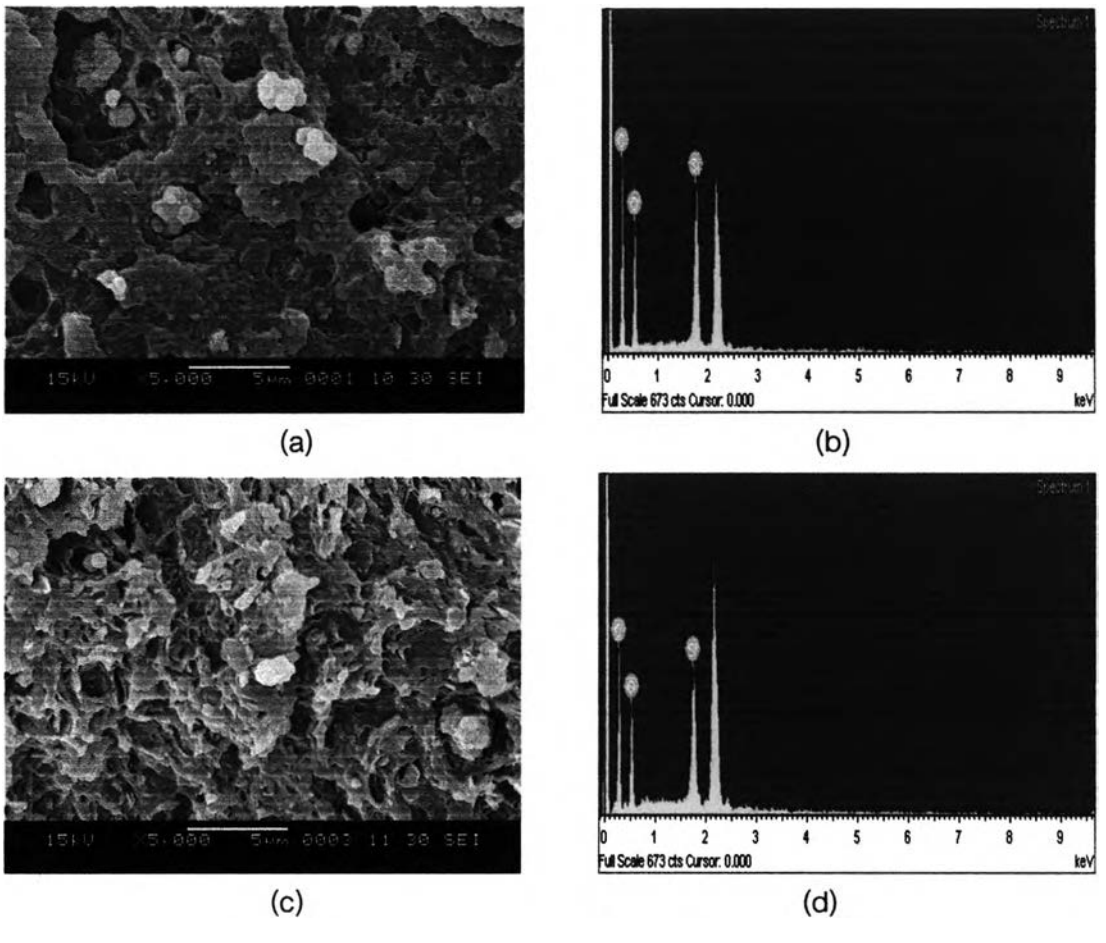

Figure 4.31 SEM-EDX micrographs of (a, b) ABS/OMT/AMMO-g-RHS/RHSilatrane and (c, d) ABS/OMT/AMMO-g-CCS/CCSilatrane

4.4.3.2 Transmission electron microscopy (TEM)

Transmission electron microscopy (TEM) was used to investigate morphology of ABS nanocomposites. TEM images for blends of ABS with filler (i.e., OMT, modified silica, and silatrane) were complicated due to ABS consisted of rubber particles or rubber phase and SAN matrix. In order to easily detect, the samples must be stained with a heavy metal oxide (OsO_4) to provide visual contrast with SAN matrix. On the contrary, OMT consisted of an aluminosilicate, thus it was easily differentiated from SAN matrix without staining. In the same way, modified silica and silatrane could be also noticed but their images were not as clear as OMT.

TEM images shown in Figure 4.32 revealed that ABS/OMT/VTMO-g-RHS and ABS/OMT/VTMO-g-SiO_2 nanocomposites were an intercalated structure. As for Figure 4.32 (e) and (f), TEM images of ABS/OMT nanocomposites at higher magnification (x200,000) revealed that OMT consisted of several silicate layer stacks and dispersed

in SAN matrix. Furthermore, it was found that OMT and VTMO-g-RHS/VTMO-g-SiO_2 were mainly distributed in SAN phase. The deep grey islands were rubber particles of butadiene. The black lines corresponded to clay layers of OMT. In addition, silica particles were also found to disperse and reside in the SAN phase of polymer. However, there were some agglomerate particles, which partially dispersed in rubber particles of butadiene and SAN matrix [25-29].

Regarding XRD patterns in Figure 4.27, the results could be confirmed with TEM image whether the nanocomposites have an intercalated structure. From TEM images as shown in Figure 4.33, ABS/OMT/AMMO-g-RHS and ABS/OMT/AMMO-g-CCS seem to be intercalated structure. When the silicate layer of OMT was considered, it was also found that the interlayer between silicate layers of OMT was increased. Thus, it can be concluded that their structure was partially exfoliated and intercalated structure. This result had an influence on flammability and mechanical performance as will be discussed shortly.

Figure 4.34 showed the dispersibility of OMT, grafted silica, and silatrane in ABS/OMT/AMMO-g-silica/silatrane nanocompates. It was found that OMT, grafted silica, and silatrane were dispersed thoroughly in SAN matrix. Furthermore, the interlayer between silicate layers of OMT was separated apparently. This result indicated ABS/OMT/AMMO-g-SiO_2/SSilatrane, ABS/OMT/AMMO-g-RHS/RHSilatrane, and ABS/OMT/AMMO-g-CCS/CCSilatrane were exfoliated structure in accordance with the XRD patterns shown in Figure 4.28.

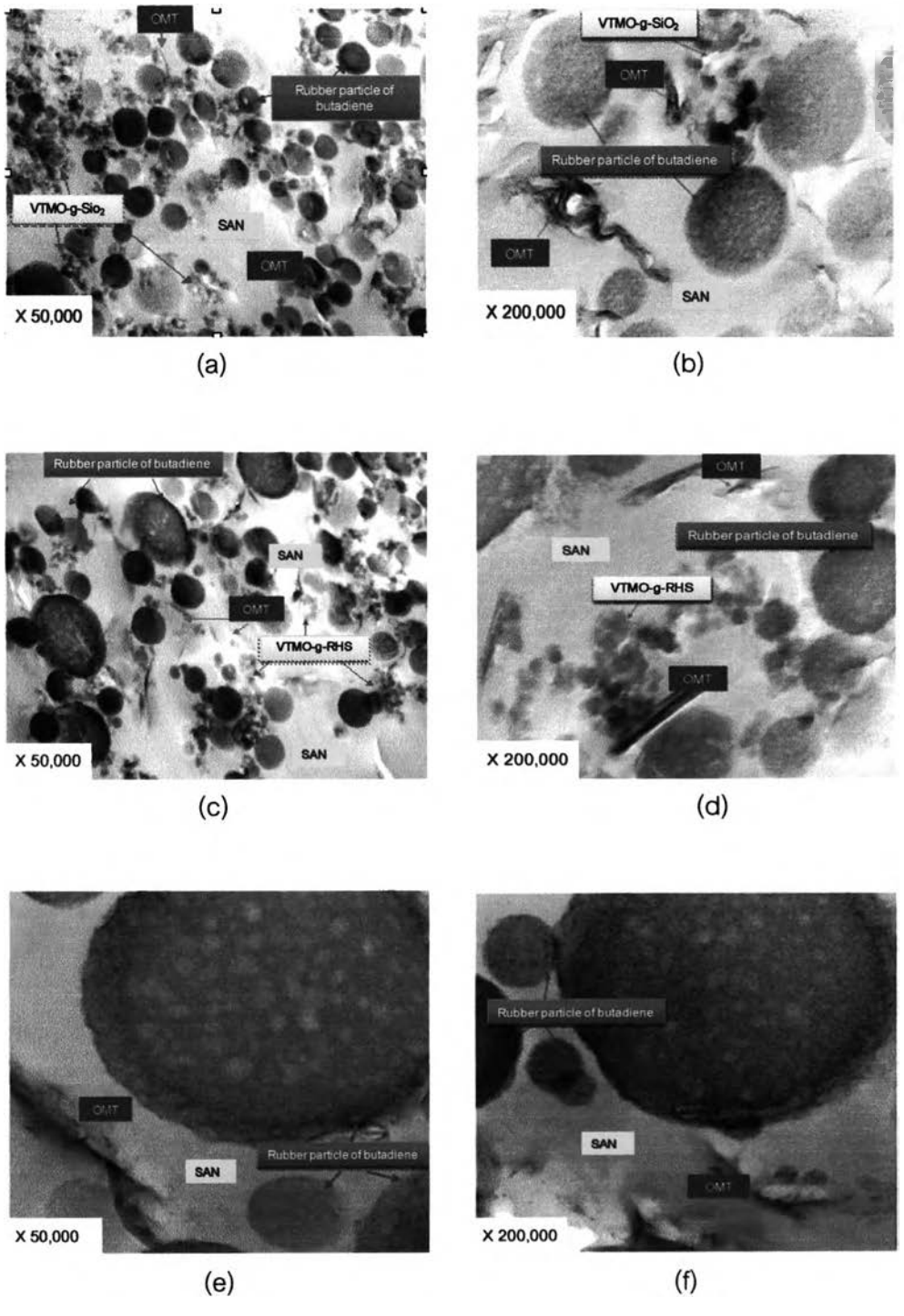

Figure 4.32 TEM images stained with OsO_4 of (a,b) ABS/OMT/VTMO-g-SiO_2, (c,d) ABS/OMT/VTMO-g-RHS, and (e,f) ABS/OMT nanocomposites at lower magnification (x50,000) and higher magnification (x200,000)

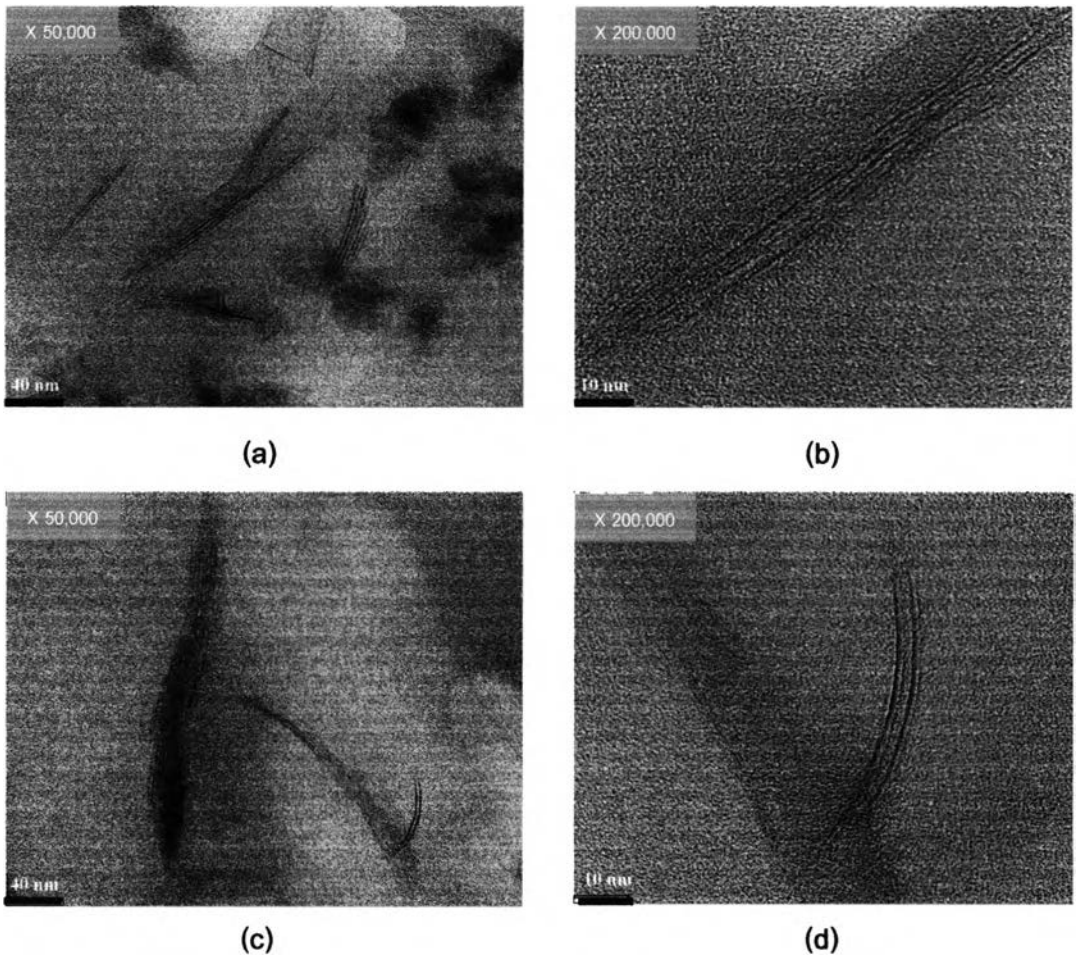

Figure 4.33 TEM images (without staining with OsO_4) of (a,b) ABS/OMT/AMMO-g-RHS and (c,d) ABS/OMT/AMMO-g-CCS nanocomposites at lower magnification (x50,000) and higher magnification (x200,000), respectively

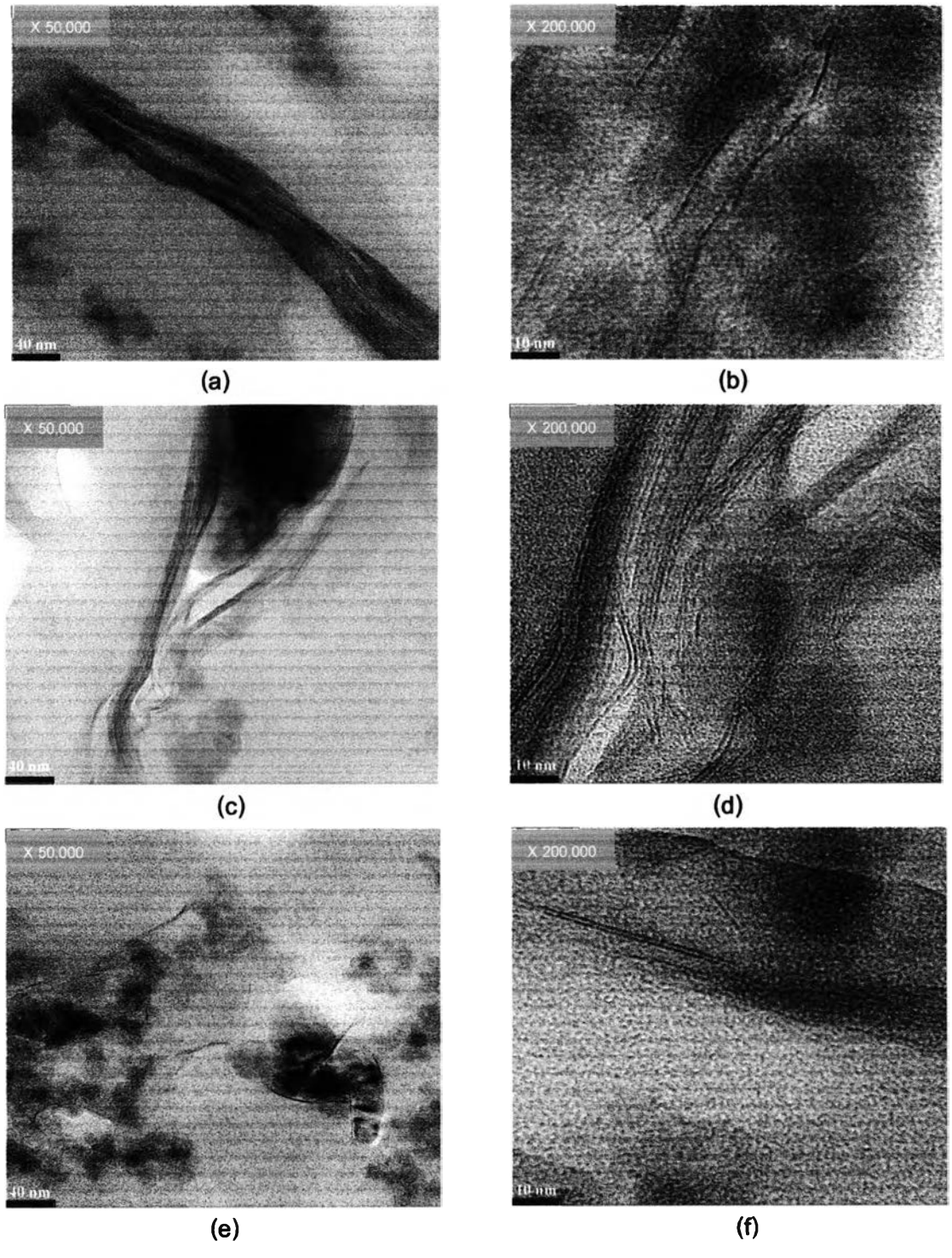

Figure 4.34 TEM images (without staining with OsO4) of (a,b) ABS/OMT/AMMO-g-SiO_2/SSilatrane, (c,d) ABS/OMT/AMMO-g-RHS/RHSilatrane, and (e,f) ABS/OMT/AMMO-g-CCS/CCSilatrane nanocomposites at lower magnitication (x50,000) and higher magnification (x200,000), respectively

4.4.4 Thermal Stability

Thermogravimetric analysis (TGA) was performed by using a TA instrument in order to evaluate the degradation temperature as well as the chemical decomposition of filler. The degradation temperature (Td) of ABS nanocomposites was shown in Figure 4.35. It was found that TGA curves of SSilatrane, RHSilatrane, and CCSilatrane were obtained in a similar way. When the amount of silicon increased, the onset of decomposition temperature was shifted to higher temperature. This behavior was in accordance to mechanism of fire performance via silicon modification and silicon containing in various type of silatrane. It can be obviously seen that the decomposition of AMMO and silatrane formed a silicon residue after the initial weight loss, which acted as a thermal insulator preventing gas evolution and slowing down the decomposition of ABS. The higher residues at 800^{o}C for ABS / 5%OMT / 20%AMMO-g-SiO_2 / 10%SSilatrane, ABS / 5%OMT / 20%AMMO-g-RHS/ 10%RHSilatrane, and ABS / 5%OMT / 20%AMMO-g-CCS / 10%CCSilatrane indicated that the formation of silicaceous char layer had an important role in flame retardancy [39-40]. Clearly, ABS/OMT nanocomposites containing AMMO-g-silica and silatrane had the highest percentage of weight residue; whereas neat ABS had the lowest amount of residue. In fact, Neat Pure was completely degraded at 470 ^{o}C. Upon adding OMT, AMMO-g-silica, and silatrane into the ABS, its percentage of weight of silicon residues at 800^{o}C was significantly increased confirming the increase in thermal stability and flame retardancy of the ABS.

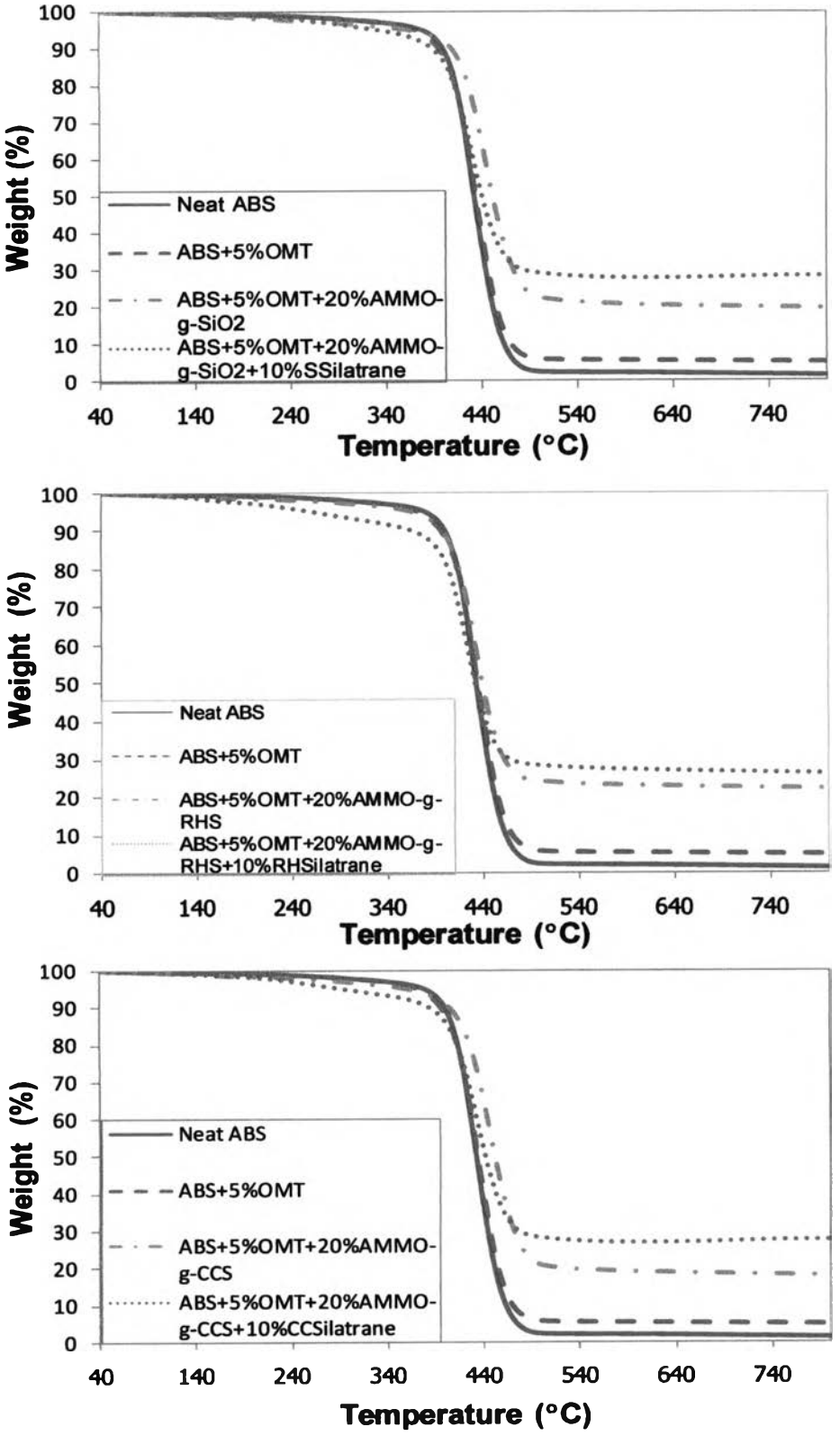

Figure 4.35 TGA graphs of (top) ABS/OMT/AMMO-g-SiO2/SSilatrane, (middle) ABS/OMT/AMMO-g-RHS/RHSilatrane, and (bottom) ABS/OMT/AMMO-g-CCS/SSilatrane

4.4.4.2 Differential Scanning Calorimetry (DSC)

Differential scanning calorimetry (DSC) was used for measuring the difference in heat flows between a sample and a reference pan that are exposed to the same temperature program. Thermal transition temperatures (e.g., glass transition temperature (Tg), and melting temperature (Tm) were determined from the second heating of DSC thermogram.

The influence of modified silica loading on thermal transition of ABS nanocomposites was studied. The second heating DSC thermograms of ABS nanocomposites were displayed in Figure 4.36 neat ABS showed glass transition temperature at approximately 106-107^{o}C but had no melting temperature which was expected to occur at 105 ^{o}C. Due to the melting peak could not be observed because there was overlapping transitions between its melting temperature and glass transition temperature [41].

Regarding DSC thermograms, it was shown that the aminosilane loading had an effect on glass transition temperature. It was found that at low amount of aminosilane, Tg was decreased as compared to neat ABS. The addition of OMT and modified silica at low amount level led to a slight decrease in the glass transition temperature because the filler couldn't be dispersed thoroughly into SAN matrix, thus the chain mobility could move easily. This caused to the decrease in Tg. On the other hand, the increasing of filler, the increasing of Tg as shown in Tg of ABS/5%OMT/20%AMMO-g-RHS and ABS/5%OMT/20%AMMO-g-CCS nanocomposites with approxinately 5^{o}C increments, comparing with that of neat ABS. This result was because of rigidity of silicon containing in silicate layer of OMT and silane modified silica particles. In addition, agglomeration of silica had an influence on the increase of Tg because it could decrease chain mobility of ABS. Furthermore, ABS with 20 wt% of AMMO-g-RHS loading gave the maximum shift of glass transition temperature, thus it was expected to obtain good mechanical performance (i.e., tensile strength and modulus) as well.

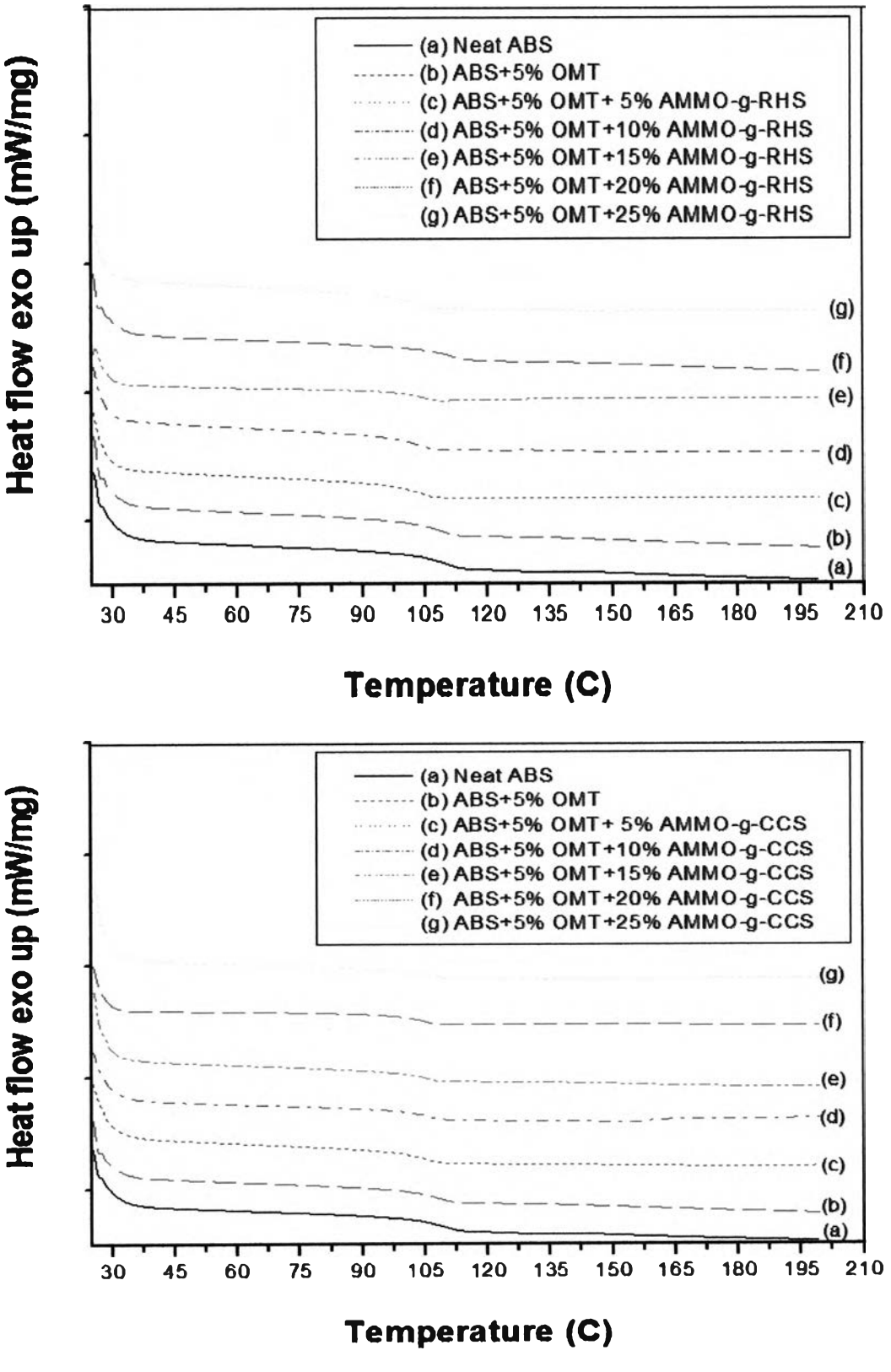

Figure 4.36 DSC thermograms of (top) ABS/OMT/AMMO-g-RHS (top) and(bottom) ABS/OMT/AMMO-g-CCS

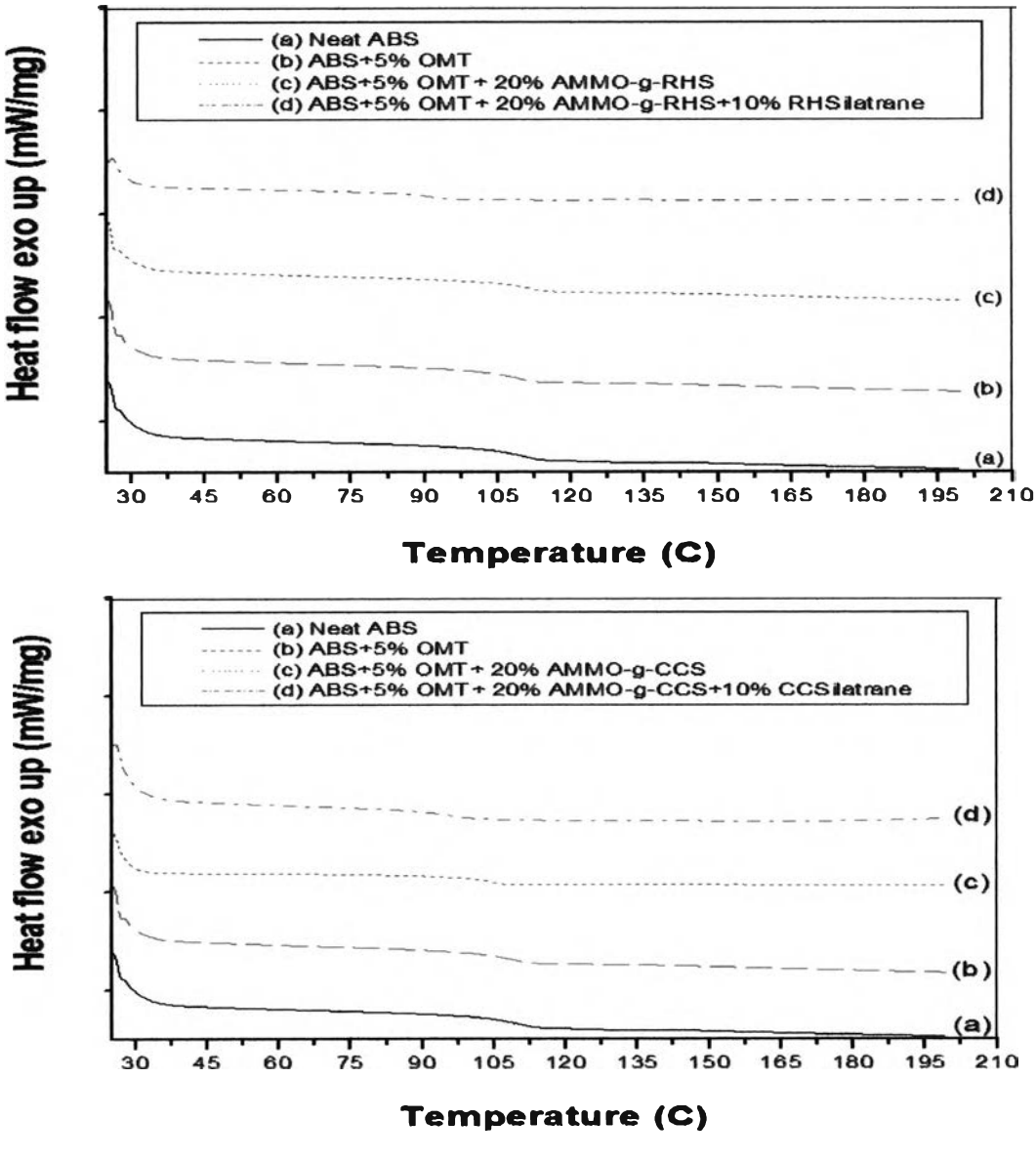

Figure 4.37 DSC thermograms of ABS/OMT/AMMO-g-RHS/RHSilatrane (top) and ABS/OMT/AMMO-g-CCS/CCSilatrane (bottom)

The effect of silatrane on thermal stability was shown in Figure 4.37 and Table 4.7. DSC thermograms showed that ABS/OMT/AMMO-g-RHS/RHSilatrane and ABS/OMT/AMMO-g-CCS/CCSilatrane gave the maximum shift of glass transition temperature towards lower temperature, thus these two nanocomposites were expected to yield good mechanical performance due to flexibility of ethylene glycol part in

silatrane structure. Similar to ABS/OMT nanocomposites containing AMMO-g-silica, this result was because of rigidity of silicon containing in silicate layer of OMT, silane modified, and silatrane. In addition, agglomeration of silica had an impact on the increase of Tg because it could obstruct and decrease chain mobility of ABS.

Table 4.9 TGA and DSC data of ABS nanocomposites

Samples	Td (°C) (Onset)	% Weight residue at 750 °C	Tg (°C)
Neat ABS	407.14	1.42	107.73
ABS+5%OMT	406.95	4.95	106.68
ABS+5%OMT+20%AMMO-g-CCS	408.71	20.75	101.79
ABS+5%OMT+20%AMMO-g-CCS+10%CCSilatrane	403.38	27.67	98.36
ABS+5%OMT+20%AMMO-g-RHS	408.83	22.33	110.76
ABS+5%OMT+20%AMMO-g-RH+10%RHSilatrane	404.13	26.34	91.09

4.4.5 Flammability Properties of ABS composites

UL-94 and LOI tests were used to examine flammability of ABS. UL-94 test was measured the ignition of ABS, reported as rate of burning. Regarding UL-94 HB test, the burning rate of samples must not exceed 40 mm/min. Limiting oxygen index (LOI) measured the ease of extinction of fire. The samples were measured the minimum oxygen concentration that was required for sustaining flame within 180 seconds or 5 cm of length.

4.4.5.1 Effect of OMT Loading

Organomontmorillonite (OMT) was used as nano-filler for improvement of flame retardant properties of ABS. Figure 4.38 and Table 4.10 showed that the decrease of combustion time in UL-94 HB test of ABS/OMT nanocomposites was in agreement with the increase of the limiting oxygen index (LOI) value. As shown in Table 4.10 the burning rate of ABS with 5 wt% of OMT gave the minimum value of 28.84 mm/min. On the other hand, the LOI value of ABS with 5 wt% of OMT showed the maximum value at 18.2%. Then, as compared to the burning rate of neat ABS, ABS/5%OMT could improve flame retardant behavior up to 53.86%. The increasing of OMT loading caused a decrease of burning rate and increase of LOI values because OMT could form char layer which acted as an insulator and a mass transport barrier, slowing the escape of the volatile product (e.g., HCN) generated during thermal decomposition of ABS [14]. However, of the burning rate of ABS with 7 and 9 wt% of OMT, increased apparently because of the higher amount of OMT. The organic chains of dioctadecyl dimethyl ammonium chloride used as modifing agent in OMT could accelerate the combustion rate instead of inhibition while burning. Therefore, the addition of 5 wt% of OMT was chosen for studying flame retardant properties of ABS as discussed in the next topic.

Table 4.10 UL-94 and LOI test of ABS/OMT nanocomposites

Samples	Burning rate of UL-94 HB Grade (mm/min)	LOI (%)
Neat ABS	62.50	17.3
ABS+1%OMT	36.79	17.7
ABS+3%OMT	31.44	18.1
ABS+5%OMT	28.84	18.2
ABS+7%OMT	31.91	18.0
ABS+9%OMT	33.20	17.9

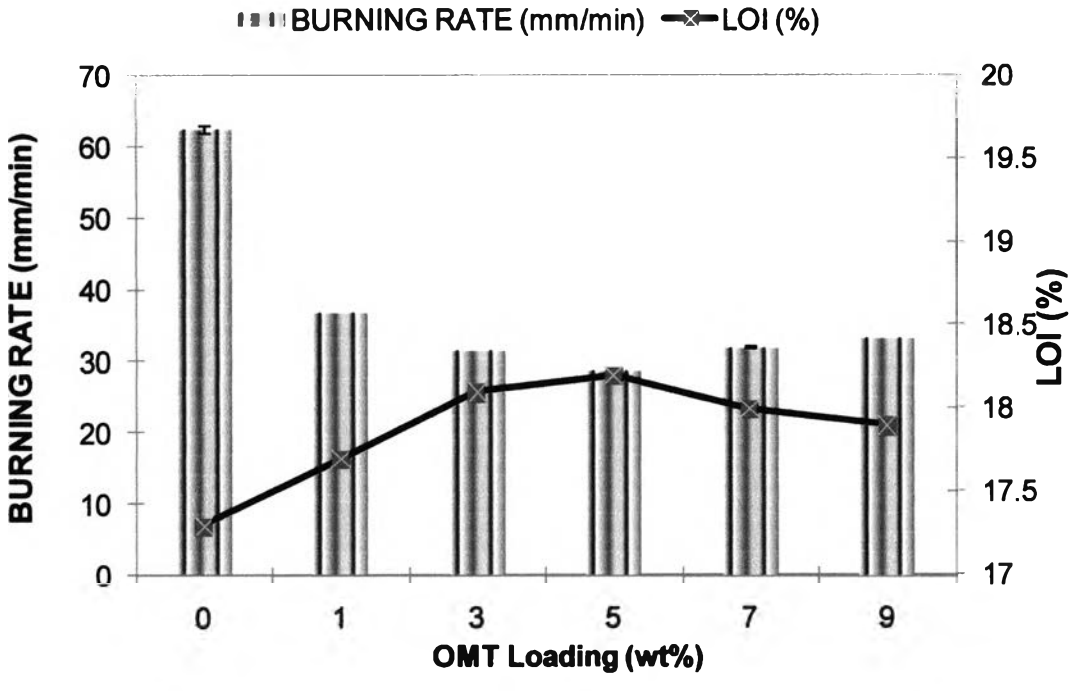

Figure 4.38 Effect of OMT loading on flammability of ABS nanocomposites

4.4.5.2 Effect of Silane Coupling Types and Contents

Evaluation of flammability properties of ABS nanocomposites was measured and the results were shown in Figure 4.39 and Table 4.11. The influence of silane coupling types and contents on the burning rate and LOI value of ABS nanocomposites was studied. In this work, vinyltrimethoxysilane (VTMO) and 3-aminopropyltrimethoxy silane (AMMO) were used as silane coupling agent for modifying surface of silica and 5 wt% of OMT was chosen for blending with ABS and silane coupling as mentioned above. The results revealed that the higher AMMO-g-silica loading, the higher LOI values and the lower burning rate. The lower burning rate determined by UL-94 test and greater LOI value of all ABS/OMT/AMMO-g-SiO_2, ABS/OMT/AMMO-g-RHS, and ABS/OMT/AMMO-g-CCS nanocomposites revealed that these nanocomposites showed better flame retardant properties than those of Neat ABS, ABS/OMT nanocomposites, and ABS/AMMO microcomposites.

Table 4.11 UL-94 and LOI test of ABS/OMT/AMMO-g-silica nanocomposites

Samples	Burning rate of UL-94 HB Grade (mm/min)	LOI (%)
Neat ABS	62.50	17.3
ABS+5%AMMO	32.71	18.1
ABS+5%OMT	28.84	18.2
ABS+5%OMT+5%Ungrafted SiO_2	29.00	18.1
ABS+5%OMT+5%Ungrafted RHS	29.80	18.0
ABS+5%OMT+5%Ungrafted CCS	30.41	17.8
ABS+5%OMT+5%AMMO-g-SiO_2	28.52	18.7
ABS+5%OMT+10%AMMO-g-SiO_2	23.69	18.8
ABS+5%OMT+15%AMMO-g-SiO_2	21.35	18.9
ABS+5%OMT+20%AMMO-g-SiO_2	19.35	19.3
ABS+5%OMT+25%AMMO-g-SiO_2	18.58	19.7
ABS+5%OMT+5%AMMO-g-RHS	27.71	18.4
ABS+5%OMT+10%AMMO-g-RHS	26.93	18.5
ABS+5%OMT+15%AMMO-g-RHS	23.43	18.8
ABS+5%OMT+20%AMMO-g-RHS	21.18	19.2
ABS+5%OMT+25%AMMO-g-RHS	20.95	19.4
ABS+5%OMT+5%AMMO-g-CCS	24.41	18.4
ABS+5%OMT+10%AMMO-g-CCS	24.35	18.5
ABS+5%OMT+15%AMMO-g-CCS	22.75	18.6
ABS+5%OMT+20%AMMO-g-CCS	21.14	18.8
ABS+5%OMT+25%AMMO-g-CCS	23.81	18.9

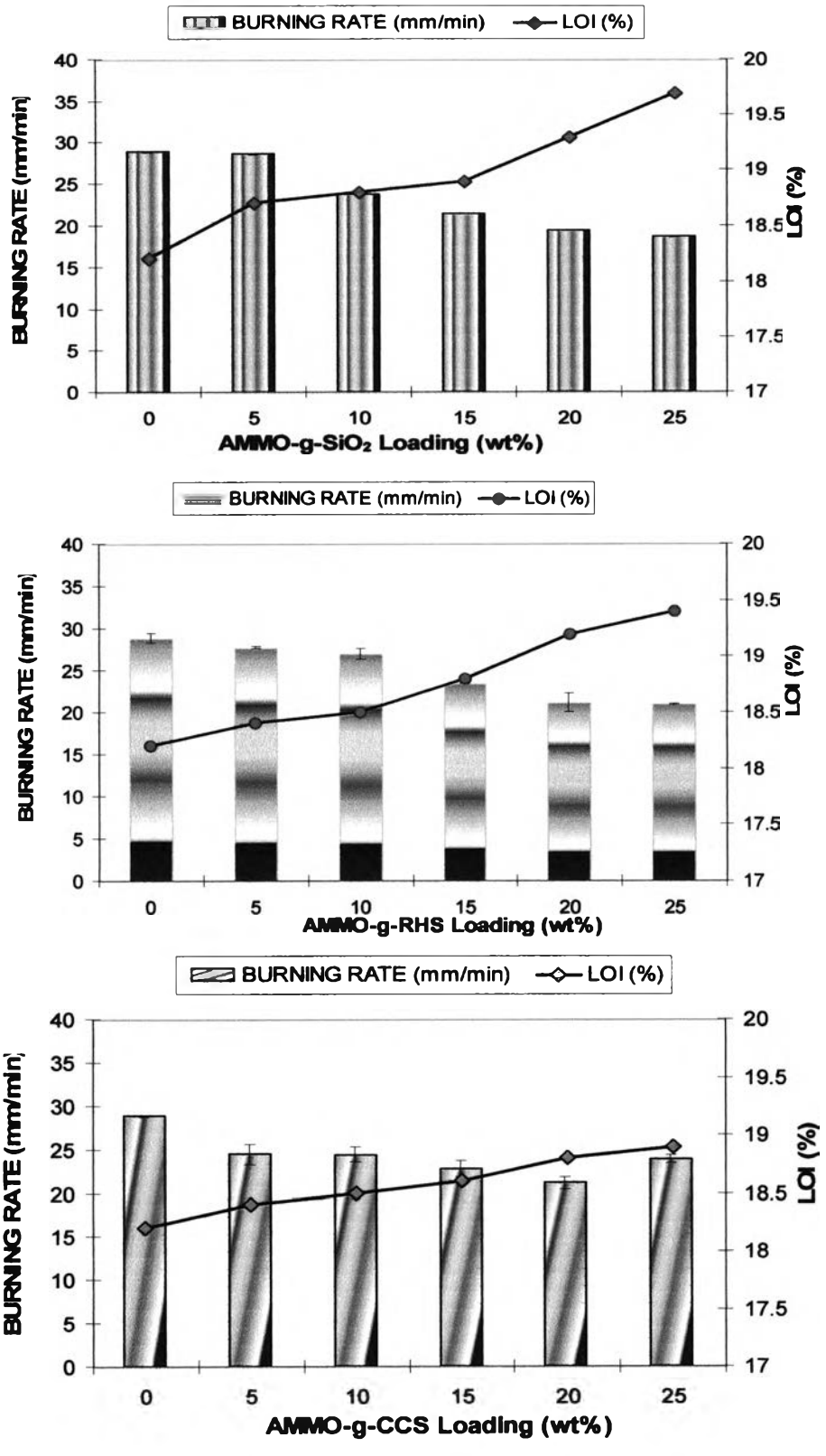

Figure 4.39 Effect of AMMO-g-silica loading on flammability of ABS/OMT nanocomposites

ABS/5%OMT/20%AMMO-g-SiO_2, ABS/5%OMT/20%AMMO-g-RHS, and ABS/5%OMT/20%AMMO-g-CCS could decrease the burning rate up to 69.04%, 66.11%, and 66.18%, respectively when compared to neat ABS. Particulary, when comparing with ABS/OMT/ungrafted silica nanocomposites , all ABS/OMT/AMMO-g-silica had better flame retardant properties. This was because OMT and AMMO grafted on silica could form a surface layer of protective char during combustion of the nanocomposites. Obviously, the increasing amount of AMMO grafted on silica from 5% to 25% could increase the LOI value and decrease the burning rate of the ABS nanocomposites significantly. Additionally, it was also found that the efficiency of flame retardant of AMMO grafted on RHS and CCS was similar to that of commercial silica modestly.

Vinyltrimethoxysilane (VTMO) was another type of silane coupling agent used in this research to study the effect of amount of VTMO grafted on silica on flammability of ABS. From Table 4.12 and Figure 4.40, ABS/5%OMT/25%VTMO-g-SiO_2 and ABS/5%OMT/20%VTMO-g-RHS showed the best formulation for improving flame retardant properties of ABS because they exhibited the highest LOI value and lowest burning rate. In addition, it was also noticed that the burning rate of ABS/5%OMT/25%VTMO-g-RHS increased and LOI value decreased when compared with ABS/5%OMT/20%VTMO-g-RHS. This result might be from agglomeration of silica particles at high loading that had an influence on dispersion into SAN matrix.

Comparing with their ungrafted counterparts, ABS/OMT/VTMO-g-silica nanocomposites showed better LOI values and lower burning rate. For example, ABS/5%OMT/VTMO-g-RHS had higher LOI value and lower burning rate than that of ABS/5%OMT/5%Ungrafted RHS. As calculated the percentage of burning rate increase, ABS/5%OMT/VTMO-g-RHS gave the percentage of burning rate and LOI value up to 29.56% and 7.78%, respectively. This shown that silane grafted on silica could enhance flame retardant properties of ABS undoubtedly.

Table 4.12 UL-94 and LOI test of ABS/OMT/VTMO-g-silica nanocomposites

Samples	Burning rate of UL-94 HB Grade (mm/min)	LOI (%)
Neat ABS	62.50	17.3
ABS+5%OMT	28.84	18.2
ABS+5%VTMO	36.72	17.5
ABS+5%OMT+5%Ungrafted SiO_2	29.00	18.1
ABS+5%OMT+5%Ungrafted RHS	29.80	18.0
ABS+5%OMT+5%Ungrafted CCS	30.41	17.8
ABS+5%OMT+5%VTMO-g-SiO_2	27.95	18.2
ABS+5%OMT+10%VTMO-g- SiO_2	30.45	18.5
ABS+5%OMT+15%VTMO-g- SiO_2	29.56	18.9
ABS+5%OMT+20%VTMO-g- SiO_2	22.85	19.4
ABS+5%OMT+25%VTMO-g- SiO_2	20.59	19.3
ABS+5%OMT+5%VTMO-g-RHS	27.90	18.3
ABS+5%OMT+10%VTMO-g-RHS	26.71	18.6
ABS+5%OMT+15%VTMO-g-RHS	23.58	18.9
ABS+5%OMT+20%VTMO-g-RHS	20.99	19.4
ABS+5%OMT+25%VTMO-g-RHS	30.70	19.3

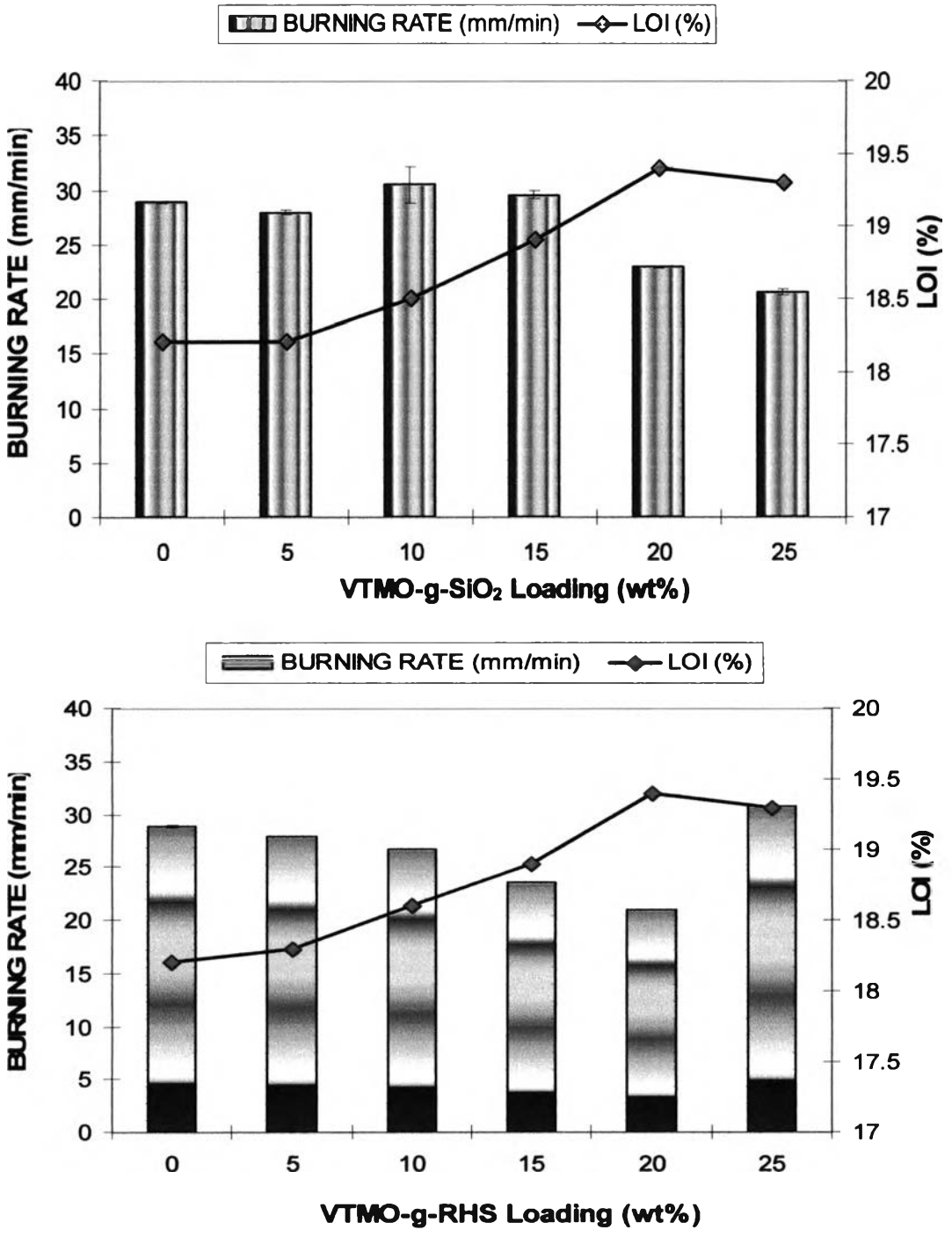

Figure 4.40 Effect of VTMO-g-silica loading on flammability of ABS/OMT nanocomposites

Comparing between two types of silane coupling agent used in this work, Figure 4.41, shown that aminosilane used as surface-modifying agent gave better flame retardancy (i.e., lower burning rate and greater LOI values) than that of vinysilane significantly. This was owing to amino group in AMMO. Therefore, AMMO was chosen to

study the effect of type and content of silatrane as described in the next topic.

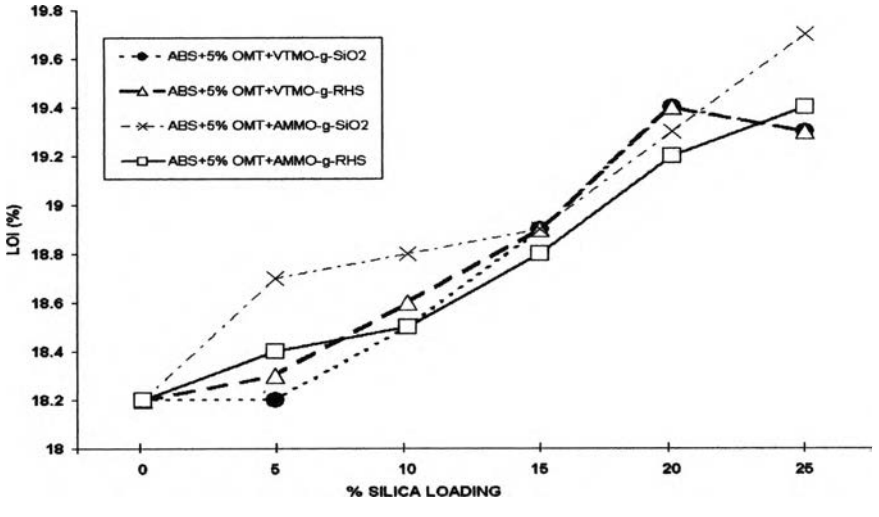

(a)

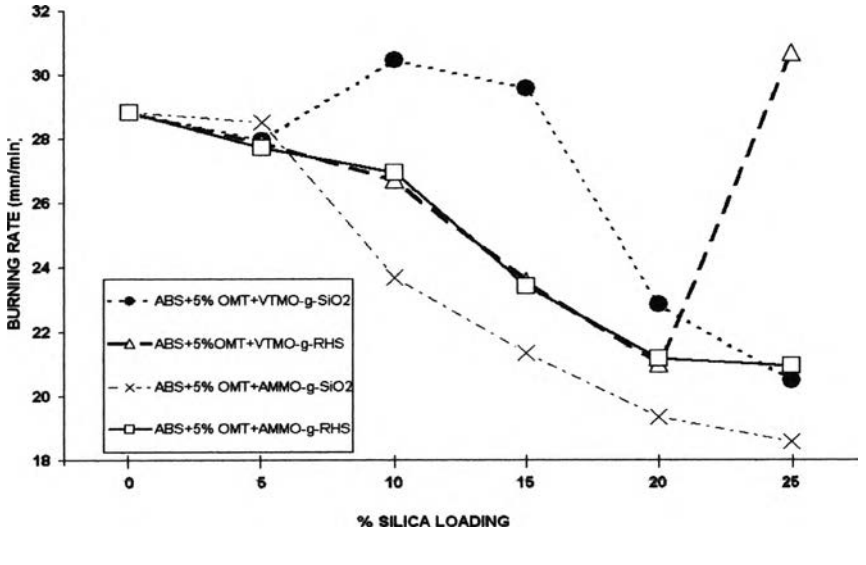

(b)

Figure 4.41 Flammability test of (a) ABS/OMT/AMMO-g-SiO_2 and (b) ABS/OMT/VTMO-g-SiO_2 ABS/OMT/AMMO-g-RHS and ABS/OMT/VTMO-g-RHS

4.4.5.3 Effect of Silatrane Type and Contents

Flame retardant nanocomposites were evaluated by testing methods using horizontal burning test (UL-94) and limiting oxygen index (LOI). The best results should have high LOI value and low burning rate value. As a result of UL-94 HB test, it was shown that the burning rate of ABS/5%OMT/20%AMMO-g-SiO_2/10%SSilatrane, ABS/5%OMT/20%AMMO-g-RHS/10%RHSilatrane, and ABS/5%OMT/20%AMMO-g-CCS/10%CCSilatrane decreased approximately 73.22%, 66.18%, and 70.64%,

respectively when compared to that of neat ABS. From Figure 4.42 and Table 4.13, it was found that the addition of OMT and silatrane into ABS could decrease the burning rate up to 17% and increased the LOI value up to 5%, whereas ABS with 5 wt% of silatrane could decrease the burning rate only 8%. This was because of the synergistic effect between OMT and silatrane. When silatrane was blended with ABS, OMT, and AMMO grafted on silica, it revealed that the increase of silatrane loading could decrease the burning rate and increase the LOI value of ABS nanocomposites. This resulted from silicaceous char layer acted as a good insulator during combustion. Hence, silatrane could be an effective flame retardant additive for ABS.

Table 4.13 UL-94 and LOI test of ABS/OMT/AMMO-silica/silatrane nanocomposites

Samples	Burning rate of UL-94 HB Grade (mm/min)	LOI (%)
Neat ABS	62.50	17.3
ABS+5%OMT	33.20	17.9
ABS+5%SSilatrane	33.84	17.6
ABS+5%OMT+5%SSilatrane	30.52	18.2
ABS+5%OMT+20%AMMO-g-SiO_2+0%SSilatrane	19.35	19.3
ABS+5%OMT+20%AMMO-g-SiO_2+5%SSilatrane	27.87	19.0
ABS+5%OMT+20%AMMO-g-SiO_2+10%SSilatrane	16.74	19.2
ABS+5%OMT+20%AMMO-g-SiO2+0%RHSilatrane	21.18	19.2
ABS+5%OMT+20%AMMO-g-RHS+5%RHSilatrane	27.73	19.6
ABS+5%OMT+20%AMMO-g-RHS+10%RHSilatrane	21.14	19.7
ABS+5%OMT+20%AMMO-g-CCS+0%CCSilatrane	21.14	18.8
ABS+5%OMT+20%AMMO-g-CCS+5%CCSilatrane	27.90	18.7
ABS+5%OMT+20%AMMO-g-CCS+10%CCSilatrane	18.35	19.6

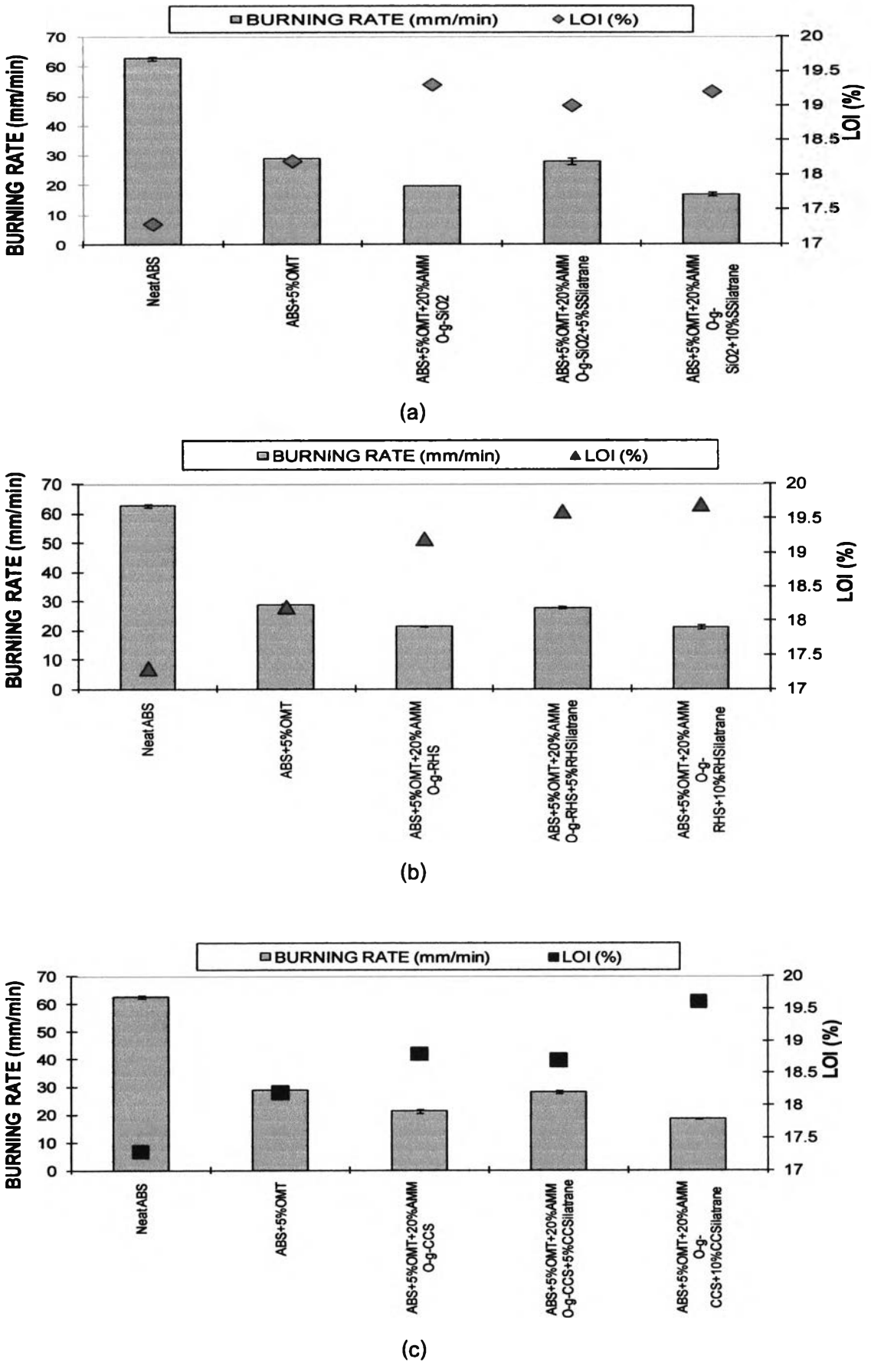

Figure 4.42 Effect of each silatrane type on flammability of ABS

Figure 4.43 showed the UL-94 horizontal burning test of ABS nanocomposites. Photographs of (a) ABS/OMT/Ungrafted SiO_2, (b) ABS/OMT/AMMO-g-SiO_2/SSilatrane, (c) ABS/OMT/AMMO-g-RHS/RHS/Silatrane, and (d) ABS/OMT/AMMO-g-CCS/CCSilatrane nanocomposites were illustrated that the distance of ignition of (b) ABS/OMT/AMMO-g-SiO_2/SSilatrane, (c) ABS/OMT/AMMO-g-RHS/RHS/Silatrane, and (d) ABS/OMT/AMMO-g-CCS/CCSilatrane nanocomposites was less than that of ABS/OMT/Ungrafted SiO_2. This led to the lower burning rate of ABS/OMT/AMMO-g-silica/silatrane.

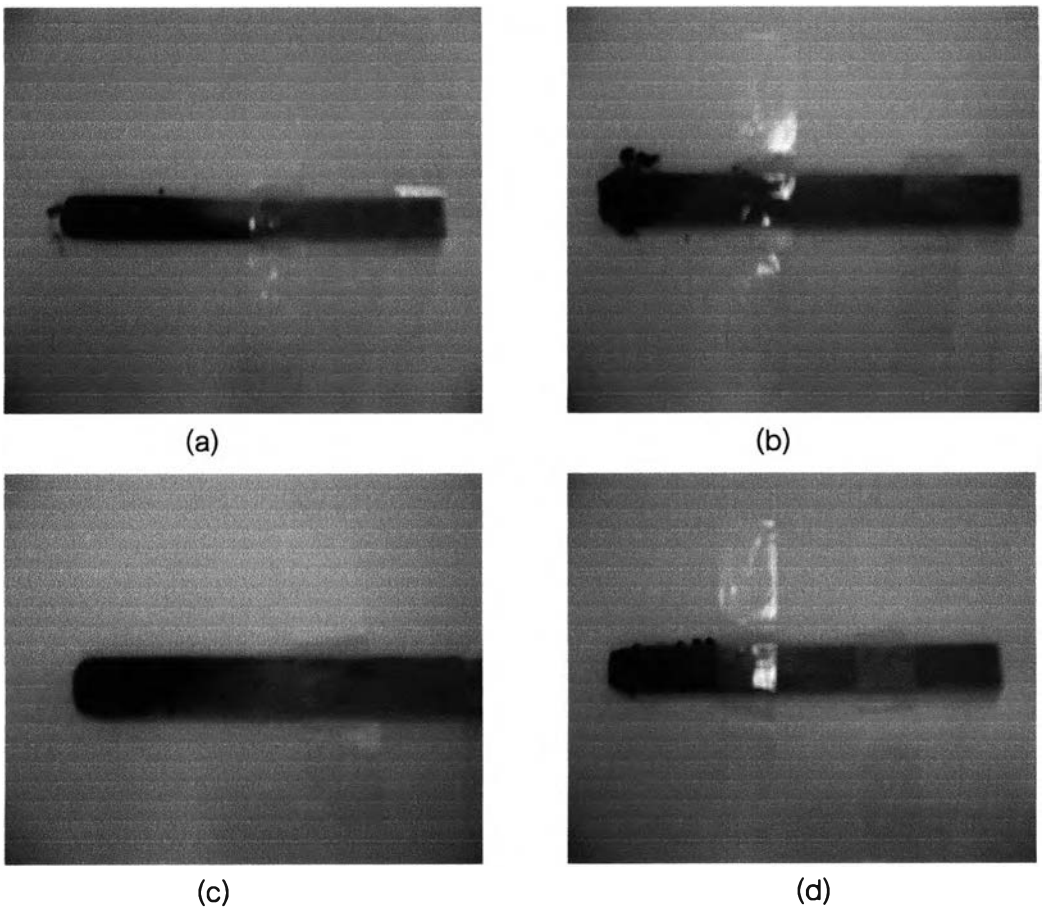

Figure 4.43 Photographs of UL-94 HB burning test of (a) ABS/OMT/Ungrafted SiO_2, (b) ABS/OMT/AMMO-g-SiO_2/SSilatrane, (c) ABS/OMT/AMMO-g-RHS/RHS/Silatrane, and (d) ABS/OMT/AMMO-g-CCS/CCSilatrane nanocomposites

As a result of UL-94 HB test, it was found that the burning rate of ABS/5%OMT/20%AMMO-g-SiO_2/10%SSilatrane, ABS/5%OMT/20%AMMO-g-RHS /10%RHSilatrane, and ABS/5%OMT/20%AMMO-g-CCS/10%CCSilatrane decreased approximately 73.22%, 66.18%, and 70.64%, respectively and the LOI value increased around 10.98%, 13.87% and 13.29%, respectively when compared to that of neat ABS. As the work of Ma et al [29], they synthesized poly(diaminodiphenyl methane spirocyclic pentaerythritol bisphosphonate) as flame retardant additive for ABS. It revealed that it could improve the LOI value up to 49.74%. However, the synthesized silatrane is low cost and easy to synthesize when compared to the work of Ma et al. In further study, we should increase the amount of silatrane and control the purity of silica to obtain the efficient flame retardant additives.

4.4.6 Mechanical Properties

4.4.6.1 Impact Strength

4.4.6.1.1 Effect of Silane Coupling Types and Contents

The notched Izod impact test was measured according to ASTM D256. The result as shown in Figure 4.44 and 4.45 and Table 4.14 revealed that the impact strength values of all ABS nanocomposites decreased obviously when the amount of silica and modified silica (i.e., AMMO-g-silica and VTMO-g-silica) increased. This result was because of rigidity of modified silica and OMT leading to the brittle behavior of ABS nanocomposites [42-43].

In comparison to impact strength of ABS/OMT nanocomposites having ungrafted silica as shown in Figure 4.45, it was found that the impact strength of ABS/OMT nanocomposites containing AMMO and VTMO grafted on silica were lowered because of rigidity of modified silica. In addition, it was found that the ABS/OMT nanocomposites containing AMMO modified silica had higher impact strength values than those of VTMO because of hydrogen bonding occurred from amino functional group in AMMO. In fact, their impact strength was only slightly lowered than the ABS/OMT nanocomposites with ungrafted silica. Hence, AMMO was more suitable to use as surface-modifying agent for silica.

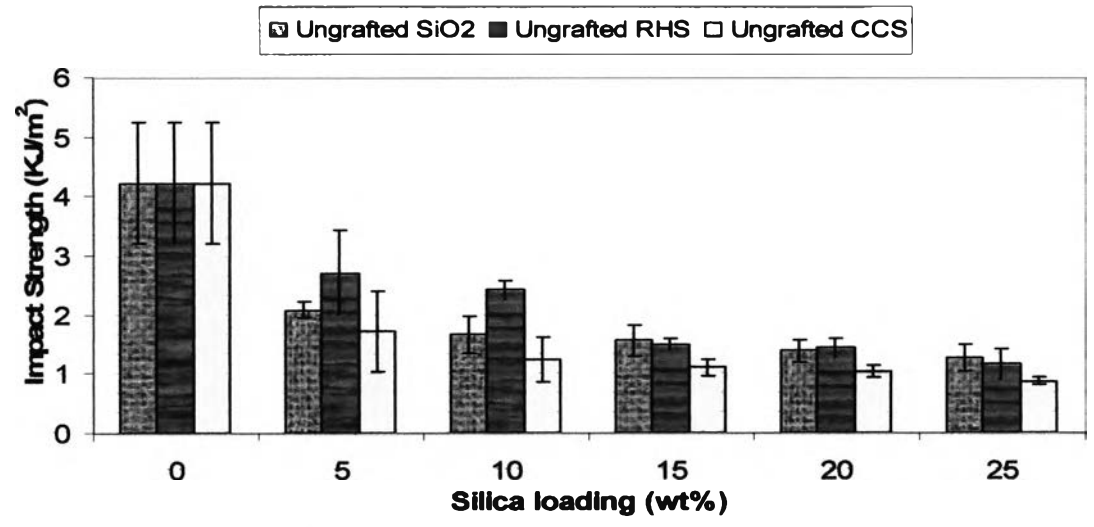

(a)

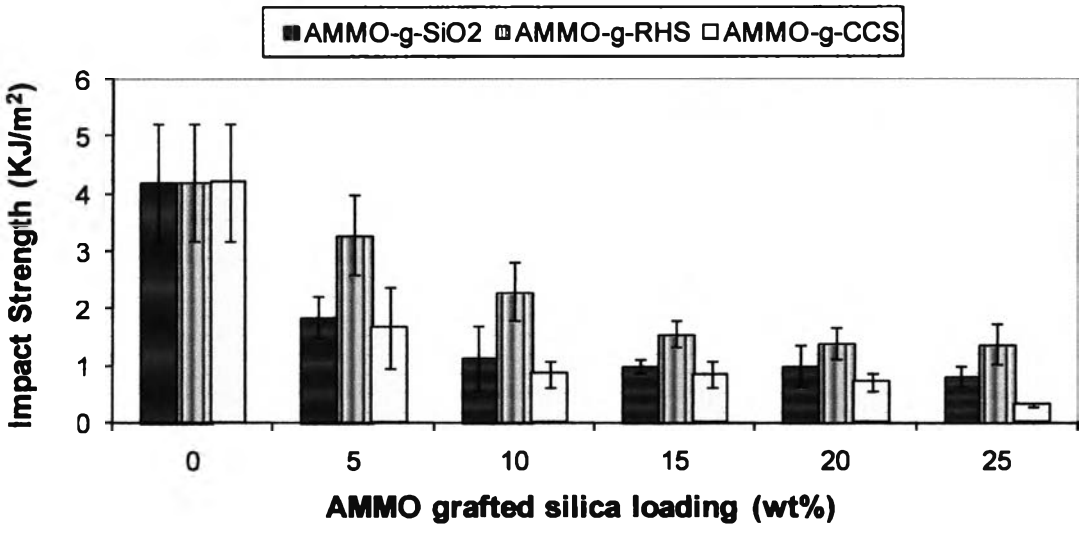

(b)

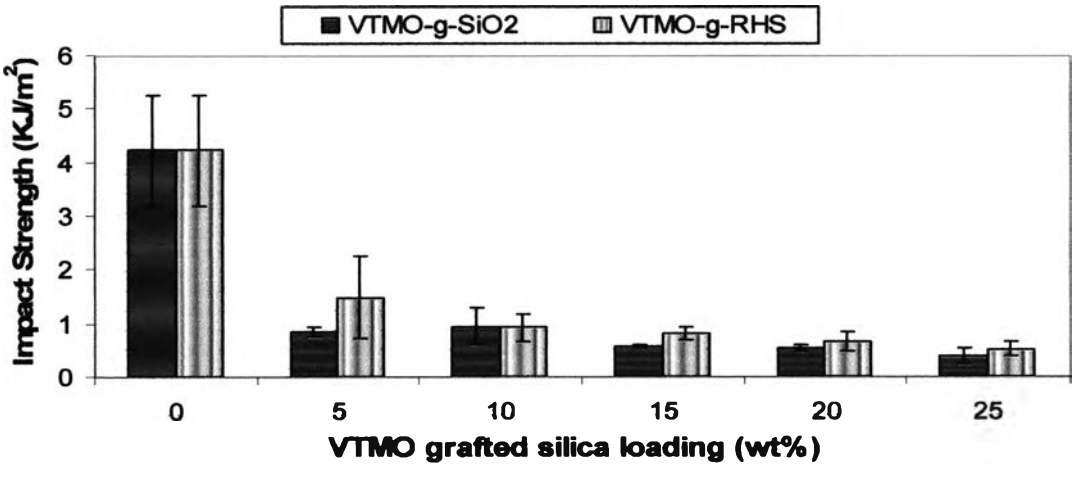

(c)

Figure 4.44 Effect of type and content of (a)ungrafted silica, (b) AMMO-g-silica, and (c) VTMO-g-silica on impact strength of ABS/5%OMT nanocomposites

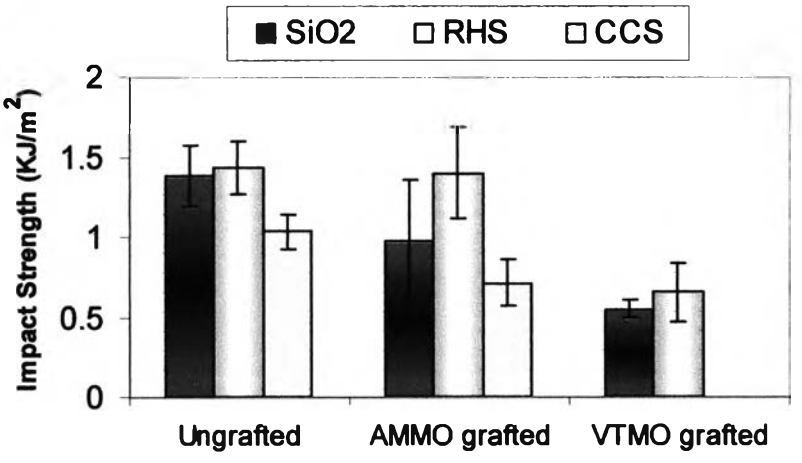

Figure 4.45 Effect of silane coupling type at 20 wt% loading on impact strength of ABS/5%OMT nanocomposites

4.4.6.1.2 Effect of Silatrane Types and Contents

Figure 4.46 showed that the silatrane loading had an effect on impact strength of ABS/OMT nanocomposites. As expected, the impact strength of ABS/OMT/AMMO-g-silica/silatrane increased with increasing of silatrane loading.

RHSilatrane showed the highest impact strength value as compared to SSilatrane and CCSilatrane. This resulted from the difference of particle size. CCSilatrane had the smallest particle size, hence CCSilatrane might be lost easily during blending with ABS nanocomposites. Furthermore, it was also noticed that some agglomeration of SSilatrane might have an influence on the decrease in impact strength value; thus RHSilatrane showed the best impact strength when compared with CCSilatrane and SSilatrane. This might be because of its chemical structure that has ethylene glycol part, which can enhance flexibility and toughness of the nanocomposites.

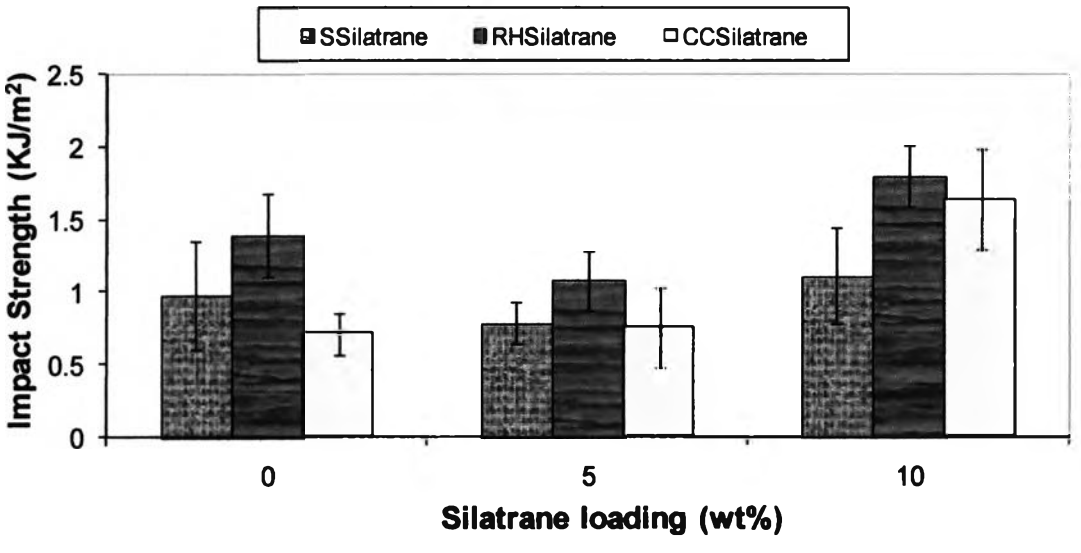

Figure 4.46 Effect of silatrane loading on impact strength of ABS/OMT/AMMO-g-silica nanocomposites

4.4.6.2 Tensile Properties

Besides impact strength, mechanical performance of ABS nanocomposites was also elucidated through tensile properties by using a universal testing machine. The gauge length was 25 mm while test speed was 50 mm/min.

4.4.6.2.1 Effect of Silane Coupling Types and Contents

ABS/OMT/AMMO-g-SiO_2, ABS/OMT/AMMO-g-RHS, and ABS/OMT/AMMO-g-CCS nanocomposites were prepared for tensile properties measurement. Figure 4.47 and 4.48 showed tensile strength value of ABS/OMT/modified silica nanocomposites. For ungrafted silica and AMMO-g-silica, it was found that the tensile strength increased upon increasing silica content. The ABS/OMT with 25 wt% of AMMO-g-SiO_2 and ABS/OMT with 25% wt of AMMO-g-RHS gave the highest tensile strength values; whereas the ABS/OMT with 5 wt% of AMMO-g-SiO_2 and ABS/OMT with 5 wt% of AMMO-g-RHS gave the lowest tensile strength values. This result suggested that 5 wt% of AMMO-g-SiO_2/AMMO-g-RHS was too low to reinforce the nanocomposites. At higher loading, however, both types of silica can bear load transmitted from ABS matrix; thus reinforcing the ABS/OMT nanocomposites.

For VTMO-g-silica, it was found that ABS with 10 wt% of VTMO-g-silica loading gave the maximum tensile strength value and then the tensile strength values decreased with increasing modified silica contents. The addition of OMT and VTMO modified silica

in high loading level caused the reduction in tensile strength because of its rigidity and agglomeration characteristics of modified silica particles [Stretz et al].

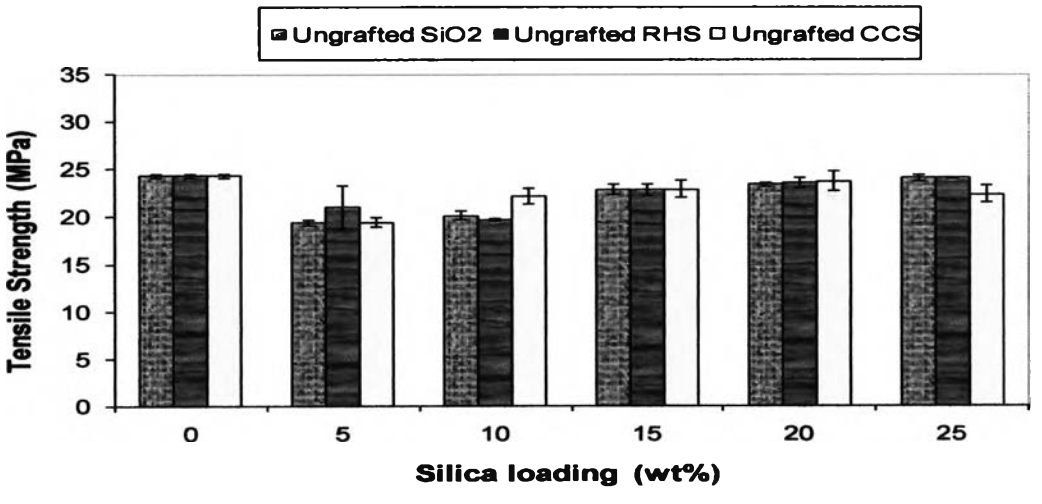

(a)

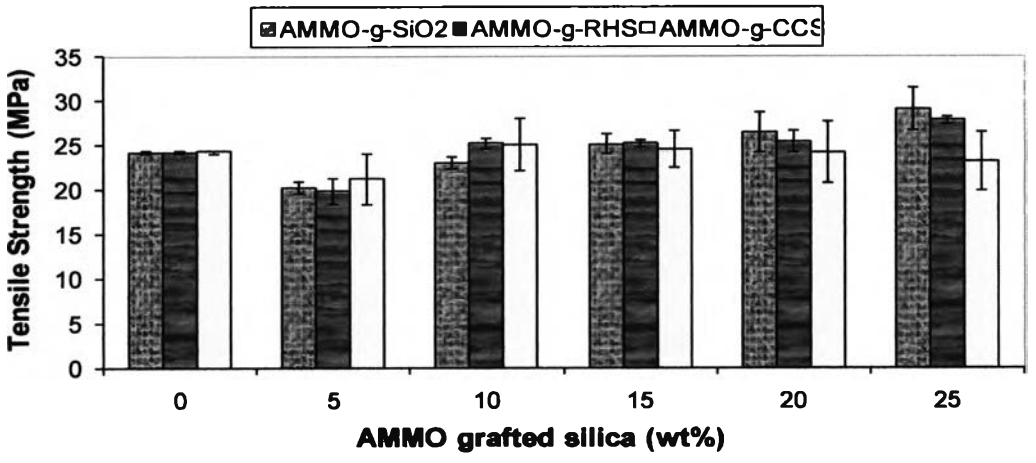

(b)

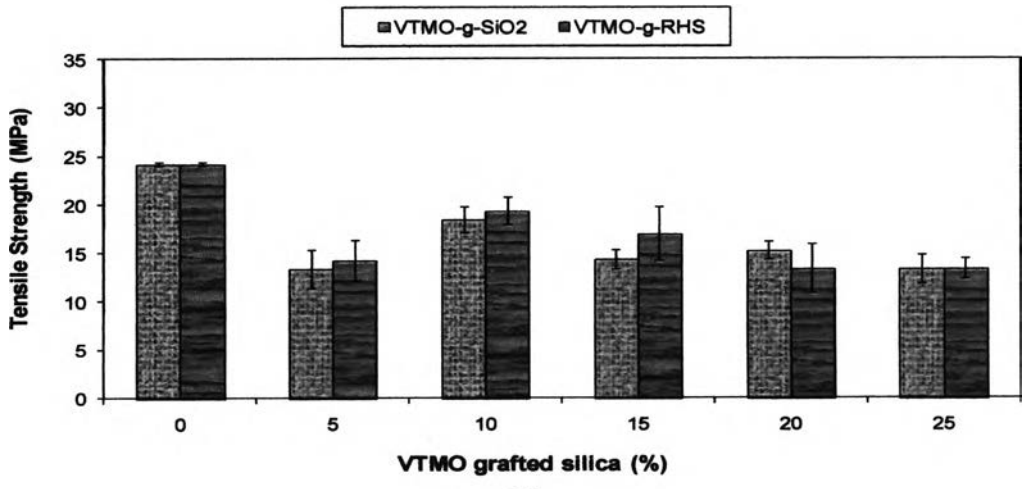

(c)

Figure 4.47 Effect of type and content of (a) ungrafted silica, (b) AMMO-g-silica, and (c) VTMO-g-silica on tensile strength of ABS/5%OMT nanocomposites

From Figure 4.48, it was obviously shown that aminosilane coupling agent had better efficiency to promote the interfacial adhesion between silica particles and ABS matrix than vinylsilane coupling agent, resulting in higher tensile strength values regardless of silica type. However, unexpectedly, VTMO had an adverse effect on the tensile strength of the ABS/OMT nanocomposites. The greater efficiency of AMMO was believed to attribute from the hydrogen bonding occurred between amino group of AMMO and nitrile group of ABS. Therefore, AMMO was the most suitable silane coupling agent for silica surface-modification.

Regarding the silica type, unlike impact strength, no significant difference among three types of silica (i.e., commercial silica, RHS, and CCS) can be noticed.

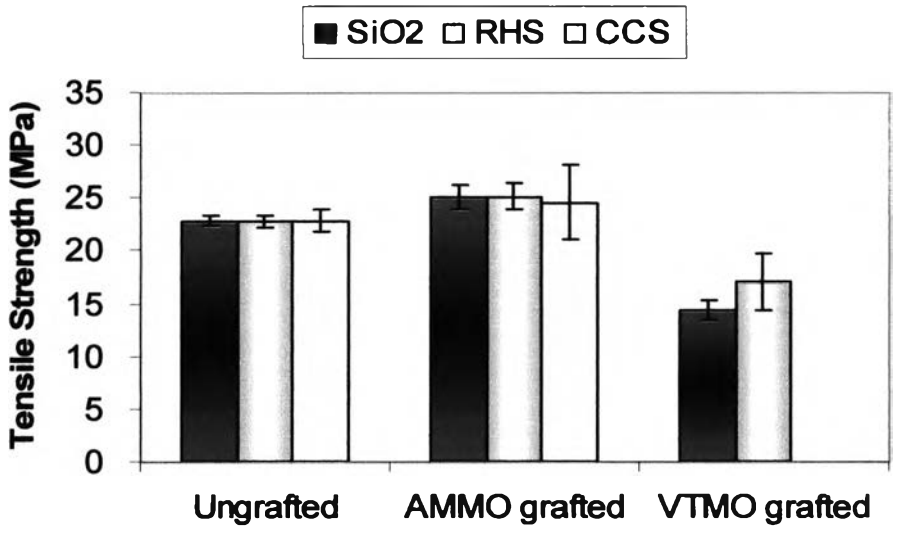

Figure 4.48 Effect of silane coupling type at 15 wt% on tensile strength of ABS/5%OMT nanocomposites

For Young's modulus, In general, the modulus increased by inorganic fillers was achieved at the expense of lowered tensile strength, due to the filler-polymer interfacial weakness [44]. From Figure 4.49, the data revealed that Young's modulus was increased with increasing of ungrafted and modified silica contents due to the rigidity of fillers. The maximum Young's modulus values were obtained at 25 wt% of filler loading.

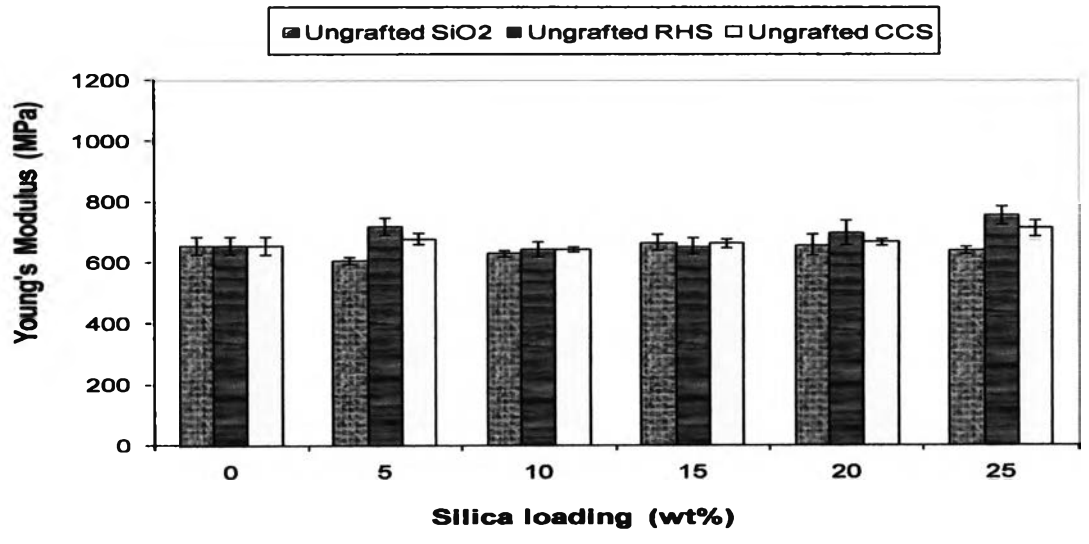

(a)

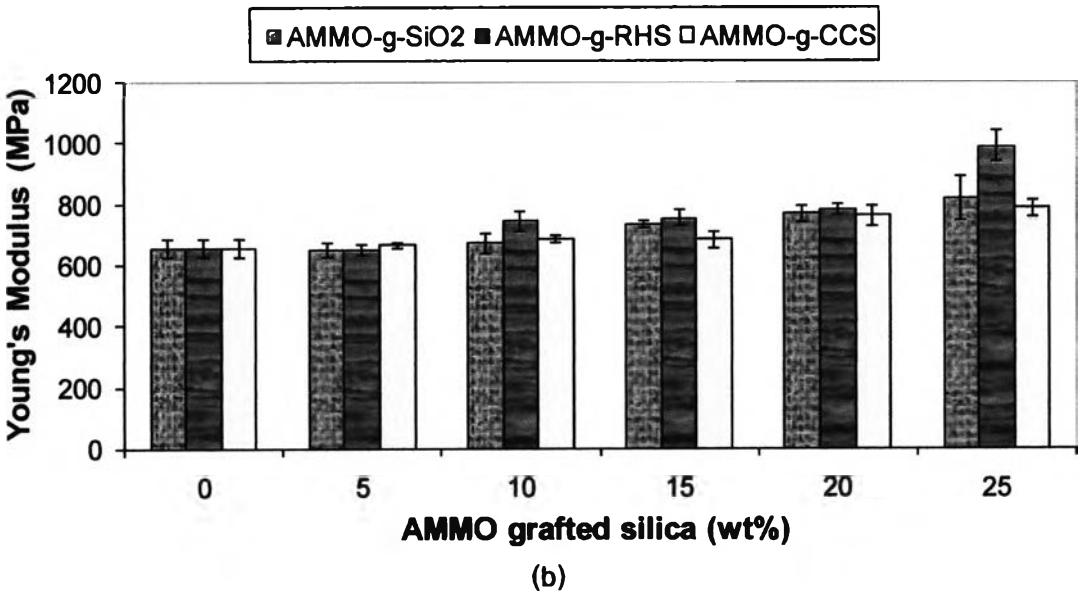

(b)

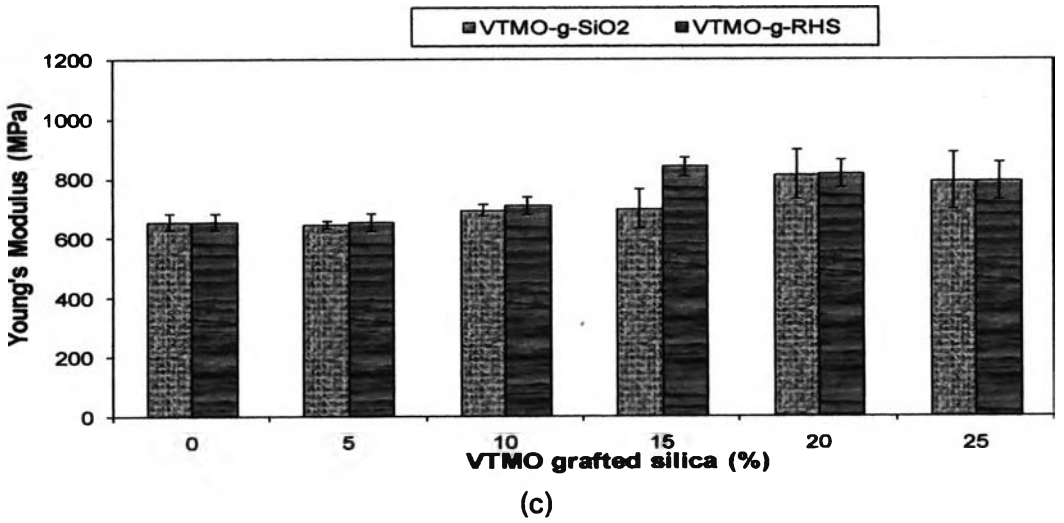

(c)

Figure 4.49 Effect of type and content of (a) ungrafted silica, (b) AMMO-g-silica, and (c) VTMO-g-silica on Young's modulus of ABS/5%OMT nanocomposites

Considering grafting efficiency, Figure 4.50 revealed that both types of modified silica showed better Young's modulus than ungrafted silica. This was because of strong polymer/filler interfacial action. In addition, it was also found that ABS/OMT containing VTMO grafted silica gave higher modulus than that of AMMO grafted. The higher efficiency of VTMO grafted silica was in agreement with the impact strength values discussed earlier in Figure 4.45, implying that the ABS/OMT nanocomposites having VTMO grafted silica was brittle than and not so strong as those having either ungrafted or AMMO grafted silica.

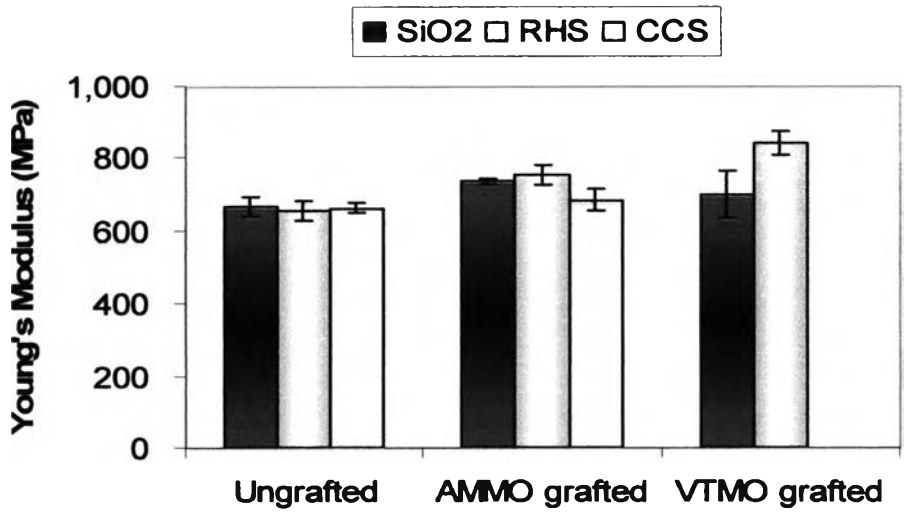

Figure 4.50 Effect of silane coupling type at 15 wt% on Young's modulus of ABS/5%OMT nanocomposites

4.4.6.2.2 Effect of Silatrane Type and Contents

Figure 4.51 revealed that the addition and increase of silatrane content led to an increase of tensile strength of ABS/OMT nanocomposites. However, the addition at high amount of modified silica and silatrane might cause the defect in ABS, lowering the tensile properties of ABS nanocomposites. This was due to agglomeration particles acted as an effective stress concentration points which had an impact on reducing the tensile properties of ABS nanocomposites. Nevertheless, silatrane could improve both of Young's modulus and fire retardant properties of ABS.

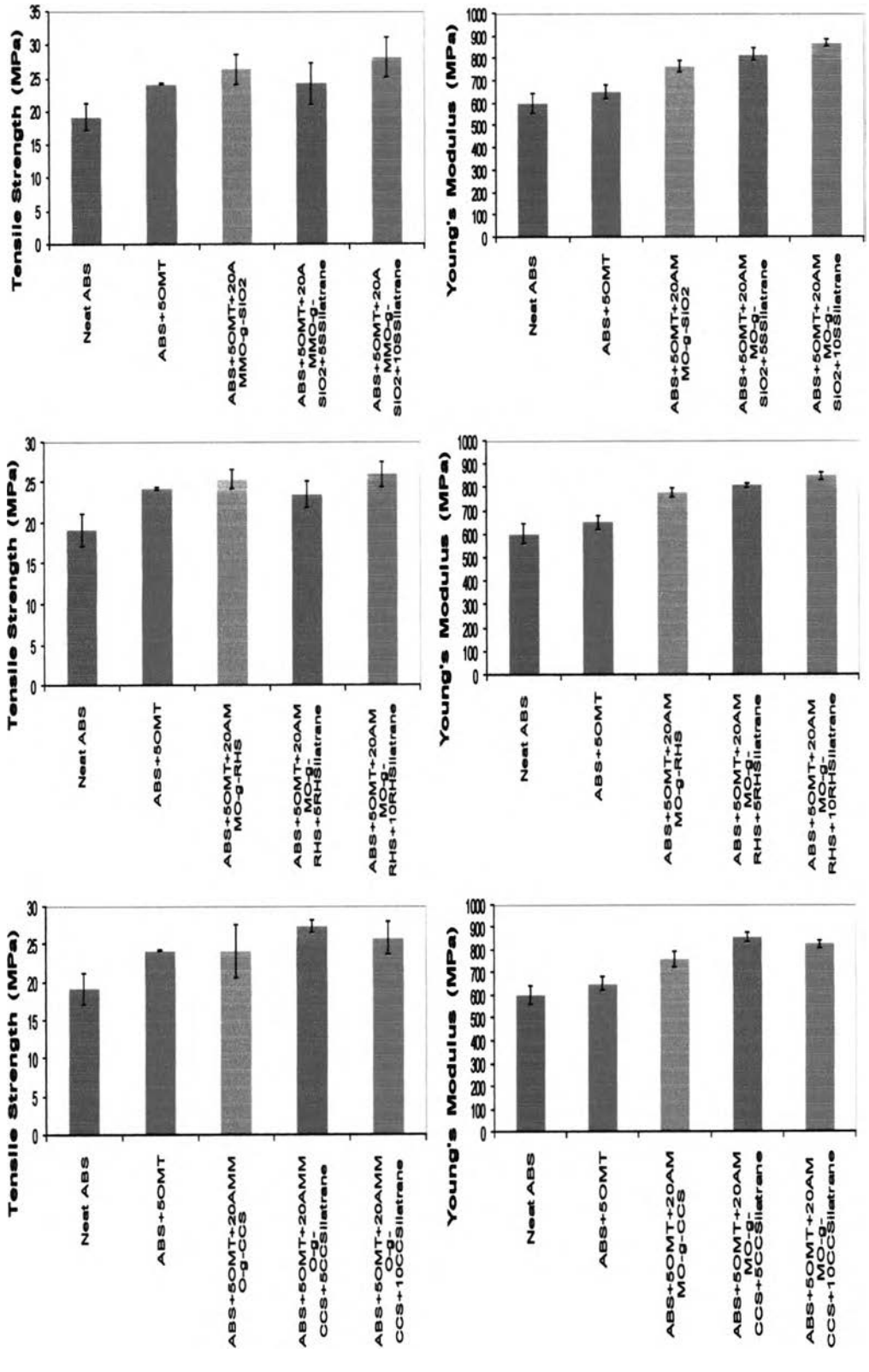

Figure 4.51 Effect of silatrane on tensile properties of ABS/OMT nanocomposites

From Figure 4.52 and Table 4.14, it can be concluded that ABS/OMT/AMMO-g-SiO_2/SSilatrane, ABS/OMT/AMMO-g-RHS/RHSilatrane, and ABS/OMT/AMMO-g-

CCS/CCSilatrane had higher tensile strength and Young's modulus than that of neat ABS and ABS/OMT nanocomposites. This might be from partial exfoliated structure of these ABS nanocomposites. It seemed that the silica type had no significant influence on the Young's modulus and tensile strength of the ABS nanocomposites. Both RHS and CCS exhibited similar efficiency and performance to commercial silica in terms of the tensile properties. The highest tensile strength and Young's modulus were attained at 35 wt% filler loading consisting of 5 wt% of OMT, 20 wt% of AMMO-g-silica, and 10 wt% silatrane.

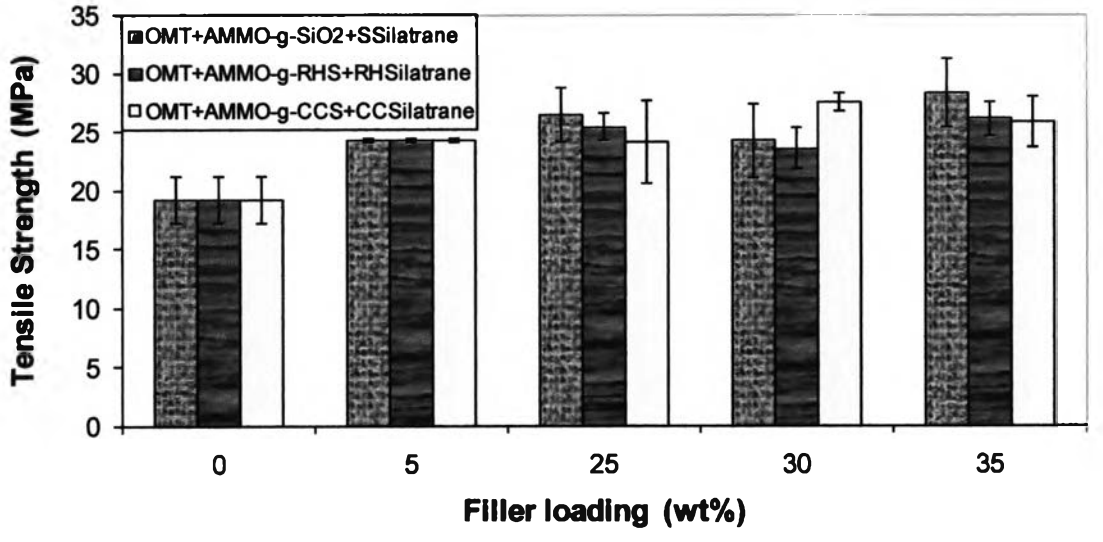

(a)

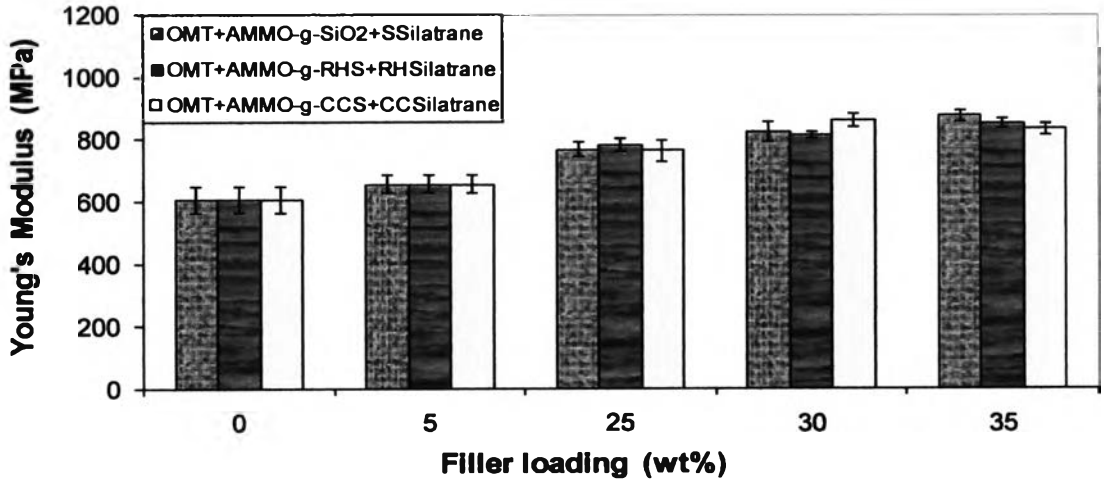

(b)

Figure 4.52 Effect of filler loading on (a) tensile strength and (b) Young's modulus of ABS nanocomposites

Table 4.14 Mechanical properties of ABS nanocomposites

Samples	Tensile strength (MPa)	Young's Modulus (MPa)	Impact strength (KJ/m^2)
Neat ABS	19.24 ± 7.03	605.97 ± 43.38	40.29 ± 2.38
ABS+5% AMMO	36.54 ± 0.26	632.71 ± 14.24	20.12 ± 0.94
ABS+5% VTMO	32.48 ± 5.38	602.96 ± 6.11	34.00 ± 4.29
ABS+5% OMT	24.25 ± 1.63	655.56 ± 28.93	4.22 ± 1.02
ABS+5% silatrane	17.45 ± 2.24	644.05 ± 24.35	10.23 ± 0.71
ABS+5%OMT ungrafted SiO_2	19.31 ± 0.26	604.27 ± 34.03	2.08 ± 0.15
ABS+5%OMT ungrafted RHS	21.01 ± 2.23	717.52 ± 27.89	2.70 ± 0.72
ABS+5%OMT ungrafted CCS	19.35 ± 0.49	676.09 ± 17.95	1.17 ± 0.68
ABS+5%OMT+20%AMMO-g-SiO_2	25.43 ± 2.26	767.57 ± 25.96	0.98 ± 0.38
ABS+5%OMT+20%AMMO-g-RHS	25.43 ± 1.19	782.57 ± 20.21	1.40 ± 0.29
ABS+5%OMT+20%AMMO-g-CCS	24.15 ± 3.48	763.26 ± 34.03	0.71± 0.75
ABS+5%OMT+20%AMMO-g-SiO_2 +10% SSilatrane	28.24 ± 2.92	874.29 ± 17.09	1.11 ± 0.34
ABS+5%OMT+20% AMMO-g-SiO_2 +10%RHSilatrane	26.06 ± 1.52	850.18 ± 14.67	1.63 ± 0.35
ABS+5%OMT+20% AMMO-g-SiO_2 +10%CCSilatrane	25.82 ± 2.15	831.52 ± 17.05	1.80 ± 0.21

ต้นฉบับ หน้าขาดหาย

ต้นฉบับ หน้าขาดหาย